

Study of Barium Titanate Epitaxy on Silicon toward Its Application in Video Holography

Tsang-Hsuan WANG

Supervisors:

Prof. dr. ir. J. Genoe

Prof. dr. ir. C. Merckling

Dissertation presented in partial
fulfillment of the requirements for the
degree of Doctor of Engineering
Technology (PhD)

February 2023

Study of Barium Titanate Epitaxy on Silicon toward Its Application in Video Holography

Tsang-Hsuan WANG

Examination committee:

Prof. dr. ir. K. Denis, chair

Prof. dr. ir. J. Genoe, supervisor

Prof. dr. ir. C. Merckling, supervisor

Prof. dr. ir. A. Stesmans

Prof. dr. ir. K. Temst

Prof. dr. ir. S. de Gendt

Prof. dr. C. Dubourdieu
(FU Berlin)

Prof. dr. D. van Thourhout
(Ghent University)

Dr. ir. P. Mlinowski
(Imec)

Dissertation presented in partial fulfillment of the requirements for the degree of Doctor of Engineering Technology (PhD)

February 2023

© 2023 KU Leuven – Faculty of Engineering Technology
Uitgegeven in eigen beheer, Tsang-Hsuan WANG, Wetenschapspark 27 box 15152, 3590 Diepenbeek (Belgium)

Alle rechten voorbehouden. Niets uit deze uitgave mag worden vermenigvuldigd en/of openbaar gemaakt worden door middel van druk, fotokopie, microfilm, elektronisch of op welke andere wijze ook zonder voorafgaande schriftelijke toestemming van de uitgever.

All rights reserved. No part of the publication may be reproduced in any form by print, photoprint, microfilm, electronic or any other means without written permission from the publisher.

Preface

This work is one part of Video Holography ERC Project (ERC grant agreement No. 742299), which will focus on investigating the materials for electro-optic waveguide for large Pockels effect to modulate the refractive index. The epitaxy of perovskite oxides on semiconductor substrates are studied in detail with their physical and optical properties being thoroughly examined, in order to obtain the material that can fulfill the requirements of the waveguide. This work is supported by imec, ERC grant (No. 742299) from Prof. J. Genoe, and ERC grant (No. 864483) from co-promoter Prof. C. Merckling.

Acknowledgement

First, I would like to thank Imec and the ERC funding for providing abundant resources on my research, so that I can carry out my PhD study in total freedom. At Imec, I have met a lot of researchers and engineers who are eager to share their experiences and knowledge with you, and there's always someone who can help you whatever difficulty you encountered. It is my pleasure to work with these nice and talented people.

There are many special people I would like to thank for. The first one is my promoter, Prof. Jan Genoe, who always helps me on every aspect of my research and provides me valuable opinions from different points of view. He also pays a lot of focus on all the details on my study, and through his patient guide, I am able to further refine and improve my research. Other than academic support, the casual talks from time to time always ease my nerves and make me feel less stressful. I am very appreciated from all his supports in my PhD study.

Another important person I would like to thank is Prof. Clement Merckling, who is my daily supervisor and the first person I go to if any issue happened. He helps me with everything, whether it's related to experimental or administrative. Whatever problems I have, he can immediately understand the situation, and give me his opinions on handling with such issues. Without his help, I cannot survive through all the tasks that I encountered in my PhD study. I'm also very grateful that Clement helps me a lot on my presentations. Even though there are still a lot to be improved, but I cannot have such progress if without his advice. With his great support, I am able to finish my PhD work in a relatively smooth and composed way.

A special thank should be given to all my committee members: Prof. Andre Stesmans, Prof. Kristiaan Temst, Prof. Stefan de Gendt, Prof. Catherine Dubourdieu, Prof. Dries van Thourhout, and Dr. Pawel Malinowski. Thank you for all the advice on my thesis, so that I can make this work more complete.

I would also like to thank Robert and Guillaume from the same ERC video

holography project. With the help from them, we have solved all kinds of difficulties and advance toward the realization of final device. Thanks to Robert, Ellipsometry is no longer a technique with intimidating and confusing fitting procedures, but a powerful tool which complements the physical characterizations in this thesis. As another PhD student in this project, Guillaume takes many integrations work, and also gives me many useful opinions in our discussions. Thanks to their help, my work can be smoothly integrated to the video holography application.

Next, a great amount of thanks should be given to the MBE-team: Kevin, Hans, Marina and whoever has helped on the maintenance of MBE tool. Only with the help from them, I am able to perform my growths and try out different experiments to complete my research at Imec.

I am also very appreciated with the prompt support from the MCA department at Imec, who helps me on the various characterizations. Thanks to Johan, who largely supports the stoichiometry analysis. Without his help, the growth process will be hundreds of times more difficult. Thanks to Maxim and Paola, from whom I can always obtain magnificent TEM results. The discussion with you always gives me inspirations and pushes me to investigate more. Together with the great help from AFM, PFM, XPS, and SIMS analyses, I am able to explore deeper on my materials.

I would also like to thank the EMCP members. Even though I'm not officially belong to this group, you still welcome me to many of your events. The discussion during the meeting as well as the daily casual talk all help me to keep on doing the research to finish my PhD study.

The Taiwanese friends in Belgium are definitely the people I would like to thank for. Thanks to the wonderful travel companions: Wen-Chieh, Yun-Tzu, Yun-An, and Brent, who not only support me experimentally, but also travel together and explore different attractions with me. Thanks to Jack, Kenny, Fan Yu, Thomas, Bing-Yang, Jhao-Rong, and Ji-Yung. The time we had lunch and coffee together definitely gives me energy to face all the difficulties in my studies and life. Thanks to Samantha and Shane, who always invite me to do more exercise. Without the help of these Taiwanese people, the life in Belgium will be so much more difficult.

Finally, I would like to thank my family and friends in Taiwan. My parents are always very supportive to whatever I want to do. Without their support, I cannot set my mind to study PhD after already started working for more than 3 years. Sorry that I'm always absent during the holidays in these years. I will be able to join again very soon. A million thanks to my sister, who gives me full mental supports. Whenever I talk to her, I feel relaxed and have the strength

to keep on facing all the difficulties. It's a bless to have you as my sister, my friend, and my always support. A special thanks to my boyfriend, who always listens to all my complaints, and provides me calmly with practical suggestions to face all the problems. I'm very appreciated for his tolerance on me being grumpy and cranky, and is always so patient with my sudden request.

Looking back on these years, I've learned a lot during my PhD study, and I'm very happy that I made the decision 4 years ago and decided to step outside my comfort zone. Even though there are some rough times that really makes me wonder if the decision is correct, I still persist and survive in the end. I would like to express again my sincere appreciation on all the helps I received during these years. I cannot finish this work without all of you.

Abstract

As the 2D display technology increases largely its resolution and refresh rate, the demand for 3D displays has also started to emerge. When compared to other 3D display technologies, holography has several advantages, including a wider viewing angle and a more complete image representation. This makes it a promising candidate to realize 3D displays. To move the 3D image, a recording material that can update the refractive index is necessary, and a material with large electro-optic (EO) effect is chosen as the target due to the fast response obtained by applying electric fields. Moreover, to realize the large EO effect, a material in single-crystalline phase with low defectivity is preferred. BaTiO₃ (BTO) is chosen as the material for video holography application due to its large EO coefficient and the possibility of being epitaxially integrated on large-scale Si substrates. The largest Pockels coefficients reported for thin BTO films are larger than 900 pm/V, which is much larger than for the already well-investigated LiNbO₃ (~30 pm/V) crystals. To control the epitaxial growth of BTO, molecular beam epitaxy (MBE) and pulsed-laser deposition (PLD) are used in this work.

To integrate epitaxial BTO films on Si(001) substrates, an SrTiO₃ (STO) buffer is needed for its thermodynamic stability in contact with Si and it does also reduce the lattice mismatch between the BTO and Si substrates. Since silicon is easily oxidized, the oxygen exposure amount and the temperature during the STO growth requires precise control to avoid immediate surface oxidation. As to the epitaxial BTO layers, the optical properties are strongly dependent on the BTO domain orientation. To obtain a large EO effect, both crystallinity and domain orientation should be well controlled.

In this thesis, the epitaxial perovskite oxides including STO and BTO are studied. MBE is used as the main growth technique, while PLD is used as an alternative for the epitaxial BTO study. Detailed investigations on the materials are executed, including the STO / Si interface control, the stoichiometry stability in thick oxide films, and the strain orientation manipulation in BTO layer.

Moreover, the optical properties are analyzed as a function of different physical properties, and they show to be highly correlated to the film crystallinity and the film orientation. The EO measurement is also performed on BTO films, and it shows that the EO effect of BTO depends strongly on the film quality than on the domain orientation. With the proper choice of the buffer layer, the strain orientation in the BTO layer can be controlled. Together with the detailed study on the crystal quality control, the BTO layer is demonstrated to be strained along the a-orientation with little relaxation.

Beknopte samenvatting

Terwijl de beschikbare 2D display technologieën al geruime tijd gekenmerkt wordt door een constante verhoging van de resolutie en updatesnelheid, stellen we vast dat er daarnaast ook langzaam een vraag naar 3D displays ontstaat. Er zijn meerdere technologieën beschikbaar die een 3D ervaring voor een kijker mogelijk maken, waaronder ook holografie. Holografie heeft zeer veel voordelen, waaronder een goede weergave onder een brede kijkhoek en een meer complete weergave van de beeldinhoud. Om een beeld van een hologram te laten bewegen is het noodzakelijk dat de brekingsindex van het materiaal van waaruit het hologram opgebouwd wordt, kan veranderd worden. Om dit te kunnen realiseren in mijn doctoraat, hebben wij een materiaal met een heel groot elektro-optisch (EO) effect gekozen om een actief veranderend hologram te implementeren. Hierdoor is een zeer snelle respons mogelijk bij het aanleggen van elektrische velden. Het is om een groot EO effect te kunnen bekomen echter wel belangrijk dat het materiaal mono-kristallijn is met een heel erg beperkt aantal defecten. Wij hebben voor BaTiO_3 (BTO) gekozen om video holografie toepassingen te kunnen realiseren, aangezien dit materiaal een erg grote EO coëfficiënt heeft en bovendien epitaxiaal kan worden geïntegreerd bovenop grote silicium wafers. Dunne filmen van BTO kunnen een Pockels coëfficiënt bereiken dat groter is dan 900 pm/V, wat beduidend meer is dan de reeds sterk bestudeerde LiNbO_3 (~ 30 pm/V) kristallen. Om de epitaxiale groei van BTO te controleren, hebben we moleculaire bundel epitaxie (MBE) en gepulste-laser depositie (PLD) gebruikt in dit doctoraat.

Om epitaxiale BTO filmen te kunnen integreren op silicium (001) substraten is een SrTiO_3 (STO) buffer laag noodzakelijk, aangezien deze thermodynamisch stabiel is op het silicium substraat en bovendien kan gebruikt worden om het verschil in rooster parameter tussen het siliciumkristal en het BTO op te vangen. Aangezien silicium gemakkelijk oxideert, is het belangrijk voor de STO groei om de zuurstofdruk en -temperatuur nauwkeurig onder controle te houden. In het andere geval oxideert het oppervlak ogenblikkelijk. Voor wat de BTO betreft, zijn de bekomen optische eigenschappen sterk afhankelijk van de oriëntatie van

de piezo-elektrische domeinen. Om dus een groot EO effect te bekomen moeten zowel de kristalliniteit als de domein oriëntatie goed onder controle gehouden worden. In dit doctoraat hebben we epitaxiale perovskieten, waaronder STO en BTO bestudeerd. MBE is gebruikt als de voornaamste groeitechniek, waarnaast PLD gebruikt werd als alternatieve depositietechniek om epitaxiale BTO te bestuderen. Een gedetailleerde studie van de materiaaleigenschappen werd uitgevoerd, met inbegrip van de controle van het interface tussen STO en silicium, de stoichiometrische stabiliteit van de dikke oxide filmen en het manipuleren van de oriëntatie van de interne spanningen in de BTO laag. Bovendien werden de optische eigenschappen geanalyseerd voor de verschillende deposities en er werd vastgesteld dat er een sterke correlatie is met de kristalliniteit en de oriëntatie van de dunne film. Ook het EO effect in de BTO laag werd gemeten en er werd vastgesteld dat dit effect sterker afhangt van de kwaliteit van de film dan van de oriëntatie van de domeinen. Met de juiste keuze van de bufferlagen kunnen we de oriëntatie van de interne spanningen in de BTO laag controleren. Vanuit de gedetailleerde studie van de kristal kwaliteit kunnen we afleiden dat de BTO voornamelijk onder spanning staat volgens de a-as, met slechts een beperkte relaxatie van deze interne spanningen.

List of Abbreviations

2D 2 Dimension(s)(al). vii, ix, 20, 21, 44, 71, 75, 83

3D 3 Dimension(s)(al). vii, ix, 1–3, 5, 20, 21, 71, 75, 83, 121, 122

AC Alternating Current. 30, 73

AFM Atomic Force Microscopy. 29–31, 42, 43, 47, 49, 50, 65, 71, 72, 78, 79, 83–85, 93, 94, 105, 107

ALD Atomic Layer Deposition. 14, 96

BEOL Back-end-of-line. 6

BF Bright Field. 33

BSO Barium Stannate, BaSnO₃. 99, 100

BTO Barium Titanate, BaTiO₃. vii–x, 10–18, 23, 25, 27–29, 32, 47, 54, 56, 61–75, 77–99, 101, 102, 107–113, 115–119, 121, 122

C-V Capacitance-Voltage. 34, 87–91, 94, 117

CGH Computer-Generated Hologram. 2–5

CMP Chemical-Mechanical Polishing. 119

CVD Chemical Vapor Deposition. 14, 96, 105

DC Direct Current. 73

DF Dark Field. 33

EO Electro-Optic. vii–x, 6–11, 15–18, 73, 115, 116

- FEOL** Front-end-of-line. 6
- FFT** Fast Fourier Transform. 45, 46, 48
- FOM** Figure-of-Merit. 10, 11
- FWHM** Full Width at Half Maximum. 14, 15, 27, 40, 42, 43, 51, 58, 60, 63, 64, 68, 70, 73, 75, 80, 81, 83, 96, 99, 101, 103, 106–109, 113, 116, 117
- GST** Germanium-Antimony-Tellurium compound, $\text{Ge}_x\text{Sb}_y\text{Te}_z$. 3, 4
- HAADF** High-Angle Annular Dark-Field. 33, 65, 66, 79, 80, 96, 111, 112
- HRTEM** High-Resolution Transmission Electron Microscopy. 33, 66
- I-V** Current-Voltage. 34, 87–89, 94, 101
- IR** Infrared. 72–74
- LNO** Lithium Niobate, LiNbO_3 . 9–11
- L NOI** Lithium Niobate-on-Insulator. 10
- MBE** Molecular Beam Epitaxy. vii, ix, x, 14–18, 21, 22, 24, 31, 37, 50, 51, 54, 56, 60, 61, 67, 71, 74, 77, 78, 83, 92–95, 99, 101, 107, 108, 116, 117
- ML** Mono Layer. 39, 41, 44, 46, 96, 102, 105, 106, 119
- NBD** Nano-Beam Diffraction. 33, 65, 67, 68, 74, 84–86, 94, 111–113, 117
- PCM** Phase Change Material. 2, 3, 6
- PFM** Piezoresponse Force Microscopy. 30, 31, 86–88, 117
- PIXE** Particle-Induced X-ray Emission. 31
- PLD** Pulsed-Laser Deposition. vii, ix, x, 14, 17, 18, 21, 25, 26, 77–79, 81–83, 85, 87, 92–98, 116
- PVD** Physical Vapor Deposition. 25
- QCM** Quartz Crystal Microbalance. 23, 56, 61
- QUAD** Cross Beam Source Quadrupole Mass Spectrometer. 23

- RBS** Rutherford Backscattering Spectrometry. 31, 32, 45, 47, 49, 52, 54, 55, 58–60, 63, 116
- RF** Radio Frequency. 23, 96
- RHEED** Reflection High-energy Electron Diffraction. 15, 22–25, 42, 44, 46, 51, 54, 55, 58–60, 62, 63, 65, 68, 69, 78, 103–107, 116, 118, 119
- RSM** Reciprocal Space Mapping. 27, 82, 83
- SE** Spectroscopic Ellipsometry. 16, 34–36, 50–52, 91, 92, 94
- SHO** Strontium Hafnate, SrHfO₃. 99, 100
- SOH** Silicon-Organic Hybrid. 9, 10
- STEM** Scanning Transmission Electron Microscopy. 33, 65, 66, 79, 80, 100, 111
- STO** Strontium Titante, SrTiO₃. vii, ix, x, 14–18, 29–32, 39–56, 58–61, 63, 65, 67, 68, 71, 72, 77–80, 83–86, 90, 93–95, 97, 99–109, 112, 113, 115–119
- SZO** Strontium Zirconate, SrZrO₃. 18, 101–109, 111–114, 117, 118
- TEM** Transmission Electron Microscopy. 15, 32, 33, 45, 46, 48, 51, 85, 96, 97
- UHV** Ultra-high Vacuum. 22, 56, 103, 107, 116
- VH** Video Holography. 5, 6, 9, 11, 16, 29, 51, 62, 65, 116
- XBS** Cross Beam Source Quadrupole Mass Spectrometer. 23, 56, 117
- XPS** X-ray Photoelectron Spectroscopy. 22, 33, 34, 45, 47, 49, 51, 52
- XRD** X-ray Diffraction. 15, 25–29, 42, 43, 46, 48, 58–60, 63, 68, 71, 73, 78–80, 82, 83, 85, 94, 96–98, 101, 103, 104, 106–110, 112, 113, 116, 117
- XRR** X-ray Reflectivity. 29, 50, 51, 93

List of Symbols

γ	surface energy
λ	wavelength
ϵ	permittivity
E	electric field
k	extinction coefficient
n	refractive index
R	Kerr coefficient
r	Pockels coefficient
L	Langmuir: gas exposure amount

Contents

Abstract	vii
Beknopte samenvatting	ix
List of Abbreviations	xiii
List of Symbols	xv
Contents	xvii
List of Figures	xxi
List of Tables	xxv
1 Introduction	1
1.1 Holography	1
1.1.1 From Static to Dynamic Holography	1
1.1.2 Updatable Holography in Video-framerate	5
1.2 Refractive Index Modulation	7
1.2.1 Non-linear Optics Pockels and Kerr Effect	7
1.2.2 Material Candidates with Large Pockels Coefficient	8
1.3 BaTiO ₃ Characteristics Review and Comparison	10
1.3.1 BaTiO ₃ Physical Properties	10
1.3.2 BaTiO ₃ Domain Orientation	13
1.3.3 BaTiO ₃ Epitaxy on Si Substrate	14
1.4 Problem Statement	16
1.5 Methodology Description	17
1.6 Thesis Outline	17
2 Epitaxy, Crystal Growth Techniques and Characterization Methods	19
2.1 Introduction to Epitaxy	19

2.2	Growth Technique	21
2.2.1	Molecular Beam Epitaxy	21
2.2.2	Pulsed-Laser Deposition	25
2.3	Physical Characterization	25
2.3.1	X-ray Diffraction	25
2.3.2	Atomic Force Microscopy	29
2.3.3	Piezoresponse Force Microscopy	30
2.3.4	Stoichiometry Characterization	31
2.3.5	Transmission Electron Microscopy	32
2.3.6	X-ray Photoelectron Spectroscopy	33
2.4	Electrical Characterization	34
2.5	Optical Characterization: Spectroscopic Ellipsometry	34
3	Fundamental Challenges of MBE-grown Lattice-matched Oxides on Silicon	37
3.1	SrTiO ₃ as Buffer Layer for Perovskite Oxides Integration	37
3.1.1	Sr-on-Si Surface Interaction	37
3.1.2	SrTiO ₃ on Si	39
3.2	Direct Epitaxial SrTiO ₃ Interface Control	42
3.2.1	Substrate Temperature Optimization	42
3.2.2	Oxygen Partial Pressure Optimization	43
3.3	Thick Oxide Growth and Source Oxidation Effect	54
3.3.1	Stoichiometry Evolution of Thick STO	54
3.3.2	Source Oxidation Effect	56
3.4	Conclusion	60
4	MBE-grown BTO on Si with STO Buffer Layer	61
4.1	Ba Temperature Compensation for Source Oxidation Effect	62
4.2	BaTiO ₃ Deposited Using Different Growth Rates	67
4.3	BaTiO ₃ Optical and EO Properties Comparison	71
4.4	Conclusion	74
5	PLD-grown BTO using STO / Si(001) Pseudo-substrate	77
5.1	BaTiO ₃ Epitaxial Growth on SrTiO ₃ / Si(001) Pseudo-substrate	78
5.2	BaTiO ₃ Orientation Control by Growth Parameter Variation .	81
5.3	Electrical and Optical Characterization of BaTiO ₃ with Different Orientation	86
5.4	Conclusion	93
6	Alternative Buffer Layer and Substrate for BTO Orientation Control	95
6.1	Alternative Substrate and Buffer Candidate: Literature Review	96
6.1.1	Alternative Substrate	96
6.1.2	Alternative Buffer	97

6.1.3	Literature Summary and Outlook	101
6.2	SrZrO ₃ Buffer Layer Epitaxy	102
6.2.1	SrZrO ₃ on Si Epitaxy	102
6.2.2	SrZrO ₃ on Ge / Si(001) Epitaxy	105
6.3	BaTiO ₃ Orientation Control Using Alternative SrZrO ₃ Buffer .	108
6.4	Conclusion	113
7	Conclusion and Outlook	115
7.1	Conclusion	115
7.2	Outlook	117
7.2.1	Effusion cell control with feedback loop	117
7.2.2	Alternative buffer optimization and extension	118
7.2.3	Single domain orientation with off-cut wafer	118
7.2.4	Wafer Bonding Processes for Video Holography Device .	119
A	Appendix: Exploitation Plan	121
	Bibliography	123
	List of Publications	151

List of Figures

1.1	Schematic of holography imaging	2
1.2	Schematic of dynamic hologram using CGH	3
1.3	Different phases comparisons of PCM	4
1.4	Schematic of dynamic holography using GST	4
1.5	Schematic of proposed video holography device	6
1.6	Pockels coefficient comparison for different materials	9
1.7	Schematics of SOH Mach-Zehnder modulator	10
1.8	Schematic of LNO integrated on Si substrate	11
1.9	BTO structure as a function of temperature	12
1.10	BTO film bonded on Si schematics	15
2.1	Schematic of vapor species at the sample surface during deposition	20
2.2	Schematic of different growth modes	20
2.3	Schematic of film nucleation	21
2.4	Side-view schematic of MBE Riber49 200 mm oxide chamber .	22
2.5	Schematic of RHEED pattern formation	24
2.6	RHEED pattern of different crystalline states	25
2.7	Schematic of PLD	26
2.8	Schematic of Bragg's condition	27
2.9	Schematic of the different angular manipulations of XRD measurement	28
2.10	Additional peaks in XRD asymmetric scans	29
2.11	Typical XRR curve	30
2.12	Schematic of AFM	31
2.13	Typical RBS profile	32
2.14	Schematic of XPS sampling depth	34
2.15	Illustration of Ellipsometry	35
2.16	Fitting procedure used for SE	36
3.1	Summary of Elemental Stability in contact with Si	38

3.2 Sr-on-Si Coverage and Surface Reconstruction	40
3.3 Schematic of step-by-step STO epitaxy on Si	41
3.4 STO RHEED with different substrate temperatures	42
3.5 AFM images of STO at different substrate temperatures	43
3.6 XRD and AFM comparison of STO at different temperatures	43
3.7 Experimental procedure of STO growth	44
3.8 Pressure profiles in the chamber as a function of time during STO epitaxy	45
3.9 RHEED of 1 nm and 4 nm STO	46
3.10 RBS of STO with different exposure amount	47
3.11 STO cross-sectional TEM images with different exposure amount	48
3.12 4-nm STO XRD results of STO(002) and (202) peaks	48
3.13 AFM of STO with different exposure amount	49
3.14 XPS of STO with different exposure amount	49
3.15 STO SE Raw spectra	50
3.16 STO n and k values comparison	52
3.17 STO bandgap extraction	53
3.18 Sr and Ti thermodynamic properties comparison	53
3.19 RHEED evolution of thick STO	55
3.20 RBS analysis of thick STO	55
3.21 Sr pressure under different gas ambient	57
3.22 Sr pressure change due to source oxidation	57
3.23 Sr pressure comparison under varied oxygen pressure	58
3.24 STO with high Sr temperature	59
3.25 STO with different growth rate comparison	59
4.1 BTO RHEED with different Ba temperature gradients	62
4.2 RBS analysis of BTO with different Ba gradients	63
4.3 XRD of BTO with different Ba gradients	64
4.4 XRD FWHM values comparison of BTO with different Ba gradients	64
4.5 AFM of BTO with different Ba gradients	65
4.6 HAADF of BTO with different Ba gradients	66
4.7 Dislocations around BTO islands	66
4.8 NBD mappings of BTO with different Ba gradients	67
4.9 NBD profiles of BTO with different Ba gradients	68
4.10 Ba stable pressure under oxygen environment	69
4.11 BTO with differernt growth rates comparison	69
4.12 XRD for BTO defect density extraction	70
4.13 AFM of BTO with different growth rates	72
4.14 Optical properties of BTO with different growth parameters .	73
4.15 BTO bandgap extraction	74
4.16 BTO Pockels coefficient with differetn Ba gradients	75

5.1 XRD and AFM of STO before and after annealing in the PLD chamber	79
5.2 XRD of BTO with different growth rates	80
5.3 HAADF images of BTO with different crystalline states	80
5.4 XRD of BTO with different substrate temperatures	81
5.5 XRD of BTO with different oxygen pressures	82
5.6 RSM of BTO with different oxygen pressures	83
5.7 AFM of BTO with different oxygen pressures	84
5.8 NBD mapping of BTO with different domain orientations	85
5.9 NBD profile of BTO in in-plane and out-of-plane directions	86
5.10 PFM amplitude map of BTO with different orientations	87
5.11 PFM butterfly curve of BTO with different orientations	88
5.12 Electrical measurement results of BTO	88
5.13 C-V of BTO with different oxygen pressures	89
5.14 Illustration of hysteresis BTO C-V curve	91
5.15 BTO refractive indices in different axes	92
5.16 Refractive indices comparison in function of film density	93
6.1 BTO on Ge(001)	97
6.2 BTO on MgO	98
6.3 Different perovskite oxides lattice parameter comparison	98
6.4 Epitaxial BSO on Si(001)	100
6.5 Epitaxial SHO on Si(001)	100
6.6 Epitaxial SZO on Ge(001)	101
6.7 Summary of BTO orientation as a function of buffers and substrates	102
6.8 Deposition procedure for SZO grown on Si(001)	103
6.9 RHEED of SZO / Si with different temperatures	104
6.10 XRD of SZO and STO grown on Si comparison	104
6.11 SZO and STO grown on Si AFM comparison	105
6.12 RHEED of SZO / Ge / Si as a function of temperature	106
6.13 XRD of different temperatures SZO / Ge / Si	107
6.14 AFM of different temperatures SZO / Ge / Si	107
6.15 XRD comparison between the same thickness STO and SZO . .	108
6.16 Optical properties of SZO	109
6.17 XRD of BTO on different buffers and substrates	110
6.18 c and a lattice parameter comparison of BTO on differernt buffers	110
6.19 STEM and NBD of BTO / SZO / Si	111
6.20 STEM and NBD of BTO / SZO / Ge / Si	112
6.21 Optical properties comparison of BTO with different buffers . .	113
7.1 RHEED comparison between on- and off-axis wafers	119
A.1 Targeted structure for video holography project	121

List of Tables

1.1	Comparison of EO effect coefficient for different materials	7
1.2	EO material comparison including the FOM value	11
1.3	BTO with different growth techniques comparison	14
4.1	Defect density summary of BTO with different growth parameters	71
A.1	Comparison of static and video holography applications	122

Chapter 1

Introduction

1.1 Holography

1.1.1 From Static to Dynamic Holography

Compared with photography invented in 19th century, holography is a relatively late-developed recording technique which was first proposed in 1948 by D. Gabor[1]. If the photography mainly responds to the intensity of light, holography also records the phase distribution, making it contains more “complete” information[2, 3]. Thus, for the holography image, the viewing angle is larger compared with photography, creating images that can be viewed in 3 Dimensions (3D).

The schematic of holography imaging is illustrated in Figure 1.1. To record the phase information, the beam reflected from the object interferes with a reference beam, and the interference pattern is recorded. Due to this additional interference with another beam, the phase distribution from the object is included into the produced interference pattern. To show again the object, the same reference beam would need to shine on the recorded pattern. After the beam is diffracted by the interference pattern, the image can be reconstructed, carrying the same information as the original object. Since the interference pattern contains all the information from the object, the recording media is named “hologram,” which came from the Greek word “holo” meaning “whole[4].” Today, holography is widely investigated and used in various fields such as security of the paper notes of different currencies.

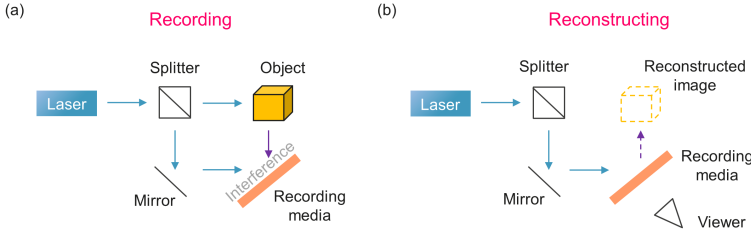


Figure 1.1: Schematic of (a) recording and (b) reconstructing of holography. The figures are adapted from Ref.[5].

At the beginning, the hologram was recorded on a photographic plate consisting of regions with different optical indices. This could be achieved by using materials such as polymers or photoresist, which showed large differences in optical response after suitable processing[6]. However, the indices of these materials cannot be changed once processed, thus could only create static holograms. To achieve dynamic holography, the optical indices of the recording media should be updatable to manipulate light path in real time. Other than updatable recording material, the interference pattern should also be changed in order to move the image. This concept was first proposed by Brown and Lohmann in 1966, who demonstrated the computer-generated hologram (CGH) based on physical optics theories[7, 8]. The schematic of using CGH to produce dynamic hologram is illustrated in Figure 1.2, which shows the calculated pattern is transmitted to a device that can modulate the light phase or intensity. These devices include means to change in between at least two states optically, such as liquid crystals or micromirrors that can change the mirror rotation angle to the incident light, resulting in affecting the light path and form 3D image after diffraction[9, 10]. Using the calculated diffraction pattern, the 3D image is created without the need of beam from real objects. The development of CGH opens up a new path towards 3D holograms, and is widely adapted in the realization of dynamic holography[11, 9].

To update the CGH pattern on holographic plate, a material with two reversable optical states is required, which makes the phase change materials (PCM) promising candidates. The crystalline state of PCMs can be controlled thermally between amorphous and crystalline states. The change of states affects directly the optical properties of the PCMs, as the refractive index n and extinction coefficient k show large differences[12, 13]. To change the states of PCM, the temperature needs to be higher than the melting point, which can be achieved

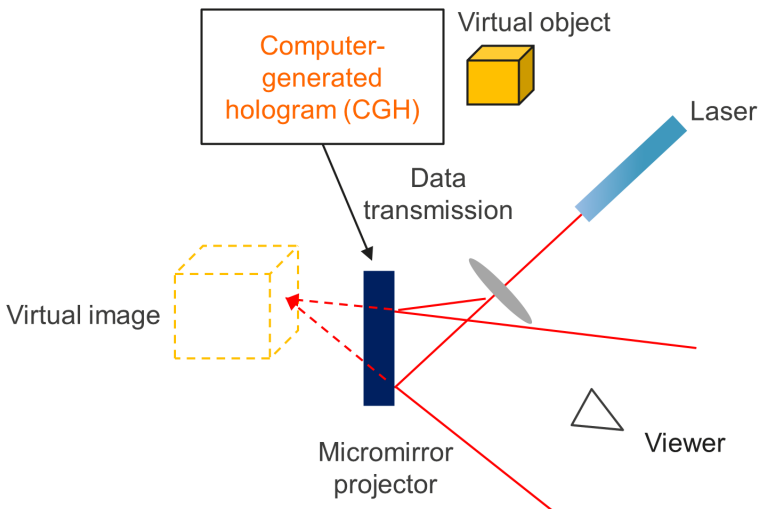


Figure 1.2: Schematic of dynamic holography produced by CGH pattern. The figure is adapted from Ref.[9].

with a high-energy laser beam. With varied thermal procedures, the material states are also different. As shown in Figure 1.3(a) and (b), with different laser power and duration, the material phase can be determined to be either the amorphous or crystalline state. The most widely investigated PCM is the germanium-antimony-tellurium compound ($\text{Ge}_x\text{Sb}_y\text{Te}_z$, GST), and its optical indices comparisons are shown in Fig. 1.3(c) and (d). At 1550 nm wavelength, the refractive index difference Δn can reach ~ 2 , showing great potential as the recording media for dynamic holography. Other than GST, VO_2 could also be a candidate since it also shows large refractive index differences of ~ 1 between its metallic and resistive states[12, 14].

The real dynamic holography with updatable image is demonstrated using GST with a laser beam to write and erase between different phases. The schematic of dynamic holography using GST is shown in Figure 1.4, which shows the CGH pattern creation by using a laser beam to define the crystalline state on the GST film. As the crystalline state in the GST film is changed, the refractive index is modified, finally producing a 3D image based on the calculated CGH. To move the image, a new CGH pattern would then be calculated and applied to the GST material. As a result, the continuous update on CGH results in the movement of 3D images.

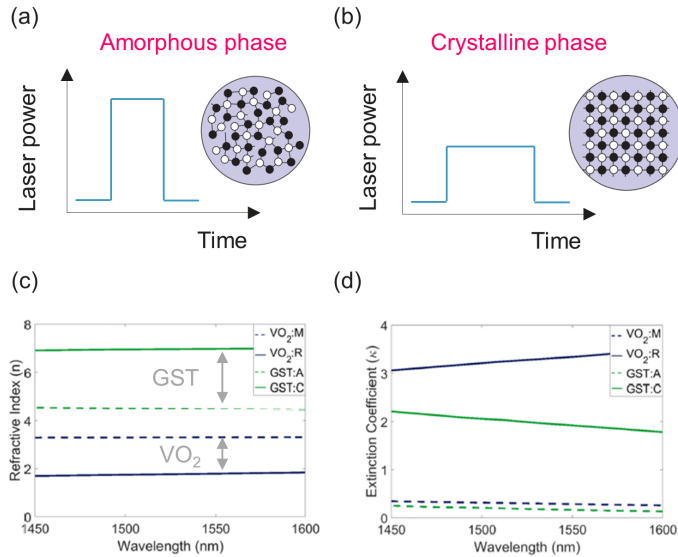


Figure 1.3: Different phase change material states of (a) amorphous and (b) crystalline phases. (c) Refractive index and (d) extinction coefficient comparison between different states, which show large differences between different phases. The figures are adapted from Refs.[12, 15].

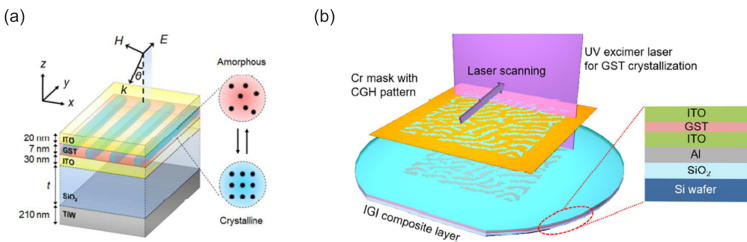


Figure 1.4: Schematic of dynamic holography using GST to change the refractive index. (a) GST film consisting of both amorphous and crystalline states to manipulate light path. (b) CGH pattern created by laser scanning. The images are adapted from Refs.[16, 17].

However, due to the fact that process of phase change involves thermally heating up and cooling down, the time to change the refractive index is relatively long. Even though the phase change speed has much improved these days with reported values reaching tens of ns, it is still quite long compared to electric-driven reactions[18, 19]. Moreover, it is difficult to confine the thermal reaction in a small region without affecting neighboring pixels, thus the resolution of the hologram is limited. In addition, the calculation of the CGH pattern is time-consuming, further lowering the updating frequency of the 3D image. Therefore, a new material which doesn't require thermal processing to change its refractive index, as well as a new device structure without using CGH is necessary to reach the holographic display in video-framerate.

1.1.2 Updatable Holography in Video-framerate

Based on the need for faster and higher resolution 3D display, a new structure with novel materials for video holography (VH) application was proposed by Prof. Genoe's ERC project (ERC grant agreement No. 742299), and the device structure is shown in Figure 1.5. On top of the CMOS transistor, a new type of interconnects consisting of transparent conductive metamaterials is needed to apply an electric field to the top waveguide. Meanwhile, the waveguide will be made from electro-refractive material, with the refractive index being changed by the applied electric field. The laser light is introduced laterally and propagates in the waveguide with little dissipation. Only for the regions with electric field, the light would be leaking out since the refractive index is changed and cannot satisfy the criteria for total internal reflection. In this way, we should be able to control the leaked out light pattern, resulting in a 3D image on top of the device.

To achieve video-framerate holography with the proposed device structure, there are several problems that need to be solved. First, a new transparent metamaterial layer consisting of conductive oxides between insulators to apply locally an electric field in the waveguide, and controlled by the bottom CMOS devices is needed. The traditional metallic interconnects will absorb light, thus cannot be used in such proposed photonic devices. Also, in between the conductive and insulating materials in the metamaterial matrix, the refractive indices should be close to avoid light scattering at the pillars. On the other hand, the pitch between conductive pillars should also be small enough to obtain a high-resolution image. To control the light, the spacing should be smaller than $\frac{1}{4}$ of the wavelength, which requires the spacing to be smaller than 100 nm for blue light. Thus, the CMOS transistor dimensions also need to be scaled down. The advanced 10 nm FinFET CMOS technology would perfectly fulfill the requirement.

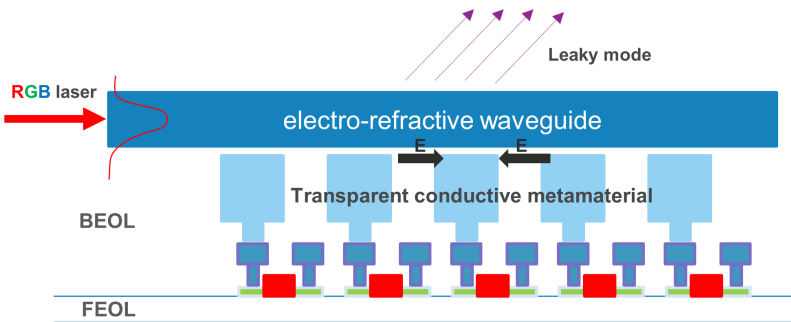


Figure 1.5: Schematic of proposed video holography device. The front-end-of-line (FEOL) consists of 10-nm node transistor, and the transparent conductive metamaterial is used in back-end-of-line (BEOL), replacing the traditional metal interconnects.

The electro-refractive waveguide should be composed of materials with large differences in refractive index as a function of the applied electric field. It should also have a small extinction coefficient k so that light could travel without heavy absorption (optical losses). The Electro-optic (EO) material is chosen as our target because of its fast response time compared to PCM. The response time of the EO material is expected to be smaller than 1 ns, which largely reduces the writing time[20]. For a 1 cm^2 hologram containing 20000 lines/mm, the total estimated writing time would be only ~ 0.8 ms using CMOS to control. For the full-color image, 3 lasers of red, green, and blue will be used, resulting in 3 times the processing time. However, even with the 2.4 ms writing time, it is still very sufficient for the update frequency to exceed 60 Hz. Moreover, without the thermal process, the regions of refractive index change can be well-defined by the pillar size and spacing, making EO materials more attractive than PCM in this VH application.

For this new VH device, the study will be divided into two parts: the study on (1) metamaterials and (2) on electro-refractive waveguides. In this thesis, we will focus on the waveguide material, with the target to find a material that shows a large refractive index difference (Δn) while preserving a small extinction coefficient and that can be easily manipulated by an external electric field.

Table 1.1: Comparison of Electro-optic (EO) effect coefficients for different materials

Material	n_o	Pockels coefficient r (pm/V)	Kerr coefficient R (cm 2 /W)
Si	3.4	—	2.7×10^{-14}
Ge	4	—	9.9×10^{-14}
GaAs	3.4	1.2	3.3×10^{-13}
LiNbO ₃	2.3	31	5.3×10^{-15}
KDP	1.5	10.5	2.8×10^{-16}

1.2 Refractive Index Modulation

1.2.1 Non-linear Optics Pockels and Kerr Effect

The refractive index of a certain material is usually stable and will not be easily affected by external forces. However, as the force magnitude increases, the optical properties will eventually be modified. The refractive index changed by an applied electric field is called the electro-optic (EO) effect. The EO effect can be roughly divided into two categories based on its response to an electric field: linear Pockels effect and quadratic Kerr effect. The change of refractive index Δn by the applied electric field E can be expressed by the equation[21]:

$$\Delta n = -\frac{1}{2}n^3(rE + RE^2) \quad (1.1)$$

where r represents the Pockels coefficient and R the Kerr coefficient. The comparison between these two coefficients of some common materials is listed in the Table 1.1. The values are adapted from various reports in the literatures dealing with different light wavelengths, and are only shown for simple comparison[22, 23, 24, 25, 26]. For the centrosymmetric materials such as Si, only the Kerr effect could be observed; while for the non-centrosymmetric materials, the Pockels effect is often more pronounced, and its Kerr effect can be neglected.

In silicon photonics, light is used as the information carrier based on its larger bandwidth compared with electrons at extreme small interconnect dimensions[27]. Silicon photonics requires components which can manipulate the light path, thus the ability to change the refractive index is mandatory. However, due to the its centrosymmetric lattice structure, the change of refractive index for Si is small. Even though a change in carrier concentration can affect the refractive index in Si, the loss would increase, making the device less effective

and harder to design[28]. In order to change the refractive index more efficiently, a non-centrosymmetric material possessing a large Pockels coefficient is preferred. Moreover, with a large Pockels coefficient, the smaller applied electric field can save energy and protect the material from hard breakdown, which adds more advantages for the real applications. Thus, new materials with large Pockels effect can be very beneficial for silicon photonics as well as applications in holography.

1.2.2 Material Candidates with Large Pockels Coefficient

The Pockels coefficient can be linked to several material properties with the equation of[21]:

$$r_{ijk} = \varepsilon_0 f_{ijm} (\varepsilon_{mk}^0 - \delta_{mk}) \quad (1.2)$$

where r_{ijk} is the Pockels coefficient, f_{ijm} is the polarization-optic tensor, ε_{mk}^0 the real part of the permittivity tensor and δ_{mk} the imaginary part of the permittivity tensor (losses). The notations i, j, k, m correspond to the direction of applied electric fields. Based on this equation, it has been reported that a large Pockels effect is often observed in materials with large dielectric permittivity and spontaneous polarization[29]. In Figure 1.6, materials ranging from traditional semiconductors to organic and ferroelectric oxides are summarized with the reported Pockels coefficient[30, 31, 32, 33, 34, 35]. For traditional semiconductor materials, the Pockels coefficient is very small (~ 1 pm/V), which makes realization of the refractive index change more difficult in these materials. For materials with larger Pockels coefficient, two categories show much larger potential: organic and ferroelectric oxides.

Organic Materials

To produce a more pronounced Pockels effect, the organic material should be ordered into a non-centrosymmetric way, which can be achieved by incorporating the material into a polymer matrix or to recrystallize the material to form organic crystals[32, 36]. By carefully designing the donor and acceptor groups of the chromophores, the EO coefficient is reported to reach larger than 1000 pm/V at the 1310 nm wavelength[37]. Compared with inorganic materials, the organic materials show almost a constant EO coefficient over a wide frequency range, which is important for broadband applications[21]. In addition, the driving voltage can be very small for organic materials, resulting in devices with high energy efficiency[38]. Various devices using organic EO materials are

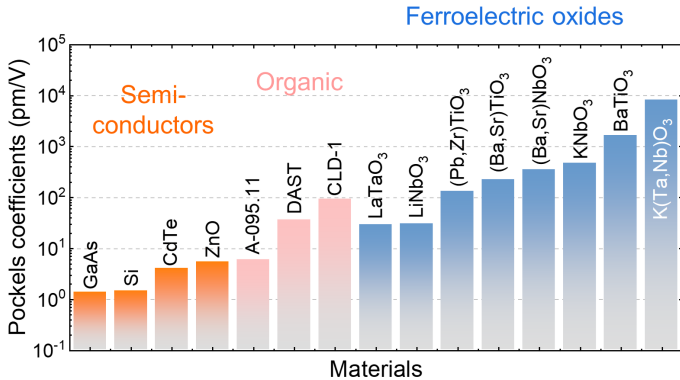


Figure 1.6: Pockels coefficient comparison for different materials. The values are adapted from Refs.[30, 31, 32, 33, 34, 35].

demonstrated with the silicon-organic hybrid (SOH) integration, which utilizes the large EO response from organic materials while the light is guided in a low-loss silicon waveguide[39, 40]. The schematic of SOH device is presented in Figure 1.7, with light being confined in the Si slot and the electric field applied on the EO material around to affect the optical behavior. With the SOH device, the modulation at 12.5 Gbit/s with the an applied voltage of only 80 mV has been demonstrated[38]. However, although the organic material device is easy to fabricate, it is less stable material and could easily be influenced by its surrounding environment. The stability issues including thermal stability of poled organic materials and the photochemical stability all require further studies to achieve improvement[41]. It has been demonstrated that the device dimensions and design would strongly affect the EO performances using organic materials[42]. Moreover, since the organic materials often show strong absorption in the visible wavelength, their application on VH is not feasible[43].

Ferroelectric Oxides

Another group of materials that possesses large potential is the group of ferroelectric oxides. These materials show on average a large permittivity and some materials also possess spontaneous polarization, thus is expected to exhibit a larger Pockels response in general. Among them, the LiNbO₃ (LNO) is widely studied and has been successfully demonstrated to be integrated on a

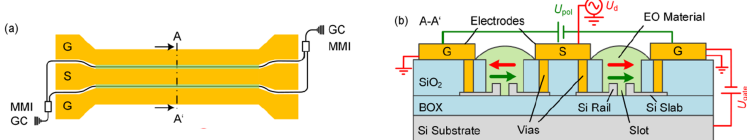


Figure 1.7: Schematics of SOH Mach-Zehnder modulator. (a) plan-view and (b) cross-sectional schematics. The figures are adapted from Ref.[39].

silicon photonics platform. As illustrated in Figure 1.8, the LNO thin film on SiO₂ / Si can be obtained by bonding a bulk LNO substrate (2" to 4") to a target Si wafer, forming the Lithium Niobate-On-Insulator (L NOI) platform for different photonic devices[44]. With a split off film from the bulk substrate bonded to the planarized silicon waveguide, various photonics components such as waveguide and Mach-Zehnder modulator are fabricated[44, 45]. The refractive index differences between LNO and SiO₂ is large, enabling a better confinement of light in the waveguide, which results in an increase of the packing density using the L NOI platform. Together with the larger EO response compared to Si, the L NOI shows a smaller operational power and higher reliability, creating possibilities of building all photonic components on a L NOI platform[46, 47]. The large EO response results in ultra-wide bandwidth, which is reported to exceed the 100 GHz 3-dB bandwidth for the unetched LNO film on Si single-mode photonic circuits[45]. Despite many building blocks have already been demonstrated using LNO, many questions still need to be resolved, and the diameter upscaling of the LNO substrate is one of the major drawbacks which requires further improvement. Until now, there is still no 8-inch LNO wafer available commercially, which increases the difficulty of scaling up and limits the realization of L NOI for integrated photonic circuits.

1.3 BaTiO₃ Characteristics Review and Comparison

1.3.1 BaTiO₃ Physical Properties

To fully realize a large Pockels effect using ferroelectric oxides, BaTiO₃ (BTO) becomes an even more promising candidate than LNO. The change of refractive index based on Pockels effect is proportional to n^3r as is clear from Equation 1.1, and the comparison between materials including this figure-of-merit (FOM) n^3r value is shown in the Table 1.2. For inorganic materials, the refractive

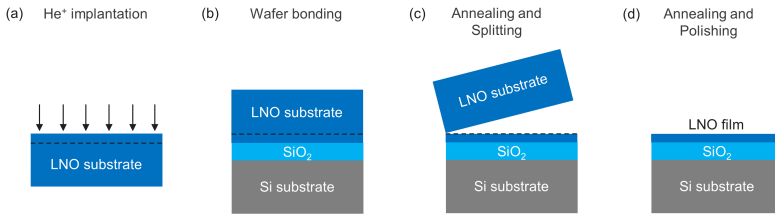


Figure 1.8: Schematic of LNO integrated on Si substrate. The figures are adapted from Ref.[44].

Table 1.2: EO material comparison including the FOM value

Material	r (pm/V)	n	n^3r (pm/V)	λ (nm)	Reference
Inorganic:					
LiNbO ₃	31.5	2.2	340	633	[21]
GaAs	1.2	3.5	51	1020	[21]
KNbO ₃	63.3	2.2	650	633	[21]
BaTiO ₃	1640	2.5	25625	514	[22]
Organic:					
DAST	92	2.5	1470	720	[21]
CLD-1	130	1.65	584	1313	[21]
BAY1	1100	2.02	9100	1310	[37]

index n is usually large, while the organic materials can possess a larger Pockels coefficient r in case of careful material design. Both of these values should be high in order to obtain a larger FOM value. As shown in the Table 1.2, the BTO shows not only a large theoretical r but also a high n , resulting in a much larger FOM value compared with other materials. This large FOM value makes this material extremely promising for EO applications and it has obtained much focus in the past decades. Moreover, the BTO thin film has been reported to epitaxially grow on a Si(001) substrate if carefully controlled, which largely increases the possibility of industrialization for this material compared with LNO[48]. Thus, for the VH application, fBTO will be our target material, and the material properties of BTO epitaxial films on Si(001) will be studied in detail.

As shown in Figure 1.9(a), BTO is in a tetragonal phase at room temperature, with a lattice parameter of 4.03 Å in one axis and 3.99 Å in the other two axes. The slight displacement of the Ti atom from the center of the perovskite

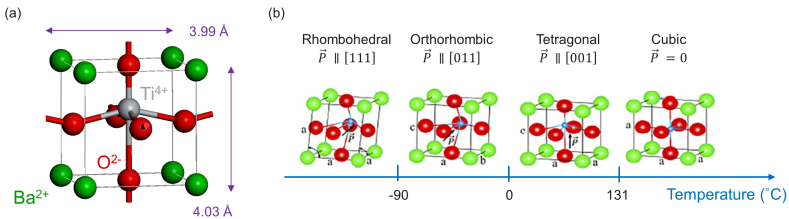


Figure 1.9: (a) BTO lattice structure at room temperature. (b) BTO phase change as a function of temperature. The figure (b) is modified from Ref.[51].

lattice results in the spontaneous polarization, which is also the source of ferroelectricity in BaTiO₃[49, 50]. The detailed BTO phase evolution as a function of temperature is presented in Figure 1.9(b), which shows that at higher temperature ($T \geq 131$ °C), the BTO is in the cubic phase and no ferroelectricity is expected since the structure is centrosymmetric. When the temperature is lower than the Curie temperature $T_c \sim 134$ °C, ferroelectricity starts to appear as the structure changes to a non-centrosymmetric tetragonal phase[50, 51]. As the structure deviates from cubic, the Ti atom will slightly shift from the center position, forming a dipole with the orientation parallel to the elongated axis. The Ti position can be on different side from the center, creating dipoles in the opposite direction. Within a ferroelectric domain, all the dipoles are aligned in the same direction, and the domain walls can be further moved by external forces to affect the final ferroelectric characteristics[52]. When the temperature is further cooled down, the BTO structure even distorts to orthorhombic and rhombohedral, and the polarization orientation also slightly changes.

Several mechanisms are responsible for the high Pockels coefficient observed in BTO, including a large permittivity, piezo-response from the applied field, and the spontaneous polarization change under external force. For BTO, the dielectric permittivity is reported to exceed 1000 at 20 GHz frequency, which is much larger compared with Si (~11)[53]. When applying an electric field to BTO, the field from spontaneous polarization is changed, which modifies the light passing through the material and results in the change of refractive index. Moreover, the piezo-electric property further moves the ions when applying the electric field, creating even more shift to the incident light[54, 55]. The modulation in optical properties by lattice vibrations is linked to Raman susceptibility, which estimates the coupling between electrons and phonons[56]. With the electronic states affected by phonons, the larger Raman susceptibility

is reported to result in larger Pockels responses[57]. Based on the density functional theory (DFT) simulation by Hamze et al., the BTO possessed a non-centrosymmetric structure with soft phonons (correlated to lowering of the symmetry and the spontaneous polarization formation) and strong electron-phonon interaction, which resulted in the large Pockels effect[58].

1.3.2 BaTiO₃ Domain Orientation

When no external force is applied on BTO, the numbers of domains containing dipoles with opposite directions are equal. For BTO at room temperature, the domain orientation is determined by its elongated axis direction. Different BTO domain orientations can largely affect overall the Pockels effect due to the coefficient is orientation-dependent and can be written in tensor form. The Pockels effect is affected by both the electric field and domain orientations of the material, as illustrated by the equation[22]:

$$\Delta \left(\frac{1}{n^2} \right)_i = \sum_j r_{ij} E_j \quad (1.3)$$

where r is the Pockels coefficient and E is the electric field. Based on the BTO tetragonal structure, the detailed Pockels coefficient tensor can be written in the form:

$$r_{ij} = \begin{bmatrix} 0 & 0 & r_{13} \\ 0 & 0 & r_{13} \\ 0 & 0 & r_{33} \\ 0 & r_{42} & 0 \\ r_{42} & 0 & 0 \\ 0 & 0 & 0 \end{bmatrix} \quad (1.4)$$

As shown in Equation 1.4, due to the symmetry of the tetragonal phase, only a few entries in the tensor are non-zero. In bulk BTO, the largest value is $r_{42} = 1640$ (pm/V), which is at least one magnitude larger than the other parameters[22]. Combining Equation 1.3 and 1.4, in order to take advantage of the largest Pockels effect, the electric field will need to be applied from a certain direction with respect to the BTO domain orientation[59]. Based on the elongated axis direction, the BTO domain can be categorized as c-oriented BTO (c-BTO) or a-oriented BTO (a-BTO), with the elongated axis in the out-of-plane direction for c-BTO and in the in-plane direction for a-BTO. How to control the BTO orientation will be one of the main topics in this thesis.

Table 1.3: Pockels coefficient comparison of BTO thin films grown by different growth techniques on a Si substrate

Growth technique	Sputtering	ALD	CVD	PLD	MBE
Pockels coefficient (pm/V)	41±15	26±6	7±4	37±27	624
Thickness (nm)	96	40	70	97	50
BTO(002) FWHM (°)	Epi+Poly	~0.8			
Reference	[60]	[61]	[60]	[60]	[62]

Based on the theoretical Pockels coefficient value of 1640 pm/V, the change of refractive index Δn can reach the value of larger than 0.4 with an applied electric field of 1 V/100 nm at the 500 nm wavelength.

1.3.3 BaTiO₃ Epitaxy on Si Substrate

The integration of BTO on a large scale substrate such as Si or Ge has been widely investigated, and properties of epitaxially grown BTO films using different techniques are compared in the Table 1.3. To compare fairly between different techniques, all the Pockels coefficients are taken from BTO films with thickness smaller than 100 nm; this shows that the largest value is reported from BTO grown by molecular beam epitaxy (MBE). This difference is mainly attributed to the better film crystallinity obtained by MBE, which preserves the poled dipoles in the same direction without being interrupted by defects[60]. In Table 1.3, all the listed Pockels coefficients are from BTO films epitaxially grown on a Si substrate, with a thin SrTiO₃ (strontium titanate, STO) buffer layer grown by MBE prior to the BTO epitaxy. The STO buffer growth and characterization will be discussed in detail in the chapter 3.

Various research groups reported detailed studies on the BTO epitaxial films grown on a Si(001) substrate, including domain orientation characterization and film quality analysis[63, 64, 65]. It was reported by Mazet et al., that the MBE growth parameters including the oxygen pressure and substrate temperature largely affected both the BTO film quality and the domain orientation. With the higher the oxygen pressure, the more a-oriented the films became[63]. Another important factor that changed the BTO domain orientation was film thickness, which was thoroughly examined by Dubourdieu et al., who showed the c-BTO was preferred with smaller thickness, while the a-BTO was more often observed in thicker films (> 40 nm)[66]. The further modification of BTO films was investigated by Kormondy et al., who demonstrated that with increased post-annealing temperatures in O₂ ambient, not only the BTO film quality was improved, but the domain orientation was changed from c- to a-oriented[64].

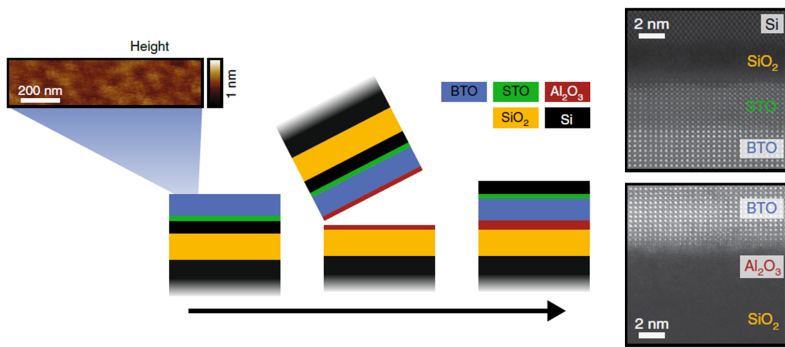


Figure 1.10: Schematic of BTO films bonded on Si for photonic devices fabrication. The BTO epitaxial film with flat surface is bonded to another substrate of SiO_2 / $\text{Si}(001)$. In this way, the light can be confined in BTO layer once the total reflection criteria are satisfied. The figures are adapted from Ref.[67].

Moreover, the a-BTO showed to have larger Pockels effect, which was consistent with the calculation from the previous work[59]. Finally, the photonics devices using BTO films are integrated together with a traditional Si photonics platform. The largest measured Pockels coefficient of $r_{42} = 923 \text{ pm/V}$ was reported by Abel et al., with the 225-nm BTO film bonded on the Si wafer to fabricate the waveguide[67]. With the high quality BTO epitaxial film (XRD FWHM $\sim 0.3^\circ$) and the electrodes rotated 45° on the BTO surface to pole all the a-oriented domains, the fabricated device was measured with frequency up to 65 GHz, showing very competitive performances while preserving the unique large EO response compared with Si. The schematic of epitaxial BTO bonded on Si for EO devices is illustrated in Figure 1.10.

The study on MBE-grown BTO has also been investigated in the previous works from our group. The impact of Ba/Ti ratio variations on BTO films was studied, with the detailed change on diffraction behavior, including RHEED, XRD, and TEM being simulated and discussed[68]. Also, the impact on domain orientation by varying both the thickness of STO buffer and BTO active layers were investigated thoroughly, which showed the differences in thermal expansion coefficient with respect to Si and STO resulted in the opposite effect on BTO domain orientations[69]. The strain relaxation in BTO / STO structure was also examined, and by using STO-BTO superlattice structure, the defect formation was limited, and the overall film quality was improved[70]. Finally, the 100-nm BTO films with an XRD FWHM value $\sim 0.7^\circ$ in both c- and a-orientation were

measured by spectroscopic ellipsometry (SE) with an applied electric field[71]. Even though the change in refractive index (Δn) showed differences between the c- and a-BTO, the deviation was not obvious by SE analysis, thus a new characterization technique for the Pockels coefficient extraction from our BTO films is still needed.

1.4 Problem Statement

Even though BTO films have already been demonstrated with good crystallinity and large EO response, there are still many unclear issues. First, despite the good BTO epitaxial quality reported by MBE, the process stability remains challenging. To obtain consistent BTO films with the same crystallinity, various parameters including pressure, temperature, and stoichiometry need to be precisely controlled. With the stoichiometry slightly deviating from ideal, the film quality would largely degrade. Thus, a systematic way to control the film quality is needed and more detailed studies should be executed.

Second, due to high vacuum in the MBE chamber, oxygen vacancies prevail in the BTO films. These defects have an impact on the optical properties, especially in the longer wavelength region[72]. Also, the electrical properties will be affected since the oxygen vacancies can increase the leakage current. This causes unwanted problems and requires additional annealing in order to compensate the oxygen deficiency in the BTO thin films.

For the EO effect, most published works focus on the correlation between domain orientations and the measured Pockels coefficient. However, the impact from different defects is scarcely discussed. Typical BTO films are grown on a STO buffer layer on top of a Si substrate, which creates compressive strain and results in c-BTO formation. The a-BTO could be obtained with the internal strain being relaxed by increasing thickness[66]. However, to relax the accumulated strain, defects including dislocations or domain boundaries will be created. Thus, domain orientation and the film quality seem to be a trade-off. In this work, the BTO films with the target thickness of 100 nm in a-orientation will be our final goal for the VH application. How to create an a-oriented BTO on a Si substrate without increasing the defect density as well as maintaining the strain will be our main research subject in this thesis.

1.5 Methodology Description

To epitaxially integrate oxides on the Si substrate, MBE is generally the favorite technique. In this thesis, the BTO active layers and STO buffer layers have been grown by MBE. The film properties will be analyzed with various characterizations, including physical analyses for the film structure and strain, as well as optical measurement for the refractive index and extinction coefficient. To maintain the film quality stability, detailed studies on temperature and oxygen pressure control will be executed. Moreover, the pressure evolution of different metallic species under varied oxygen ambient will be investigated in order to acquire better control of film stoichiometry.

Another technique to epitaxially grow BTO film is the pulsed-laser deposition (PLD). Since the working pressure of PLD is much higher than MBE, the oxygen vacancies are expected to be reduced. In addition, during the deposition, all the materials from the ceramic target will be ablated by the high-energy laser beam. Hence, the stoichiometry of PLD-grown BTO film can be more easily controlled compared to MBE. Moreover, with the alternative growth technique, the change of BTO domain orientations will be studied as a function of different PLD growth parameters.

Finally, a different buffer and substrate will be researched in order to control the BTO orientation without the necessity of strain relaxation via increase in defectivity. This should open up new opportunities of obtaining higher EO response for BTO film with high quality in the desired orientation.

1.6 Thesis Outline

In this thesis, the detailed epitaxial quality control is investigated from the STO buffer to the BTO active layer. Also, the EO response with different domain orientations and crystallinity is studied. As an alternative way of obtaining epitaxial BTO, the PLD growth will also be evaluated. Finally, a novel approach of obtaining a-BTO via an alternative buffer and substrate is proposed. The subject of each of the following chapters is described below:

Chapter 2: The growth techniques used in this thesis are introduced and compared. Also, the different characterization methods for the grown material are included.

Chapter 3: The fundamental challenges of perovskite oxide integrated on Si using MBE will be addressed. First, the epitaxy of STO buffer layer on Si is studied in detail, and the delicate oxide / Si interface control will be investigated.

Moreover, the source oxidation effect which relates to stoichiometry stability will be discussed based on different thermodynamic parameters of metal oxidation.

Chapter 4: The BTO grown by MBE will be investigated, including stoichiometry, strain, and optical properties. These characteristics will be further studied to correlate the impact on the EO response in terms of defectivity and domain orientations.

Chapter 5: Another approach for obtaining BTO thin film using PLD will be elaborated in this chapter. The change of BTO properties based on different PLD growth parameters will be examined.

Chapter 6: Alternative buffer and substrates are used to control the BTO orientation. The new buffer layer SrZrO_3 (SZO) grown on a Ge substrate will be investigated. After the optimization of the SZO buffer, the BTO active layer using MBE will be grown on this new buffer layer to compare SZO with STO as a buffer layer. The resulting change in crystallinity and strain orientation will be studied in detail.

Chapter 7: Conclusion and outlook for future study.

Chapter 2

Epitaxy, Crystal Growth Techniques and Characterization Methods

2.1 Introduction to Epitaxy

Epitaxy is a specific type of thin-film growth with the newly grown atomic layer following the crystal orientation of the seed layer or substrate, forming a crystalline film with the lattice all aligned in a certain orientation. If the substrate and epitaxial layer are the same material, it is called “homoepitaxy,” while when the material of the grown layer differs from the substrate, the process is called “heteroepitaxy.” In this thesis, the perovskite oxides grown on a Si substrate is a heteroepitaxy process, with the vapor form of the growth material being transported and deposited on the substrate at elevated temperature in vacuum. When atoms or molecules are transported to the substrate, the deposition is mainly determined by kinetic processes, and the schematics of some possible reactions are shown in Figure 2.1[73]. As the atoms approach the sample surface, they will first form weak van der Waals bonds, which is called the physisorption process. After the physical adsorption, the chemisorption will take place, with stronger chemical bonds being formed.

As the atoms start to arrange on the sample surface, the growth mode will be influenced by the surface energy, which can be categorized to three different modes as illustrated in Figure 2.2[74]. When the atoms are more attracted

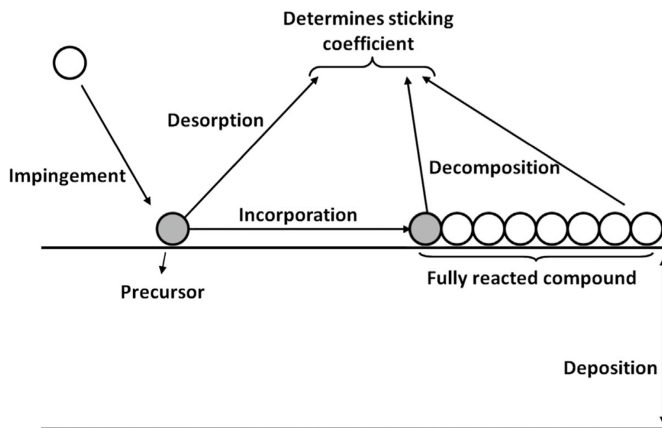


Figure 2.1: Schematic of vapor species at the sample surface during deposition. The figure is adapted from Ref.[73].

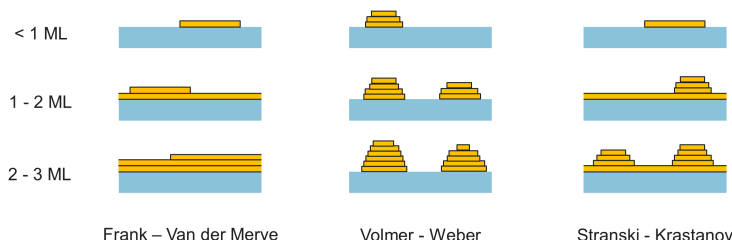


Figure 2.2: Schematic of different growth modes based on the surface energy differences. The figure is adapted from Ref.[74].

to the substrate, the growth mode will mainly be 2-dimensional (2D), and layer-by-layer growth will be observed. On the contrary, if the layer atoms are more attracted to each other, the 3D growth will start at the beginning of nucleation.

The growth mode can be roughly estimated based on the surface energy differences between the substrate, growth layer, and the interface. The schematic between these surface energies is shown in Figure 2.3, and the correlation can be written according to Young's relation[75]:

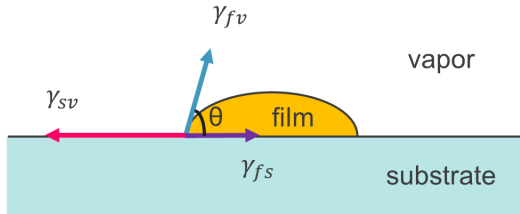


Figure 2.3: Schematic of the surface energy correlation between vapor, substrate, and the grown film. The variations in these surface energies affect the growth mode to be 2D, 3D, or the mix. The figure is adapted from Ref.[75].

$$\gamma_{sv} = \gamma_{fs} + \gamma_{fv} \cos \theta \quad (2.1)$$

where the indices f, s, and v refer to the film, substrate and vapor respectively. γ is the interface energy, and θ is the contact angle. If γ_{sv} is larger than the sum of the other terms, the film obtains a complete “wetting” on the surface, resulting in 2D growth. On the contrary, if γ_{fs} is much larger, the deposited material will tend to form 3D islands to minimize the contact area with the substrate[74]. In between these two conditions, the Stranski-Krastanov mode shows that the film starts with 2D growth, and changes to the 3D mode when the thickness increases. The change in correlation can result from the accumulation of strain inside the films. The growth modes can also be affected by kinetic factors, such as substrate temperature and growth rate, which will be discussed in more detail in the following chapters.

2.2 Growth Technique

In this study, the perovskite oxides are grown by Molecular Beam Epitaxy (MBE) and Pulsed-Laser Deposition (PLD) techniques. The fundamental principles of these two growth techniques and the related monitoring characterizations will be introduced in the following section.

2.2.1 Molecular Beam Epitaxy

The use of MBE system for epitaxial growth was first developed using the GaAs and III-V materials systems[76, 77]; afterwards, with further improvements of

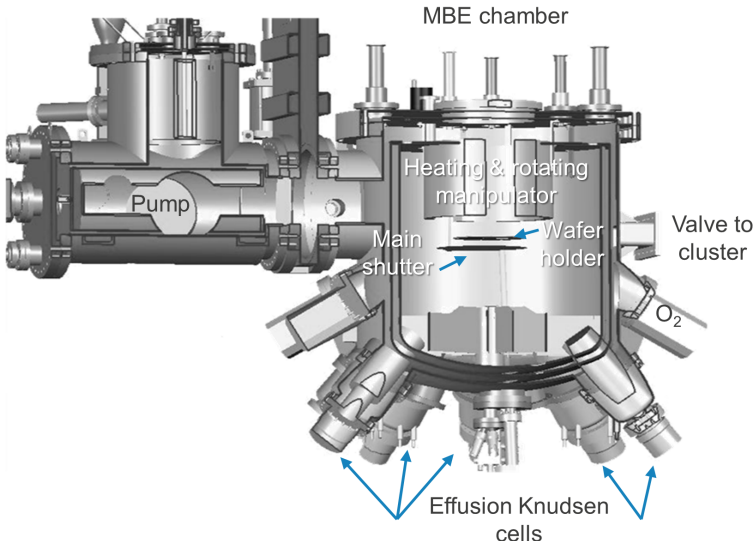


Figure 2.4: Side-view schematic of MBE Riber49 200 mm oxide chamber

the MBE systems and cleaning procedures of substrates, the growth of other materials such as functional oxides on various substrates were demonstrated as well. In MBE system, the chamber pressure is ultra-high vacuum (UHV) with the base pressure in the 10^{-10} Torr range, creating a mean free path larger than 10^5 m. In combination with Knudsen cell which can control the source temperature easily and precisely, MBE provides good atomic control on the growth process. Moreover, with the excellent controllability and UHV, MBE can also study the surface structure in combination with characterization techniques such as Reflection High-energy Electron Diffraction (RHEED) and X-ray Photoelectron Spectroscopy (XPS). With these features, MBE shows to be a powerful tool for realizing high-quality epitaxy with precise interface control and is our principal growth technique in this work.

A 200 mm MBE Riber49 Oxide system is used in this thesis with base pressure of 10^{-10} Torr. Prior to the growth, the Si substrate is cleaned with diluted 2 % HF before introducing into the load-lock and transferred to the epitaxy module once the pressure reaches 5×10^{-7} Torr in the load-lock. During the growth, the Sr and Ba sources are evaporated from double filament effusion cells, while the high-melting-point metals Ti and Zr are produced by electron beam evaporators.

The oxide chamber schematic is shown in Figure 2.4. The effusion cells are located at the bottom of the reactor and directed toward the wafer center. Oxygen is introduced to the chamber, and a remote plasma is applied in some of the growth process (mainly for BTO layer growth) to produce atomic oxygen for more complete oxidation. During the growth, the substrate is heated by a filament to provide sufficient energy for the epitaxy growth with the maximum temperature around 900 °C. For stoichiometry control, the metal fluxes are calibrated prior to the growth with a Quartz Crystal Microbalance (QCM); also, during the growth, fluxes are monitored from the Cross Beam Source Quadrupole Mass Spectrometer (XBS or QUAD) in order to obtain stoichiometric films. In combination with the real-time RHEED monitoring of crystal states, the perovskite oxides epitaxy can be well-controlled and adjusted in real time.

Quartz Crystal Microbalance (QCM)

A QCM is used to measure fluxes from each metallic source independently. For this, the QCM is introduced into the chamber just below the wafer center position. When measuring the fluxes, the metal atoms adsorb on the quartz electrode surface, which will affect its resonance frequency and is translated into a change in mass[78]. By measuring the thickness change over time, we can calculate the average fluxes from each element. The flux ratio between the different elements determines the stoichiometry of the film, which is crucial for the epitaxy quality of the perovskite oxide materials.

Cross Beam Source Quadrupole Mass Spectrometer (XBS or QUAD)

The XBS is a mass spectrometer which measures the mass-to-charge ratio of the molecules. The XBS consists of 4 parallel metal rods which are arranged in a circular form, and the rods opposite to each other are connected electrically. A radio frequency (RF) voltage is applied on the rods with a voltage offset present between these two sets of rods. When ions are passing through the quadrupole, the alternating field creates an oscillating trajectory, and only a narrow range of mass-to-charge (m/z) ratio is allowed to reach the detector without colliding with the metal rods[79]. The XBS is located close to the metal sources, thus we can monitor the partial pressure from the sources in real time. In addition, the pressure from electron beam evaporator is controlled by feedback loop, which ensures the flux stability during oxide growth.

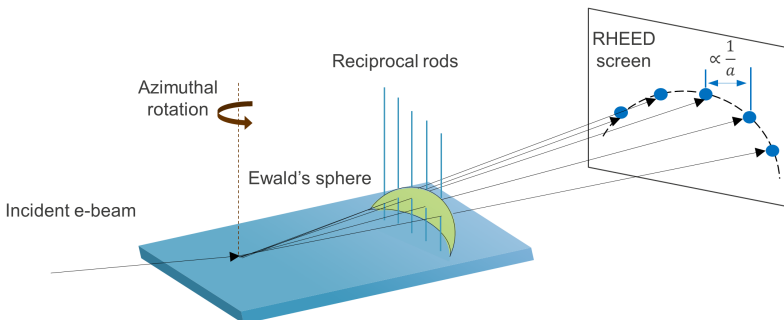


Figure 2.5: Schematic of RHEED pattern formation. The spacing between signal spots on the RHEED screen is proportional to the inverse of material plane spacing (denoted as " a "). The illustration is adopted from Ref.[81].

RHEED

RHEED is widely used in combination with MBE to in-situ monitor the growth status of thin films. The schematics of RHEED in MBE is illustrated in Figure 2.5. With a grazing incident angle, this technique is very sensitive to the surface condition. The electron beam first diffracts from the sample lattice following Bragg's law, then reflects onto the phosphorous screen allowing direct observation of the diffraction pattern from the sample surface. From the crystal diffraction theory, the Ewald's sphere diameter is inversely proportional to the incident wavelength. Thus, for the RHEED high-energy electron beam (20 kV), the constructed Ewald's sphere is relatively large, resulting in multiple intersects with the reciprocal rods of the sample[80]. Due to imperfections at the surface, the diffraction pattern of a single crystalline sample showing on the screen becomes lines with a periodicity proportional to the inverse of the spacing between diffraction planes.

RHEED is very useful to monitor the growth behavior including kinetics, surface reconstruction and crystalline status change. Figure. 2.6 shows RHEED patterns corresponding to different crystalline status. The single-crystalline sample shows clear diffraction lines or streaks with dark background, while the poly-crystalline sample possesses an additional ring-shaped pattern with brighter background. For the amorphous sample, only a diffuse background without diffraction lines is observed. Importantly, the sample is rotated during the growth for better layer uniformity, thus the RHEED patterns change according to diffractions from different directions. As a result, we can obtain orientation-dependent information, including the in-plane lattice parameter and surface reconstructions

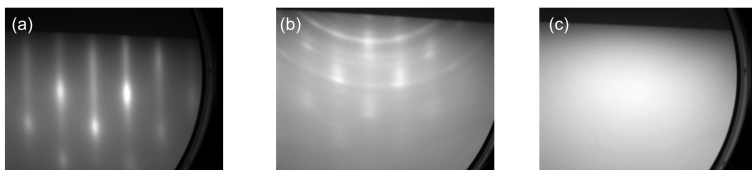


Figure 2.6: RHEED pattern of (a) single-crystalline: streaks (b) poly-crystalline: rings and (c) amorphous: diffuse sample

changes during the growth.

2.2.2 Pulsed-Laser Deposition

PLD is a physical vapor deposition (PVD) technique using a high-energy laser to ablate the target material for deposition. Compared with other PVD techniques such as sputtering, the PLD-grown thin film is known to have a very similar composition as the target material due to the deposition of all thermally melt-out species[82]; in addition, the working pressure can reach 10^{-2} Torr, making this technique a promising candidate for functional perovskite oxides growth.

In this thesis, a 200 mm production PLD system from Solmates is used, and the essence of PLD is illustrated in Figure 2.7. The laser beam is produced by a KrF excimer laser and focused on the ceramic BTO target. With high incident energy, all the target materials are ablated and form a plasma plume in between target and substrate. The substrate is heated during the deposition for epitaxial growth, and the oxygen gas is introduced to compensate the oxygen deficiency in vacuum environment. With higher ambient pressure, the high-energy species in the plume will collide more and lose energy, thus varying the pressure can also affect the kinetic behavior of the deposited species[83].

2.3 Physical Characterization

2.3.1 X-ray Diffraction

X-Ray diffraction (XRD) is a characterization method using an X-ray beam to probe the crystal structure of the sample. This technique is very powerful since

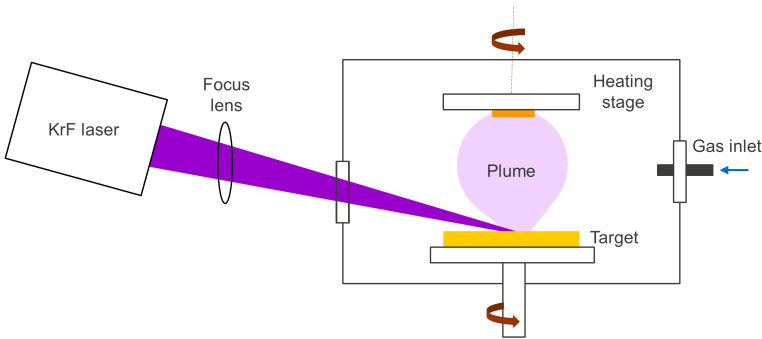


Figure 2.7: Schematic of PLD adopted from Ref.[83].

it can identify the crystal states and phases without destructively affecting the sample. XRD characterization follows the Bragg's law with the equation:

$$2d \sin \theta = n\lambda \quad (2.2)$$

where d is the distance between two parallel atomic planes, θ is the incident angle of the X-ray beam, λ is the wavelength and n is the diffraction order (an integer). The X-ray diffraction with lattice atoms is illustrated in Figure 2.8. When the Bragg's law is satisfied, which means the path difference is equal to an integer number of the wavelength, the X-ray beams from parallel atomic planes will interfere constructively; otherwise, the beams will destructively interfere with each other, resulting in the absence of diffracted signals. With a constant incident wavelength, only a specific angle can satisfy the Bragg's law from a certain plane series. By varying the incident angle, we can detect several peaks, which enables us to identify the structure and phase of the film when comparing the results with literature data.

The XRD used in this thesis is a Panalytical X'pert Pro diffractometer. In this tool, the detector scanning and the holder rotation directions relative to the incident X-ray beam are depicted in Figure 2.9. With different scan orientations, we can extract more detailed information about the grown thin film. The scans used in the thesis are listed below:

1. ω - 2θ scan: the detector will move an angle double to θ in order to collect the signal. This scan is used to verify the crystal phases and can be used to calculate lattice parameters. The scan can be roughly divided into a

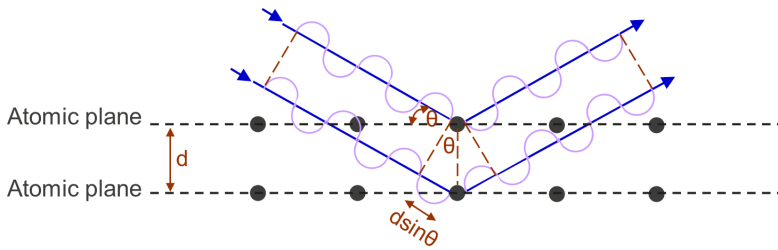


Figure 2.8: Schematic of Bragg's condition. Constructive interference only occurs when $2ds\sin\theta = n\lambda$ is satisfied.

symmetric and asymmetric process, with the symmetric scan measuring the planes parallel to sample surface while the asymmetric scan measuring the planes that contain the in-plane orientation information.

2. ω -scan: the measurement is carried out with only small variation of ω around a certain 2θ peak position while keeping the detector unmoved. In this way, the mosaicity of the film can be determined by the full width at half maximum (FWHM) of the peak, with the narrower one referring to the better crystallinity.
3. φ -scan: a full 360° φ -scan of a certain asymmetric peak can provide information about the rotation symmetry of the material, which is an important information related to the crystalline status of single or polycrystalline film.
4. Reciprocal space mapping (RSM): this scan is the combination of ω - 2θ scan and ω -scan, which allows us to visualize the Bragg reflections in the reciprocal space. The measurement is useful for strain analysis.

When performing the measurement, the peaks originating from the Si substrate are used to calibrate the tool alignment and the measured results will be shifted based on the Si theoretical peak positions. In addition, since the perovskite oxide layers are 45° rotated relative to the substrate (in-plane), for the asymmetric scan, we will first align the Si(202) peak and then rotate 45° in φ to do the perovskite oxide (202) ω - 2θ scan.

The lattice parameters of perovskite oxides are calculated by XRD using both the symmetric and asymmetric scans. In this thesis, the out-of-plane lattice parameter is calculated using the BTO(002) peak and the in-plane lattice

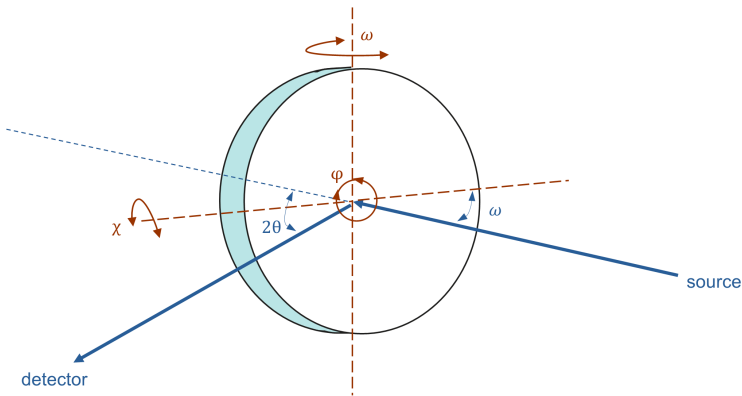


Figure 2.9: Schematic of the different angular manipulations of the XRD measurement stage.

parameters are calculated from BTO(202) and BTO(022) peaks. After obtaining the d-spacing from equation (2.2), the out-of-plane lattice parameter c can be calculated by the following equation[84]:

$$d_{002} = \frac{c}{\sqrt{h^2 + k^2 + l^2}} = \frac{c}{2} \quad (2.3)$$

After obtaining c , we then can further calculate the in-plane lattice parameters based on the equation related to the tetragonal structure[84]:

$$\frac{1}{d_{hkl}^2} = \left[h^2 + k^2 + l^2 \left(\frac{a}{c} \right)^2 \right] \frac{1}{a^2} \quad (2.4)$$

The in-plane lattice parameters for the x - and y -directions are calculated respectively from the (202)- and (022)-scans.

However, in our asymmetric scans, other than the perovskite oxide and the Si peaks, we also observed additional peaks. To verify if the peaks are correlated to poly-crystallinity of the deposited film or originating from the measuring tool, a blanket Si substrate with only SiO_2 native oxide on top is used to perform the same measurement. As shown in Figure 2.10, the additional peaks observed in between the BTO(101) and BTO(202) peaks appear in the same scan of the bare Si wafer. These two peaks also appear in the other perovskite oxide

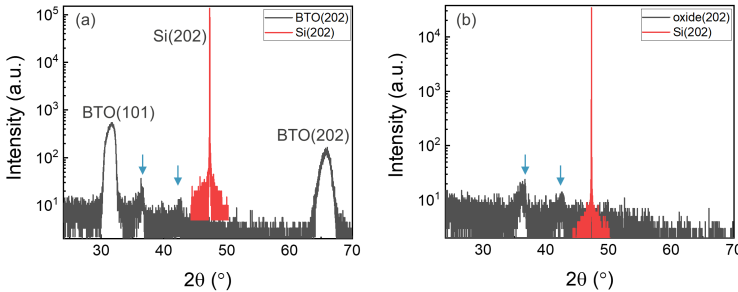


Figure 2.10: Asymmetric XRD (202)-scan of (a) BTO / STO / Si and (b) bare Si with only native SiO₂ on top. The additional peaks are coming from the measurement tool instead of poly-crystalline BTO.

films used in this thesis, and will not be regarded as peaks originating from poly-crystalline states, thus will not be further discussed.

X-ray Reflectivity (XRR) is also a characterization method using X-rays which can measure the sample thickness. With small incident angle, the X-ray will have total reflection within the film, and only when the incident angle is larger than the critical angle, the intensity starts to decrease. When measuring thin films, the density differences in each layer cause different reflections, which interfere with each other and result in the intensity oscillation during the scan[85]. Thus, these oscillations (Kiessig fringes) will be affected by the thickness and density of each layer, which can be revealed by analyzing the XRR curve. Typical XRR curve is plotted in Figure 2.11. The critical angle θ_c is mainly related to the density of the film while the oscillation amplitude is related to the density differences between the thin film and the substrate[86]. Moreover, the oscillation period provides the information of film thickness, and the decay rate is largely related to the surface roughness. The XRR curve can be fitted, and by analyzing and comparing with the measured curve, we can extract the information for each layer, including interfaces quality, the roughness, density, and thickness from this measurement.

2.3.2 Atomic Force Microscopy

Atomic force microscopy (AFM) is used to measure the samples surface roughness. For the VH application, the surface roughness criterion for the epitaxial film is expected to be smaller than 1 nm, which is set in order to

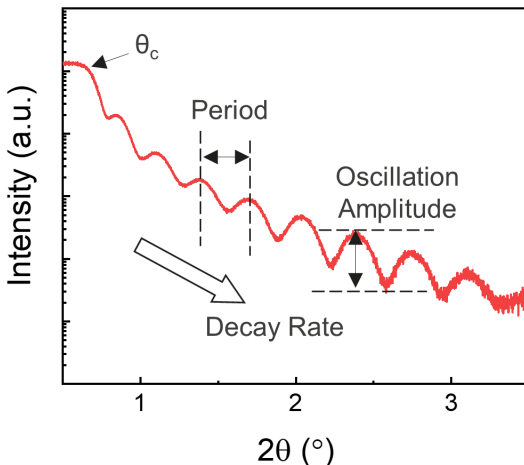


Figure 2.11: Typical XRR curve. The grown film thickness can be extracted from the periodicity, and the surface roughness is obtained from the decay rate.

enable the subsequent wafer bonding process. In the measurement, the AFM probe tip is scanning the surface and measures the atomic force between tip and surface atoms. The atomic force changes when the distance between tip and surface changes, thus influencing the laser position shining on top of the cantilever. Thus, by monitoring the reflected laser beam, the surface roughness over the scanned area can be extracted. A schematic of the AFM setup is shown in Figure 2.12(a). The resolution of AFM can be on atomic scale due to high sensitivity of the change in atomic forces. Figure 2.12(b) shows the step and terraces of the surface of an epitaxial STO film on Si(001) by AFM, revealing a step height of ~ 4 Å.

2.3.3 Piezoresponse Force Microscopy

The setup of piezoresponse force microscopy (PFM) is similar to that of AFM but now with a direct contact and the usage of a conducting tip, which is specially used for the characterization of piezo or ferroelectric materials. When conducting the PFM measurement, the tip will contact the sample and an AC electric field is applied. This AC field will induce the piezo effect, affecting

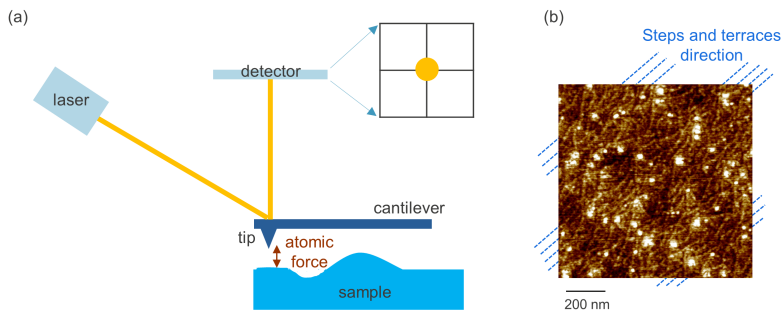


Figure 2.12: (a) Schematic of AFM and (b) a high resolution image of steps and terraces measured by AFM on an annealed STO surface grown on a Si(001) substrate.

the final tip position and the subsequent beam deflection, producing images correlated to the magnitude of the piezo effect[87].

The PFM measurement in this thesis is based on the usage of a heavily doped Si substrate and metal coated tip contacting the top surface, thus the electric field is perpendicular to the surface inside the sample. Thus, for our PFM measurement, only the domains along the same direction (c-oriented) as the applied electric field will response.

2.3.4 Stoichiometry Characterization

Regarding the MBE-grown film, the stoichiometry largely affects the film crystallinity and defectivity, resulting in deviations in the physical and optical characteristics. In this thesis, the stoichiometry is measured by Rutherford backscattering spectrometry (RBS) and particle-induced X-ray emission (PIXE). For RBS, the incident high-energy alpha particle beam will be scattered by the nuclei in the sample, thus the detected particle energy will be correlated to the nuclei mass and atomic number of the nuclei it has interacted with. By comparing the detected peak energy and peak height intensity to the known scattered cross-sections, RBS not only can analyze which element is present in the sample, but also quantitatively the amount of the element[88].

However, for elements with similar mass such as Sr and Zr involved in this thesis, RBS cannot distinguish these peaks. Instead, PIXE is used to quantify the amount of Sr and Zr, in which a similar setup as for RBS is used, but with now the detection of the emitted characteristic X-ray. When the alpha particles with

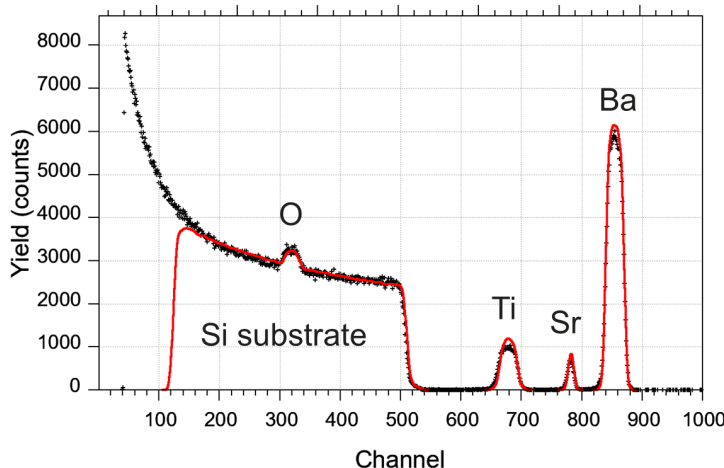


Figure 2.13: Typical RBS profile observed from a BTO / STO / Si sample. The black dots are obtained from the real measurement, while the red curve is created by simulation. The spectrum shows different elemental peaks ranging from small to large energy along the x-axis, while the count in y-axis is proportional to the amount of each element inside the sample. The simulation is modelled to a depth in the substrate $\sim 1 \mu\text{m}$ because of no useful information below this point, thus a deviation between the curves will be observed in the low energy part of the spectrum.

high-energy hit the sample, the inner shell electrons will be ionized, resulting in outer shell electron filling of the inner shell vacancy with attendant emitting of characteristic X-rays[89]. Similar to RBS, by analyzing the emitted X-ray energy and intensity, we can characterize the element present in the thin film. A typical RBS profile from a BTO / STO / Si sample is shown in Figure 2.13.

2.3.5 Transmission Electron Microscopy

The main application of using transmission electron microscopy (TEM) in this thesis is imaging on atomic resolution scale and performing strain analysis. The electron energy in TEM is very high ($\geq 100 \text{ keV}$), which results in a small wavelength and the possibility to achieve high resolution atomic imaging. The TEM sample is very thin, and the electron beam will penetrate the whole sample, finally reaching the detector underneath for further analysis. The

imaging can be switched from bright field (BF) to dark field (DF) by using respectively the direct beam and the diffracted beam, and the reversed contrast can be used complementarily depending on the different types of analysis[90]. High-resolution TEM (HRTEM) imaging is using the direct beam while the high-angle annular dark-field (HAADF) imaging is using the diffracted beam. Compared with HRTEM, the HAADF is collecting the diffracted beam at higher angle. Due to the dominant Rutherford scattering at high angle, the diffracted electron energy is proportional to the atomic number (Z), thus the contrast observed in HAADF image can be directly linked to the different elements in the perovskite lattice[91].

In addition to imaging of the epitaxial film, the TEM is also used to analyze the localized strain by using the nano-beam diffraction (NBD) technique. By focusing the beam to a very small size under Scanning TEM (STEM) mode, the diffraction spot will be measured to obtain the localized lattice parameter. Upon comparing the lattice parameters for the strained and un-strained parts in the specimen, the strain magnitude and direction can be determined[92].

2.3.6 X-ray Photoelectron Spectroscopy

The X-ray photoelectron spectroscopy (XPS) is a surface sensitive analysis using X-rays with known incident energy and measures the emitted electrons that absorb sufficient energy from the X-ray to escape from the atom. The energy difference between emitted and incident beam can be written as:

$$E_{binding} = E_{photon} - E_{kinetic} - \varphi \quad (2.5)$$

where φ is related to the work function of the species and the instrument[93]. By measuring the kinetic energy of the emitted electrons, the chemical binding energy can be calculated. This analysis is surface sensitive with the a penetration depth of ~ 10 nm since only electrons close enough to the surface can escape while electrons from bulk will eventually collide inelastically and lose energy. Actually, the penetration depth can be further adjusted by changing the incident angle with the sample. As shown in Figure 2.14, using different incident angles of the X-ray beam to the sample, the sampling depth can be controlled. With the same escaping depth, the electrons in the more tilted sample will travel longer before escaping from surface, thus the detection depth is reduced[94]. In our XPS experiments, two incident angles (78° and 21°) have been applied based on the interface position and film thickness.

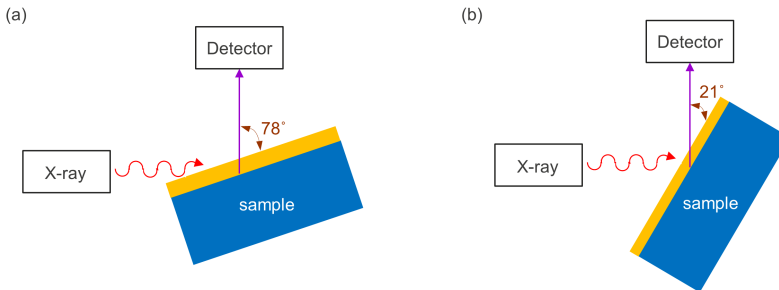


Figure 2.14: XPS with two different incident angles, resulting in (a) larger sampling depth and (b) smaller sampling depth.

2.4 Electrical Characterization

The electrical measurement is carried out by means of additional deposition of metal top and bottom electrodes. In this thesis, the top electrode is Au and the backside of the sample is covered with an Al film to reduce the contact resistance. In the measurement, the electrical potential is applied through the top electrodes while the backside is connected to the measurement chuck and grounded. The top electrode is circular with diameter ranging from 500 μm to 60 μm and is defined via usage of a shadow mask during the metal evaporation.

The current-voltage (I-V) measurements are carried out using an Agilent B1500A source. During the measurement, the voltage is applied on the electrodes, and the current is recorded and translated to current density for further comparison.

Capacitance-voltage (C-V) measurements are used to characterize the insulator dielectric properties. With the same electrode configuration, the C-V is measured by an Agilent E4980A tool with the frequency being varied from 1 kHz to 1 MHz.

2.5 Optical Characterization: Spectroscopic Ellipsometry

Woollam RC2 Spectroscopic Ellipsometry (SE) and the software CompleteEASE are used to extract the optical indices presented in this thesis. When the light passes through the sample, due to the change of refractive index, the polarization

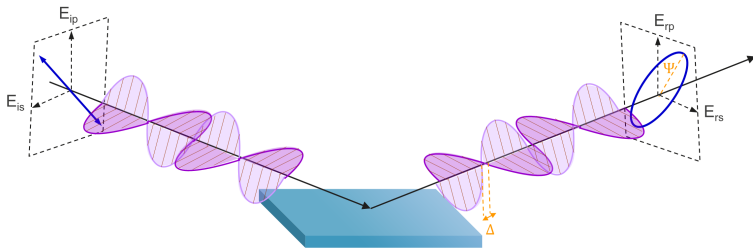


Figure 2.15: Illustration of Ellipsometry. The polarization changes after the beam interacts with the sample.

of the beam will be affected. As shown in Figure 2.15, the beam can be divided to *p*- and *s*-polarization, which are orthogonal to each other, based on the incident plane to the sample. As shown in Figure 2.15, both the phase shift and amplitude differences between the reflected *p*- and *s*-polarization wave will result in the final beam polarization change, which will be recorded by the SE detector. The *p*-over-*s* ratio of the reflected beam can be defined by the equation:

$$\rho = \frac{r_p}{r_s} = \tan \Psi \cdot e^{i\Delta} \quad (2.6)$$

in which $\tan \Psi$ is the reflected beam amplitude ratio and the Δ is the phase shift[95]. In our measurement, the incident angle is varied from 45° to 85° , and at each angle the wavelength is scanning from 200 nm to 2500 nm. As a result, more than 10k of data points are obtained for each measurement.

Although the change in polarization is the result from a change in refractive indices of the sample, the relationship between measured data and physical refractive indices is not straight-forward. To obtain the refractive indices n and extinction coefficient k , a model based on the film stacking and interfaces is necessary. With the input of roughness and thickness of each layer, the simulated curves are calculated by the CompleteEASE software. By minimizing the differences between the simulation and measured curves, we could eventually extract the desired indices of each layer involved. The fitting procedure is summarized in Figure 2.16.

The fitting error is calculated by the CompleteEASE software using the equation[96]:

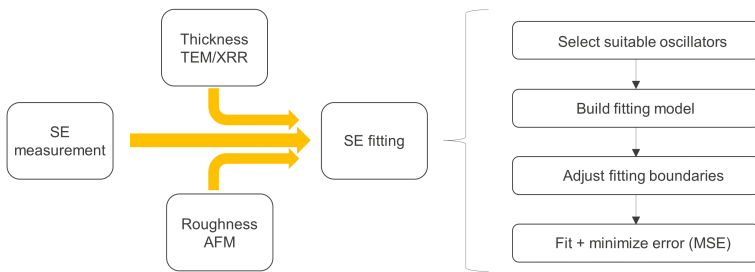


Figure 2.16: Fitting procedure used for SE.

$$MSE = \sqrt{\frac{1}{3n-m} \sum_{i=1}^n \left[\left(\frac{N_{E_i} - N_{G_i}}{0.001} \right)^2 + \left(\frac{C_{E_i} - C_{G_i}}{0.001} \right)^2 + \left(\frac{S_{E_i} - S_{G_i}}{0.001} \right)^2 \right]} \quad (2.7)$$

where n is the number of wavelengths, m is the number of fit parameters, and $N = \cos(2\Psi)$, $C = \sin(2\Psi) \cos(\Delta)$, $S = \sin(2\Psi) \sin(\Delta)$. The measured data are denoted with E and the model generated data are denoted with G . The MSE value depends not only on the consistency between measured and model data, but also on the complexity of film stacking. In this thesis, all the MSE values obtained are smaller than 10, with generally the simpler the stacking, the smaller the final MSE values.

Chapter 3

Fundamental Challenges of MBE-grown Lattice-matched Oxides on Silicon

The epitaxy of perovskite oxides on Si substrate requires extreme control such as elemental stoichiometry, substrate temperature, and pressure in the MBE chamber. Not only due to the fast silicon oxidation and stability of the formed SiO_x in the Si surface, but also because of the crystal structure mismatch between the Si diamond and the oxide perovskite, the perovskite epitaxy on Si is a real challenge. Other than the problems with interfacial and structural control, during the oxide growth, the metallic sources will also be oxidized due to the environment thus causing stoichiometry stability issues. In the last part of this chapter, the source oxidation effect will be extensively discussed, and detailed experimental results will be provided.

3.1 SrTiO_3 as Buffer Layer for Perovskite Oxides Integration

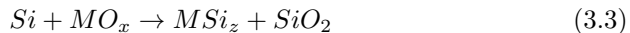
3.1.1 Sr-on-Si Surface Interaction

When integrating functional oxides on a Si substrate, not all elements are thermodynamically stable in contact with Si. D. Schlom et al. investigated the

H																					He
Li	Be																				
Na	Mg																				
K	Ca	Sc	Ti	V	Cr	Mn	Fe	Co	Ni	Cu	Zn	Ga	Ge	As	Se	Br	Kr				
Rb	Sr	Y	Zr	Nb	Mo	Tc	Ru	Rh	Pd	Ag	Cd	In	Sn	Sb	Te	I	Xe				
Cs	Ba	†	Hf	Ta	W	Re	Os	Ir	Pt	Au	Hg	Tl	Pb	Bi	Po	At	Rn				
Fr	Ra	‡	Rf	Ha	Sg	Ns	Hs	Mt													
		†	La	Ce	Pr	Nd	Prm	Sm	Eu	Gd	Tb	Dy	Ho	Er	Tm	Yb	Lu				
		‡	Ac	Th	Pa	U	Np	Pu	Am	Cm	Bk	Cf	Es	Fm	Md	No	Lr				

Figure 3.1: Summary of stability of elements in contact with Si. The thermodynamically unstable MO_x on Si are shaded in blue. Elements with pink letters lack thermodynamic data to complete the calculation, while the ones with yellow background have experimental demonstrations. This figure is adopted from Ref.[97].

element stability with Si, including the oxide and nitride forms, by calculating the Gibbs free energy of the pertinent chemical reactions. For example, as to in the M-O-Si system, the possible reactions of an element M without considering the formation of ternary phases are listed as followings[97]:



An element is stable on Si when all the Gibbs free energies are above 0 (kJ/mol) in these equations, and the results are summarized in Figure 3.1. Combining both calculation and experimental results, only few elements remain stable on Si without resulting in the formation of silicide (MSi), silicate (MSiO) or silicon oxide (SiO_x) when heating up to 1000K. This study shows that the Ba and Ti are not thermodynamically stable on Si, thus a buffer layer is required for which only a small fraction of elements is feasible. Based on the study results, Sr is stable on Si, providing a solid base for using SrTiO_3 as buffer layer to integrate perovskite oxides.

When Sr is in contact with Si, the amount of Sr shows a large impact on the top surface with the formation of various surface reconstructions as a function

of the Sr quantity. On the pristine (100) silicon surface, due to the symmetry breaking, each Si atom possesses two electrons with no bonding. These dangling bonds would further decrease their energy by forming silicon dimers with two silicon atoms bonded to each other, resulting in the formation of parallel dimer rows along the [110] direction, thus creating two two times the periodicity of that in bulk[98, 99]. At the same time, the Si rows perpendicular to these dimer rows will keep the same periodicity, forming the (2 × 1) reconstruction on the Si surface. This surface reconstruction can be observed on pristine Si surface without native oxide. The initial (2 × 1) surface reconstruction will be modified as a function of the Sr exposure and temperature. The detailed surface change was studied thoroughly by various groups using different approaches including ab-initio calculation and thermodynamic energy comparison[100, 101, 102]. When Sr atoms are introduced, the Si surface reconstruction slowly changes from (3 × 2) to (2 × 1) with the Sr coverage changing from 1/3 to 1/2 mono layer (ML) as shown in Figure 3.2[102]. The 1/2 ML coverage reaches a localized minimum energy state with Sr atoms sitting in between the Si dimer rows. This reconstruction is not only thermodynamically stable but will also act as the template which enables the transition from the Si diamond structure to the subsequent perovskite STO, as will be shown later.

Moreover, the 1/2 ML Sr covering Si(001) surface prevents it from the immediate oxidation and formation of an amorphous SiO_x layer. The surface oxidation for different Sr coverage amount has been examined, and the results show that with 1/2 ML coverage, the surface forms a crystalline silicate – in contrast to other coverages which form SiO₂ thus preventing the further epitaxial growth of the perovskite STO layer[103, 104].

3.1.2 SrTiO₃ on Si

Other than stability, the buffer layer plays an important role in strain manipulation as well as lattice mismatch reduction between functional oxides and a substrate. Bulk STO is cubic at room temperature with a lattice parameter of 3.905 Å. This material is paraelectric having a large dielectric constant, thus it was proposed to be a candidate as high-k gate oxide[104, 105, 106]. However, compared with the Si lattice parameter ($a_{Si} = 5.431 \text{ \AA}$), the lattice mismatch is extremely large (>25 %), making it very hard to control a correct epitaxial growth with cube-on-cube configuration. Thus, the STO relative lattice rotation on Si was proposed and first demonstrated by McKee et al[107]. When the STO is rotated 45°, i.e., with the orientation relationship of [100]_{STO} // [110]_{Si}, the lattice mismatch can be largely reduced to only ~1.7 %. By means of careful control of the Sr coverage, the lattice of STO layer is rotated on Si and an

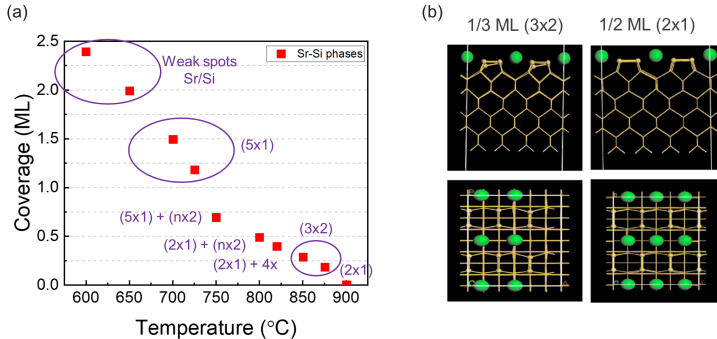


Figure 3.2: (a) Reported Sr / Si phases from 600 °C to 900 °C. This figure links the Sr coverage amount to a certain Si surface reconstruction, which is investigated by the low-energy electron diffraction (LEED). (b) The simulated Si surface reconstruction for different Sr coverages. The figures are modified from Ref.[101, 102].

epitaxial STO layer is achieved by step-by-step growth as illustrated in Figure 3.3.

The STO epitaxy was then further developed by different groups with modifications regarding temperature and pressure range to control the initial stage of the growth. In most groups, the STO epitaxy was achieved with first growing a few unit cells of amorphous STO at low temperature and low oxygen pressure, followed by a thermal annealing to recrystallize the thin STO layer. After the recrystallization, thicker STO films can be grown using both higher temperature and oxygen pressure to improve the crystallinity and dielectric properties. The STO using this two-step growth process showed good quality, exhibiting a small FWHM of the STO(002) peak less than 0.3°[108, 109]. However, the annealing step usually created a thick interfacial layer of SiO_x between STO and Si, affecting the electrical properties and adding concerns for the gate stack application[104, 110, 111]. Moreover, it was shown that during the recrystallization process, extended defects such as anti-phase boundaries were formed at where the crystallite fronts met[112].

Compared with the deposition at low temperature followed by a high-temperature annealing, another alternative was to grow STO directly at intermediate temperature. In 2011, G. Niu et al. demonstrated that under optimized conditions, one could directly grow epitaxial STO on Si without

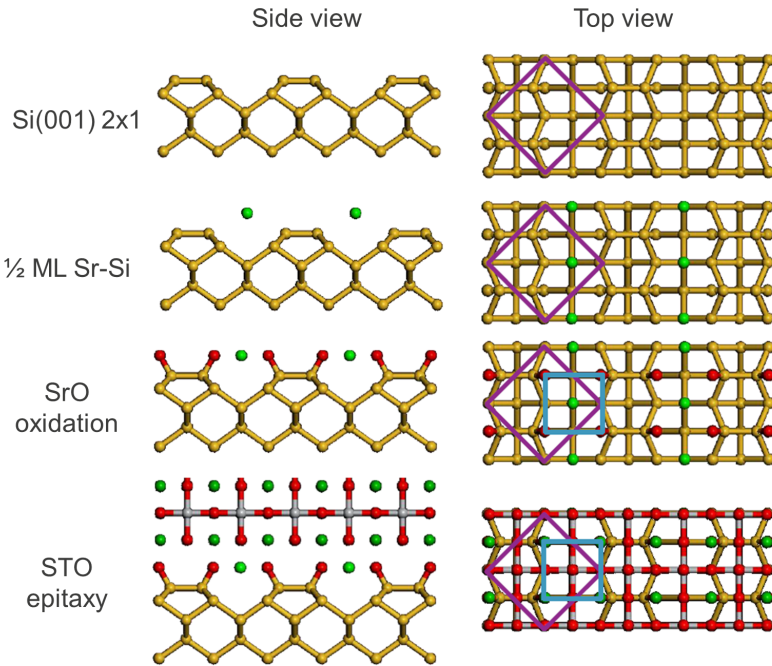


Figure 3.3: Schematic of step-by-step STO epitaxy on Si with the (001)[100]_{STO} // (001)[110]_{Si}. The Sr atoms sit in between the Si dimer rows are gently oxidized into a single SrO layer, which acts as the epitaxial template for the subsequent STO growth.

the additional annealing[113]. However, the direct epitaxy window was very small, thus requiring very precise control of the growth conditions, including temperature, stoichiometry, and oxygen pressure. In the next section, we present detailed studies on the STO direct epitaxy and demonstrate the growth of a high-quality epitaxial STO film with a sharp interface on Si after optimization.

A thermodynamically stable (2 × 1) Sr-Si(001) structure with 1/2 ML coverage can be used as template for STO epitaxy, but it requires careful control of the subsequent growth parameters to maintain this interface intact.

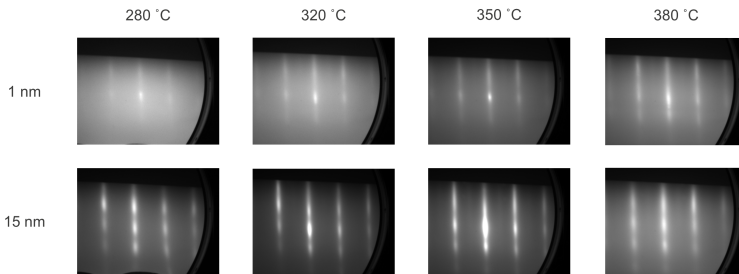


Figure 3.4: RHEED patterns along [110]STO of epitaxial STO at the initial and final stage grown on Si(100) with different substrate temperatures.

3.2 Direct Epitaxial SrTiO₃ Interface Control

3.2.1 Substrate Temperature Optimization

To obtain direct epitaxy, the substrate temperature is first optimized. As has been illustrated by Niu et al., too low a temperature caused amorphous growth, while too high the temperature resulted in an over-active substrate surface and the formation of a thick interfacial layer[113, 114]. In our experiments, we vary the substrate temperature from 280 °C to 380 °C, and RHEED images at the initial and the end stage of growth are shown in Figure 3.4. For the first 1-nm layer growth, the 350 °C growth shows clear RHEED streaks with dark background, while other temperature settings show worse crystallinity with the hint of slight amorphous growth based on the brighter background. After 15-nm growth, the RHEED images all show a higher signal-to-background ratio compared with the initial stage, suggesting a much stable growth after passing the initial stage. The better temperature range is in between 320 °C and 350 °C, with both RHEED images presenting straight streaks and a low background.

These 15-nm STO layers are further analyzed with XRD and AFM, with the characterization results shown in Figures 3.5 and 3.6. In Fig. 3.6, the STO grown at a temperature of 320 °C and 350 °C show a smaller FWHM, which is consistent with the RHEED results; as for the surface roughness, the higher the temperature, the smoother the surface. These results suggest that the optimized temperature is around 350 °C. With too low the temperature, the kinetic energy of deposited atoms is insufficient, thus some parts of the films are still amorphous with worse crystallinity and show a rougher surface.

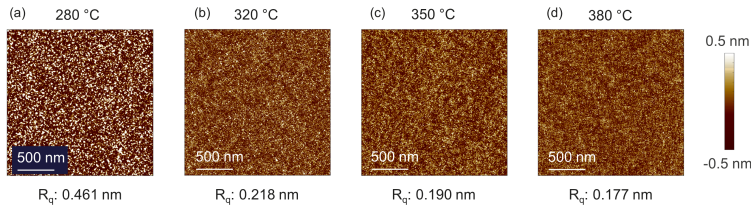


Figure 3.5: AFM images of the surface of STO layers grown at (a) 280 °C (b) 320 °C (c) 350 °C and (d) 380 °C.

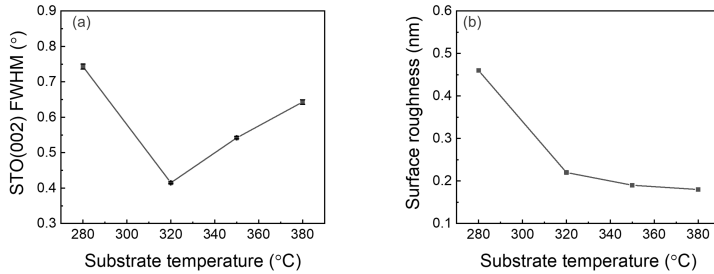


Figure 3.6: (a) FWHM of STO(002) from XRD ω -scan and (b) surface roughness from AFM of STO grown at different substrate temperatures.

On the contrary, with too high substrate temperature, the interactions of atoms with Si become stronger, and the surface is easily oxidized. The formation of amorphous SiO_x in the early stage will hinder the epitaxy, resulting in a thick interfacial layer and worsened crystallinity.

3.2.2 Oxygen Partial Pressure Optimization

Another crucial parameter is the control of the oxygen pressure during the initial stage of growth. The schematic of the STO epitaxy procedure is illustrated in Figure 3.7. Prior to the growth, the Si wafer is cleaned with aqueous 2 % HF for 90 seconds to remove the native oxide, followed by a high temperature annealing (above 650 °C) to completely remove the oxide and impurities, leading to the formation of the silicon dimer rows according to the (2×1) surface reconstruction.

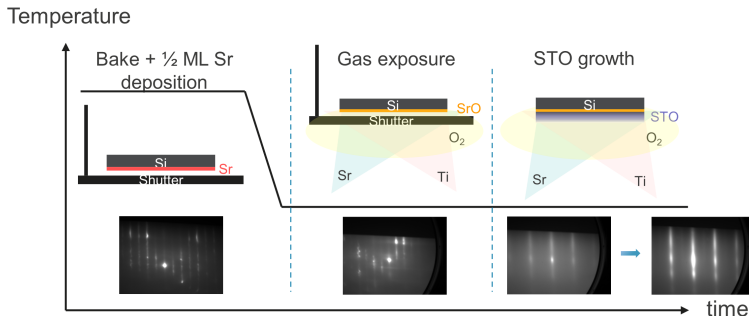


Figure 3.7: Experimental procedure of STO growth.

After these steps, the 1/2 ML Sr is introduced through carefully analyzing the different transitions of the surface reconstructions by RHEED till the reappearance of the targeted (2 × 1) reconstruction of SrSi₂ (see Fig. 3.3). After the Sr-Si template is formed, the substrate is cooled down to the deposition temperature, and the gases of metal sources and oxygen are introduced into the oxide chamber. Before opening the main shutter, the substrate has already been exposed to oxygen ambient, thus the Sr on the surface starts to oxidize and forms SrO for the subsequent STO growth. Here we vary the oxygen exposure amount, and the impact on STO is carefully investigated.

The gas exposure amount is varied by monitoring the pressure as a function of time, and is calculated by the area under the curve in the unit of Langmuir (L), as shown in Figure 3.8. Langmuir is the unit for exposure on the surface, and with the sticking coefficient of 1, one Langmuir corresponds to roughly one ML of coverage. In our STO growth, the exposure amount is varied from 1.5 L to 70 L with the main shutter being closed until a certain amount is reached. The correct oxygen amount is crucial since oxygen is needed for the oxide growth, but cannot be too high as the over-oxidation of the interface and the formation of amorphous SiO_x have to be prevented.

The exposure amount shows a large impact on the STO crystallinity as illustrated in Figure 3.9. For a small exposure amount, the RHEED images show evidence of direct growth during the initial stage with the observation of 2D streaks and low background intensity (Fig. 3.9(a) and (b)). On the contrary, the 25 L exposure only shows diffuse background without any streaks, indicating the deposited film is already amorphous in the first 1-nm growth. The initial stage also affects the following growth of STO, as the 4-nm RHEED images follows the 1-nm ones. The 2 L sample shows the highest signal-to-background intensity

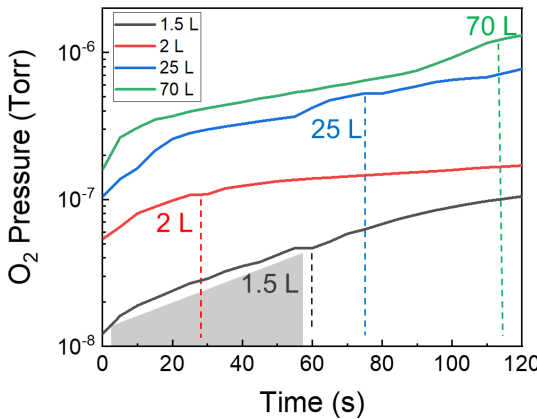


Figure 3.8: Profiles of the oxide pressure in the chamber as a function of time during STO epitaxy. The gas exposure amount is the area under the curve, expressed in the unit of Langmuir (L).

ratio.

In Fig. 3.9(d) and (f), a faint $\times 2$ reconstruction is observed, which results from a slight Sr-rich SrTiO₃ composition. The stoichiometry of STO is analyzed by RBS, and the results are shown in Figure 3.10. All the samples are Sr-rich, and the compositional change with exposure amount will be discussed together with XPS results later. For the 1.5 L and 2 L sample, the slight excess of Sr could in fact be extremely helpful for the STO epitaxy as suggested by Saint-Girons et al., who argued that the SrO / SrO / TiO₂ sequence enhanced the SrTiO₃ epitaxy compared with that for the SrO / TiO₂ stacking[116].

Furthermore, the crystalline and interface status is investigated using TEM. The cross-sectional TEM images for different exposure amounts are shown in Figure 3.11, where it is seen that both the 1.5 L and 2 L samples show sharp and coherent interfaces. Especially for the 2 L sample, the interface transition from the Si diamond structure to the STO perovskite structure is smoother compared with the 1.5 L sample. Combining the results from Figs. 3.9 and 3.11, the 2 L exposed surface demonstrates the optimized exposure amount, which indicates the Sr is thoroughly oxidized and results in an ideal Si-to-STO transition. A fast Fourier transform (FFT) analysis is carried out on both layers, and the measurement between diffraction spots suggests that the STO is fully

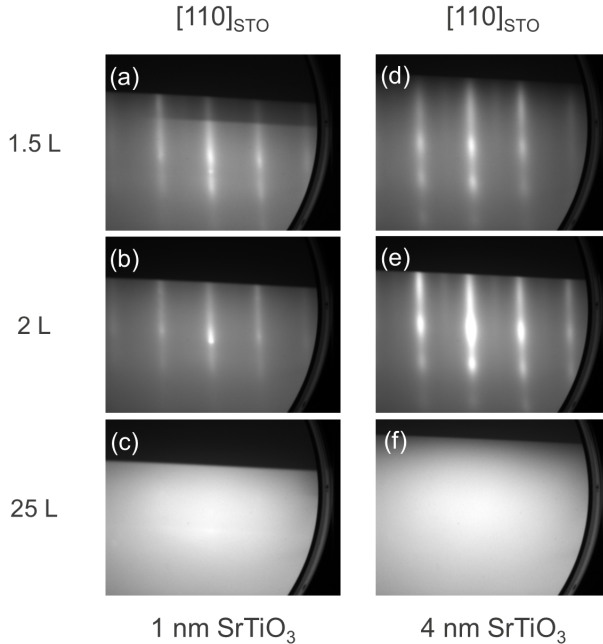


Figure 3.9: RHEED patterns taken for (a)-(c) 1 nm of STO and (d)-(f) 4 nm of STO for different gas exposure amounts. The figure is taken from the previous published work[115].

strained on Si as shown in Figure 3.11(d) and (e). On the contrary, even with 1/2 ML Sr to prevent immediate oxidation, the over-exposure still leads to an amorphous interface and STO layers, as shown in Fig. 3.11(c). The interface is very smooth compared to that of the crystalline sample, which suggests the amorphous layer is already formed during the initial stage of the STO growth.

A XRD analysis is also carried out for the crystalline samples, and the ω - 2θ scan results are shown for 1.5 L exposure STO films in Figure 3.12. Since the film thickness is only 4 nm, the signal from the STO film is small, making it difficult to correctly identify the peak position. Nevertheless, the lattice parameters are extracted, and the out-of-plane lattice parameter of 4.00 Å as well as the in-plane lattice parameter \sim 3.90 Å for the 1.5 L sample is obtained. This value is comparable with the 3.92 Å calculated from the spot distance from the TEM FFT images.

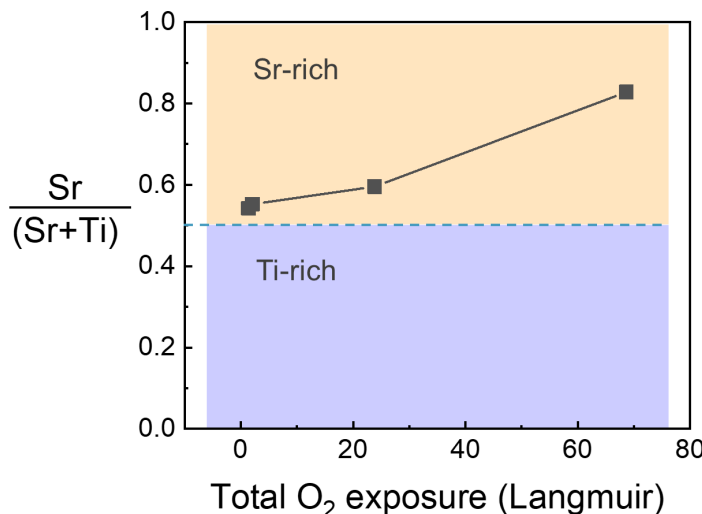


Figure 3.10: Stoichiometry of STO with different exposure amount by RBS analysis.

The STO surface roughness is measured by AFM, and the results are shown in Figure 3.13. All the STO samples are showing very flat surfaces with root-mean-square roughness in the $\sim 0.15 \text{ nm}$ range. There are some small clusters appearing on the 2 L surface, but the surface is still relatively flat with a roughness of only 0.28 nm from the $2 \times 2 \mu\text{m}$ scanning area.

The chemical binding status of the interface can be investigated by small-angle XPS as discussed in Chapter 2 for shallower sampling depth. The change in interface bonding is examined by the Si 2p core level, as shown in Figure 3.14(a). After normalizing the intensity based on the Si-Si main core level, the Si sub-oxides peak intensity shows an obvious rise as the oxygen exposure amount is increased. For the 1.5 L and 2 L samples, the small intensity originates from the Si atoms bonded to the oxygen atoms in the SrO layer right on top of the surface. On the other hand, the large intensity from 25 L and 70 L samples suggests the interface is heavily oxidized, and a thick SiO_x interfacial layer is formed when oxygen overexposes. For the 1.5 L sample, an additional *in-situ* annealing is carried out at a temperature of up to 580°C , which is the targeted growth temperature for the subsequent BTO active layer. The XPS results

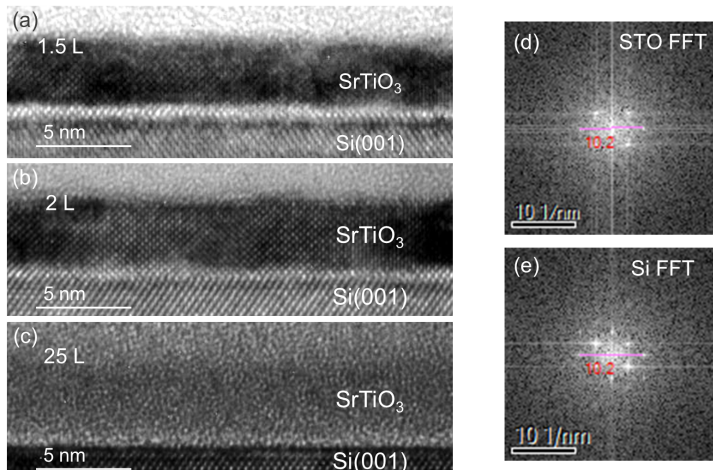


Figure 3.11: The STO cross-sectional TEM images for (a) 1.5 L (b) 2 L (c) 25 L samples. The FFT images are taken on the 1.5 L sample of the (d) STO and (e) Si layer, which show that the STO layer is fully strained on Si. The figures (a)-(c) are taken from the previous published work[115].

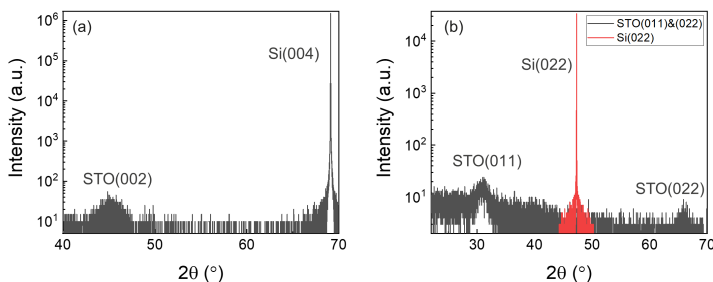


Figure 3.12: 4-nm STO XRD ω -2 θ scan of (a) symmetric and (b) asymmetric (022) plane for STO grown under a 1.5 L exposure amount.

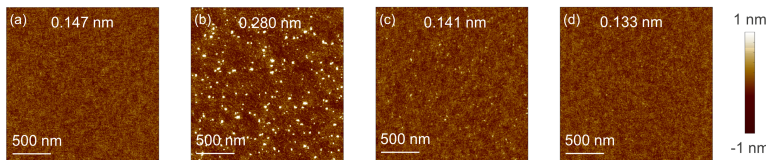


Figure 3.13: AFM images of (a) 1.5 L (b) 2 L (c) 25 L and (d) 70 L STO samples. The numbers shown at the top are the inferred root-mean-square roughness values.

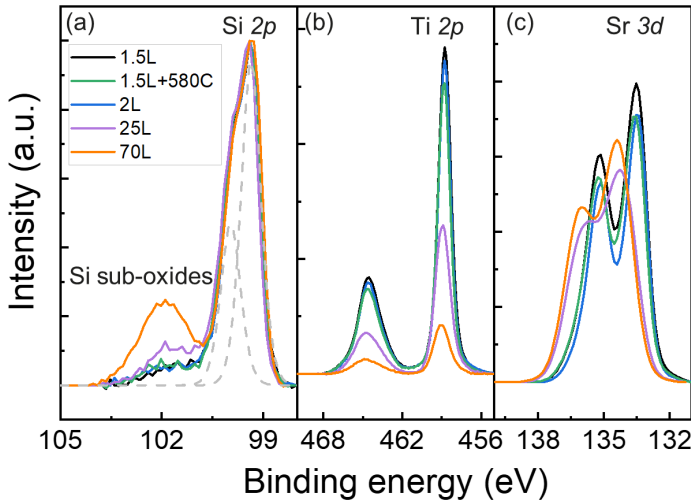


Figure 3.14: XPS results of (a) Si 2p (b) Ti 2p (c) Sr 3d core levels from different exposure amount STO samples. This figure is taken from the previous published work[115].

for the annealed sample are similar with the un-annealed one, suggesting the interface is stable, and the oxygen exposure amount is more crucial for obtaining a good quality interface.

In addition to the interface investigation from Si core levels, we also measure changes in both the Ti and Sr core levels, as shown in Fig. 3.14(b) and (c). For the Ti core level, we observe large intensity decrease when the oxygen exposure amount is increased, which is consistent with the RBS results (Fig.

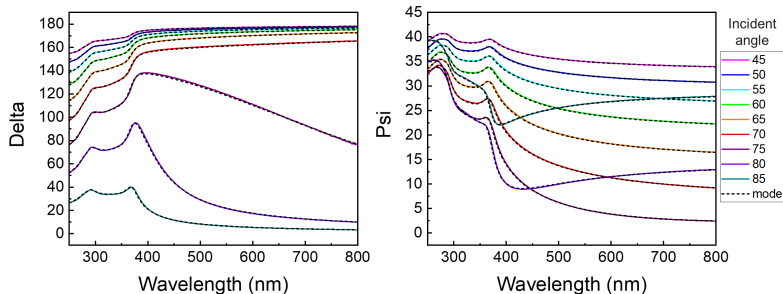


Figure 3.15: Raw SE spectra of the 2 L 4-nm STO sample (solid curves). The dotted lines are produced by the fitting model, which shows great consistency with raw spectra.

3.10). With over-exposure, the stoichiometry of Sr/Ti ratio becomes unstable and forms a very Sr-rich film. For Sr 3d peaks, the peaks are shifted to higher binding energy, which corresponds to SrCO_x bonds[117, 118]. The formation of SrCO_x is due to the easy transformation from SrO to SrCO_x in laboratory ambient, thus the transformation started when the sample has been taken out of the MBE chamber for the subsequent analyses[119]. The higher SrCO_x peak intensity in 70 L sample matches well with the stoichiometry and crystallinity characterization results.

The STO optical indices are measured using J. A. Woollam RC2 spectroscopic ellipsometry (SE) and the subsequent data analysis is carried out by the CompleteEASE software. All the measurements are carried out with varying incident angle from 45° to 85° , and the wavelength is scanned from 200 nm to 2500 nm at each incident angle. The vast amount of data points is then collected and fitted by the software together with the input of surface roughness (obtained from AFM) and layer thickness (obtained from XRR) in order to obtain more accurate optical properties. For the actual SE data analysis, we use oscillator models for the individual films to secure Kramers-Kronig consistency. For our 4-nm STO / Si, all the fitting root-mean-square errors are smaller than 5, which indicates a high consistency between the fitting model and the actual curve. The comparison between the actual curves and the fitting results are shown in Figure 3.15.

After optimizing the fitting, the refractive indices are extracted and plotted in Figure 3.16. All the visible light wavelength is included with the plot from 250 nm to 800 nm. For all our 4-nm STO samples, the refractive index n is found to be smaller than the theoretical value. At 500 nm, the highest measured n

value in our STO samples is 2.23, which is still smaller than the bulk value of 2.48 at the same wavelength[120]. The lowering of n is usually observed in the ultra-thin film, which can be attributed to larger impact from surface and interfaces or due to the smaller film density[121, 122]. As we compare the STO film density from XRR measurement results, all the crystalline STO films have the density larger than 5 g/cm³ (theoretical value of STO density is 5.1 g/cm³), thus the lowering of n is not resulted from the density deviation. To clarify the thickness effect, a 100-nm-thick STO thin film grown by MBE with excellent crystalline quality, showing a STO(002) peak FWHM of 0.2°, has been measured by SE and fitted as well, showing similar n values than the theoretical bulk curve (see Fig. 3.16(a)). The impact of crystallinity is also evidenced from the graph, with thick polycrystalline STO layers larger than 1 μm (from ref.[123]) still showing a smaller reflective index n than our 4-nm-thick epitaxial STO film. In our ultra-thin STO series, it is obvious the crystalline films show larger n than amorphous films, with the 2 L exposure one being the closest to the bulk curve. This result is consistent with RHEED and TEM, suggesting the optimized exposure amount in our system is 2 L. On the contrary, amorphous STO films (exposure amount \geq 25 L) show much smaller n values, situating between the theoretical values of SrO and SrCO₃. With higher exposure amount, the refractive indices are closer to SrCO₃, which confirms the thin film transformation observed by XPS analysis. The additional annealing shows little impact on the n values, indicating that n is mainly governed by the material stoichiometry and crystallinity

The extinction coefficient, or optical loss k , is related to the absorption of the film, which mainly depends on the bandgap and will also be affected by the crystallinity and defect states[129, 130]. In our 4-nm STO samples, the reactive volume is very small especially in the long wavelength range, making the determination of k values rather challenging. The extracted k values for STO layers are plotted in Fig. 3.16(b). As indicated, the k values below the 0.01 level are not really measurable and are extrapolated based on the oscillators with higher extinction coefficients in the smaller wavelength range. These oscillators are used to estimate the bandgap as well, which is obtained by calculating and plotting the absorption coefficient α versus incident energy, as shown in Figure 3.17. In the crystalline STO samples, the 1.5 L and 2 L STO films show a similar extinction coefficient, with the extracted bandgap matching the theoretical value of 3.2 eV[131]. With additional annealing after STO growth, the extinction coefficient is further reduced with sharper slope, as shown in Fig. 3.16(b). The reduction in extinction coefficient is important for the VH application as the waveguide loss is supposed to be reduced. For the amorphous 25 L sample, the k value shows a blue shift with an extracted bandgap of around 4 eV, which is close to the theoretical value of 4.4 eV for SrCO₃[124, 132]. This shift is consistent with the XPS results and further validates the change in film

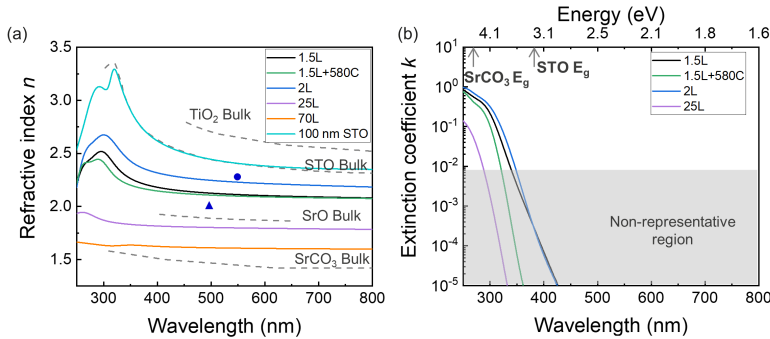


Figure 3.16: (a) refractive index n and (b) extinction coefficient k of STO extracted by SE. The reference values (dashed curves) are taken from the literature. The circle and triangle points represent the polycrystalline and amorphous STO references, respectively. The refractive index bulk reference values are taken from Refs.[120, 123, 124, 125, 126, 127, 128]. The grey region in (b) is not representative for the actual values obtained from the STO films. This figure is taken from the previous published work[115].

stoichiometry when we increase the oxygen exposure amount.

Based on the XPS and RBS data, we calculate the sticking coefficient of Sr and Ti from the total amount of each species inside the STO films. As shown in Figure 3.18(a), the sticking coefficient of both Sr and Ti decreases as the oxygen exposure amount increases, with Ti being much more affected. To grow STO epitaxially on Si with good crystallinity, the ratio of Sr/Ti needs to be as close to unity as possible, thus the precise control of Sr and Ti fluxes is required. In comparison with other perovskite oxides with volatile species such as Bi, Ru and Sn, the growth behavior is totally different for these elements[134, 135, 136]. The sticking coefficient of these elements is very small due to the large vapor pressure under high-vacuum environment, thus it requires different manipulations including over-pressure of the species and high oxygen pressure in the chamber to consolidate the oxide growth at raised substrate temperature[137, 138]. These oxides such as SrRuO₃ and BiFeO₃ increase the sticking coefficient as the oxygen increases, showing a totally different growth pattern compared to STO.

The variation in slopes of Sr and Ti sticking coefficient as a function of the oxygen exposure amount can be linked to the formation energy differences ΔG in TiO₂ and SrO, plotted in Fig. 3.18(b)[139, 140]. Compared with SrO, the formation energy of TiO₂ is lower, suggesting a much easier oxidation for Ti

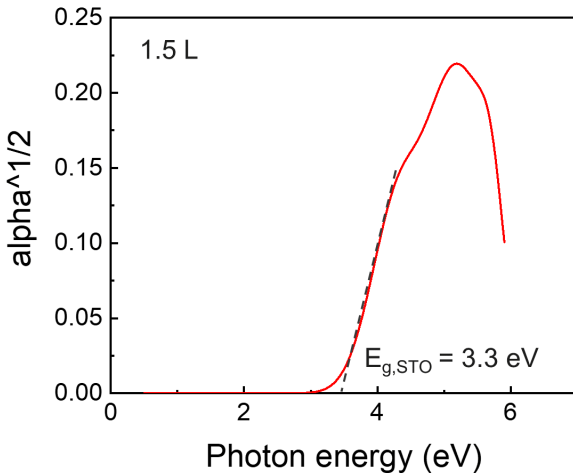


Figure 3.17: STO bandgap extraction using a plot of the absorption coefficient $\sqrt{\alpha}$ v.s. incident photon energy. The absorption coefficient α is calculated from the extinction coefficient k with the equation $\alpha = 4\pi k/\lambda$ [133]. The extrapolated bandgap value corresponds well with the theoretical value.

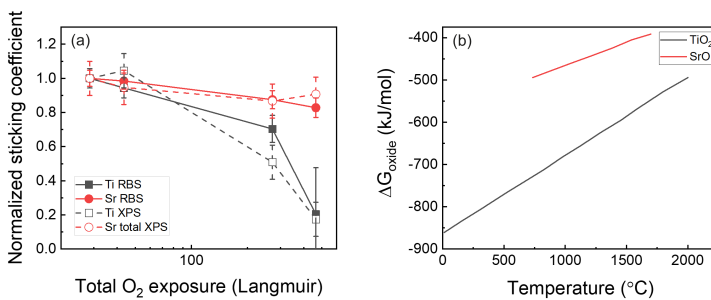


Figure 3.18: (a) Variation of the sticking coefficient with oxygen exposure amount. (b) Formation energy comparison of TiO₂ and SrO taken from references [139] and [140]. This figure is taken from the previous published work[115].

under the same environment as Sr. Thus, when excess oxygen is present inside the MBE chamber, the Ti is more easily transformed to TiO_2 , resulting in the lowering of the sticking coefficient and less participation in the STO growth.

The oxygen exposure amount is crucial for the STO growth on Si, which affects both crystallinity and stoichiometry. Direct epitaxial STO can be further realized with optimized substrate temperature, resulting in a clean and coherent interface with Si.

3.3 Thick Oxide Growth and Source Oxidation Effect

Even though growing thick STO is out of scope for this thesis and the video holography application, the related growth and characterizations of thick STO layers are reported in the following section and some very important findings are highlighted. Moreover, thick STO films larger than 100 nm integrated on silicon substrates are proposed to improve the quality of epitaxial diamond (together with the usage of an iridium buffer layer grown on STO), making this study for MBE-grown thick oxides essential[141, 142].

3.3.1 Stoichiometry Evolution of Thick STO

Due to the thermal expansion coefficient differences between STO, BTO and Si, different thicknesses of the STO buffer layer is reported to affect the final strain distribution in a BTO layer grown on top, with thicker STO favorizing the c-BTO growth[69]. However, when growing thicker STO layer with thickness larger than 50 nm, often stoichiometry instabilities are observed during the epitaxy. As shown in Figure 3.19, a STO reconstruction change is observed by RHEED during the thick STO growth. As the deposition time increases, the STO film changes from slightly Sr-rich to slightly Ti-rich with additional lines along the $[100]_{\text{STO}}$ azimuthal direction being observed and small spots appearing in the $[110]_{\text{STO}}$ azimuthal direction after long time deposition.

The stoichiometry change inside the thick STO film is investigated by RBS analysis, and the results are shown in Figure 3.20. In the figure, data points are plotted as black curves, and the red curves are generated from simulation. For Ti peak, the flat top suggests that the Ti amount is stable over the whole STO film. On the contrary, the Sr peak shows an obvious slope, i.e., a slow decrease from the bottom toward the top surface, indicating the that Sr concentration in the STO layer is progressively reduced with thickness.

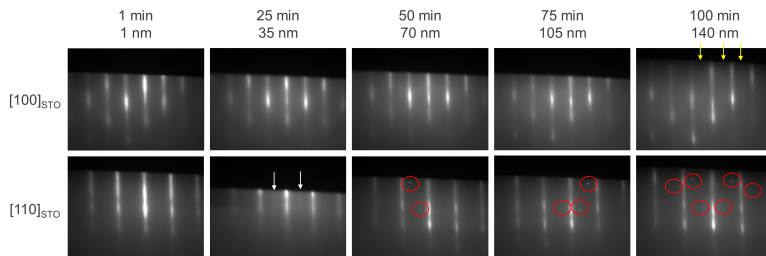


Figure 3.19: RHEED images taken during STO / Si epitaxy. The arrows indicate additional lines in between the main diffraction streaks with white arrows corresponding to Sr-rich and yellow ones corresponding to Ti-rich. The circles include additional spots which correspond to a Ti-rich phase.

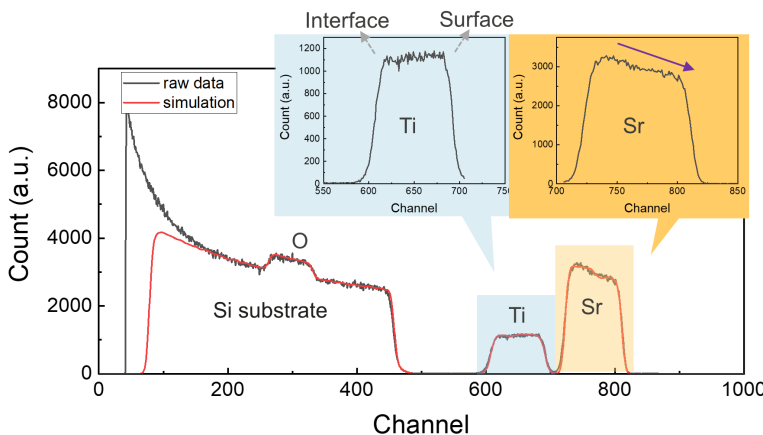


Figure 3.20: RBS analysis of thick STO. The black curves and red curves represent measured data points and simulations, respectively. The Sr signal shows a decrease from the STO / Si interface toward the surface while the Ti signal remains flat.

3.3.2 Source Oxidation Effect

The currently observed compositional instability for thick layers of both the STO and BTO grown using plasma assisted MBE causes serious stoichiometry problem and degrades the perovskite quality. The decrease of Sr and Ba was also observed by other groups who also highlighted the source oxidation problem during oxide growth[143, 144]. In our MBE oxide system, the Sr and Ba species are produced by effusion cells, and the cell temperature is determined as a function of deposition rate as measured by QCM prior to the growth. In the case of Ti, the atomic flux is generated by an e-beam evaporator, and the Ti partial pressure is controlled by XBS with feedback loop on the e-gun power supply ensuring a much stable Ti supply compared to Sr and Ba.

In this section, we study the behavior of the Sr source as a function of the temperature of the cell as well as its environment, using an in-situ XBS installed in front of the Sr atomic beam (and without feedback loop system on the effusion cell power supply). The Sr pressure under different gas ambients (O_2 , N_2 , and UHV) has been studied, with the results presented in Figure 3.21. When executed in UHV, the chamber pressure is around 5×10^{-9} Torr (without any gas introduction), while for the N_2 and O_2 condition, the chamber pressure is around 5×10^{-7} Torr. As to the Sr partial pressure under N_2 ambient and in vacuum, it is seen from Fig. 3.21 that the impact from the environment is negligible. On the other hand, the Sr partial pressure decreases immediately after the shutter is opened under oxygen ambient, suggesting the source starts to oxidize. After the shutter is closed, the pressure slowly restores to the initial value, which means the SrO_x is gradually desorbed from the source surface in UHV.

The oxidation effect has further been investigated for different oxygen conditions as a function of Sr evaporation temperatures, and the results are plotted in Figure 3.22. As shown in Fig. 3.22(a), both molecular and atomic oxygen oxidize the Sr, with, as expected, faster decrease under atomic oxygen due to the higher reactivity of the atomic oxygen species. However, the stable pressure is very similar regardless the form of oxygen atoms, with indication on that the oxidation process becomes thermodynamically stable after a reaction time longer than ~ 15 min. We then have recorded the stable pressure differences for different Sr cell temperatures, and the results are plotted in Fig. 3.22(b). For Sr cell temperatures below 450 °C, the differences between vacuum and oxygen ambient are large. However, as the Sr cell temperature increases, the gap becomes smaller. For Sr cell temperature larger than 500 °C, the differences under various ambient conditions are no longer obvious. This change indicates that above a certain transition temperature, the oxidation effect is largely reduced, and the difference in partial pressure between different ambients

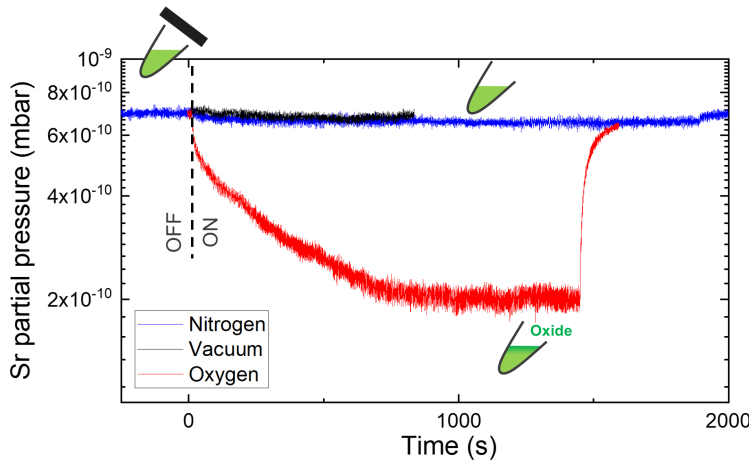


Figure 3.21: Sr partial pressure recorded before and after opening the shutter to different gas ambients: nitrogen, vacuum, and oxygen. “On” means time of opening the shutter.

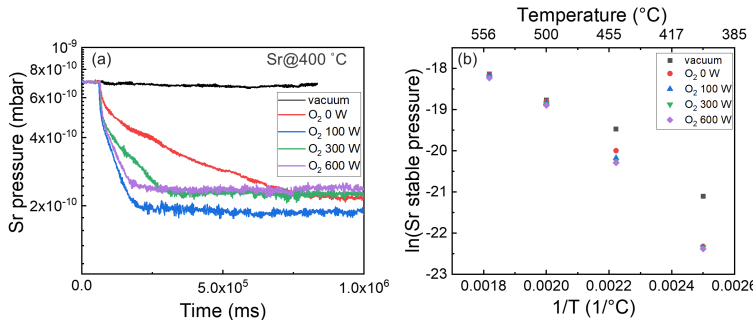


Figure 3.22: (a) Sr partial pressure behavior under oxygen ambient for different oxygen forms and plasma power. (b) Sr partial pressure comparison using different Sr temperatures. Oxygen pressure is $\sim 5 \times 10^{-7}$ Torr.

becomes negligible.

The Sr oxidation effect is further studied for different oxygen pressures. The oxygen pressure has been varied with different oxygen flows during Sr oxidation experiments, and the results are plotted in Figure 3.23. With increasing oxygen

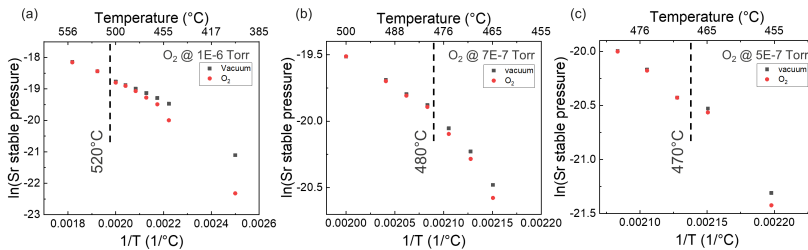


Figure 3.23: Sr stable partial pressure comparison for different Sr cell temperatures under varied oxygen pressure of (a) 1×10^{-6} Torr (b) 7×10^{-7} Torr and (c) 5×10^{-7} Torr. The vertical dashed lines indicate roughly the value of the transition temperature.

pressure, the transition temperature increases, indicating the Sr evaporation fluxes need to be larger in order to prevent oxidation as the reaction is accelerated with more oxygen.

The transition temperature suggests the source oxidation effect can be largely suppressed above a certain transition temperature, which is really important to determine thick oxides growth. To examine the suppression of the source oxidation effect, thick STO films with a thickness ~ 100 nm is grown with source temperature higher than the transition temperature reported in Fig. 3.23. The results of RHEED and RBS analysis results of these films are shown in Figure 3.24. Compared with the lower Sr temperature STO, the Fig. 3.24(a) images are more stable in terms of composition, with only a slightly Ti-rich phase appearing at the end of the growth. Also in the RBS profile, the Sr peak shows a flatter slope with no obvious degradation as the growth progresses. Both results validate our Sr oxidation analysis and provide a possible solution for the source oxidation effect.

However, higher Sr cell temperature results in higher Sr flux, thus the growth rate is also increased. The XRD comparison between high and low growth rate STO is shown in Figure 3.25. This shows that high growth rates results in larger XRD FWHM for both symmetric and asymmetric scans. For the epitaxial thin films, small mis-orientation crystallites can result in mosaic films, which broadens the XRD peaks from both symmetric and asymmetric scans. The symmetric ω -scan is linked to the film tilt mosaicity, while the asymmetric φ -scan is related to the twisted crystallites which are slightly rotated around the out-of-plane axis[145]. With larger FWHM of both STO(002) and STO(101) peaks, the defect density is expected to be higher for the larger growth rate.

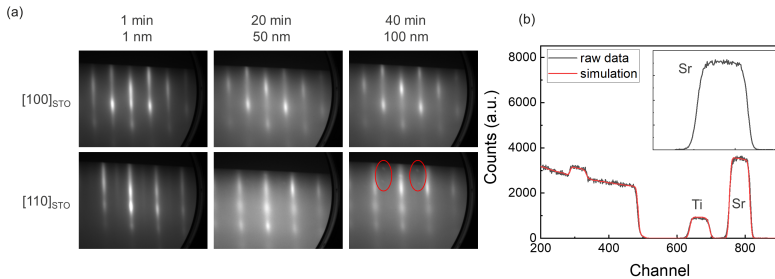


Figure 3.24: (a) RHEED evolution and (b) RBS analysis results of thick STO (~ 100 nm) with Sr cell temperature higher than the transition temperature.

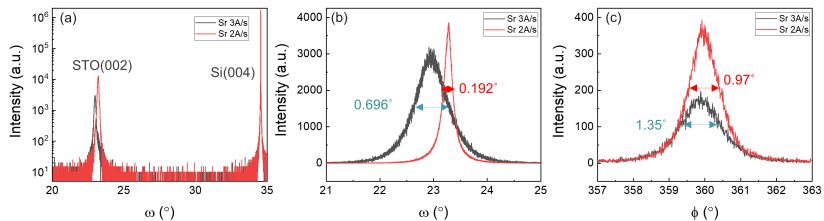


Figure 3.25: Data taken on STO with different growth rate. (a) XRD symmetric ω - 2θ scan (b) STO(002) ω -scan (c) STO(101) ϕ -scan. The red curves represent low growth rate (i.e. lower Sr temperature) while the black ones stem from high STO growth rate (i.e. higher Sr temperature).

The lattice parameter of the low-growth-rate STO is ~ 3.90 Å for both in-plane and out-of-plane orientation, suggesting this film is relaxed to the bulk cubic structure. On the other hand, the high-growth-rate STO shows slightly larger lattice parameter of ~ 3.94 Å for the out-of-plane orientation. Considering an in-plane lattice parameter of ~ 3.92 Å, this film is still slightly strained in compression for a 100-nm growth. However, larger deviation of lattice parameters from the bulk STO could also be linked to the degradation of crystallinity.

Metallic source oxidation without feedback loop control causes stoichiometry instability during thick oxide growth. A Higher source temperature can suppress this effect, but then results in degraded crystallinity.

3.4 Conclusion

The direct epitaxy of STO / Si has been demonstrated for optimized temperature and oxygen exposure amount. Oxygen exposure prior to the STO growth proves to be crucial for obtaining high quality epitaxial STO, including sharp interface, stable stoichiometry, and good crystallinity. On the contrary, over-exposure of oxygen results in not only a thick interfacial layer but also a shift in the stoichiometry which leads to large degradation.

When growing thick oxides using MBE, the metal sources (from effusion cells in our system) are oxidized by oxygen ambient in the chamber, and the atomic fluxes are slowly decreased if not applied a feedback loop control system on the power supply of the source. This decrease results in stoichiometry instability during the growth process, which is probed by RHEED and confirmed by RBS analysis. The Sr oxidation is further studied for different ambient gases, pressures and temperatures. The results suggest that the oxidation immediately starts in the presence of oxygen regardless the oxygen form; moreover, the oxidation effect could be minimized when the source temperature is above the “transition” temperature. When growing STO at higher growth rate, with sources above the “transition” temperature, less compositional change is observed as evidenced by RHEED and RBS analyses. However, the final film quality exhibits larger FWHM of XRD peaks, meaning this layer is more defective due to the too high growth rate of the perovskite layer.

Chapter 4

MBE-grown BTO on Si with STO Buffer Layer

MBE is used to grow BTO epitaxial films because of its ability to control the growth at atomic level. However, as demonstrated in the previous chapter, source oxidation during thick oxide growth is also expected for MBE-grown BTO and will need to be taken in consideration for obtaining reliable epitaxy. Thus, in this chapter, different approaches to counteract the source oxidation effect will be carried out.

Different from the STO / Si epitaxy growth, which requires precise control in temperature and pressure, the BTO is grown on the STO layer with the already formed crystalline perovskite structure underneath. Thus, a higher substrate temperature of 580 °C and larger oxygen pressure of $\sim 1 \times 10^{-6}$ Torr is used. In addition, an oxygen plasma with maximum power of 600 W is applied during the growth in order to reduce oxygen vacancies and enhance dielectric properties. Similar as carried out for the STO growth, the Ba and Ti atomic fluxes are calibrated by means of QCM before the growth, where Ba is emitted from an effusion cell and Ti is generated by an e-beam evaporator with feedback loop control.

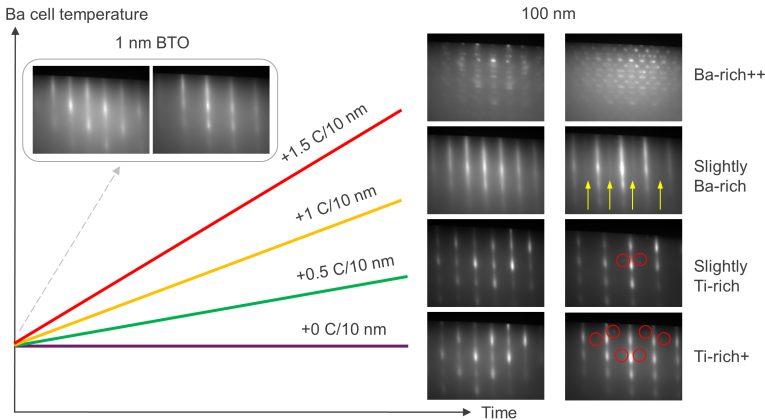


Figure 4.1: BTO RHEED evolution with different Ba temperature gradient settings.

4.1 Ba Temperature Compensation for Source Oxidation Effect

As described in the previous chapter, the oxidation of metallic sources without feedback loop will cause stoichiometry instability for thick oxide growth. For the BTO in VH application, the targeted thickness is ~ 100 nm, thus the decrease of Ba after long deposition time is expected to happen. To overcome the source oxidation effect, a direct compensation to Ba source is proposed. In this approach, the Ba effusion cell temperature is continuously increased to compensate flux loss during the growth. As shown in Figure 4.1, the 100-nm BTO layers are grown with the same initial Ba and Ti fluxes. During the growth, four different gradient settings are used, starting from 0 $^{\circ}\text{C}$ to 1.5 $^{\circ}\text{C}$ per 10 nm growth, and clear differences in the final RHEED patterns are observed. For the BTO without any flux compensation, the final RHEED patterns show typical additional Ti-rich spots. As the gradient increases, the Ti-rich spots start to disappear, reaching almost stoichiometric with only slightly Ba-rich reconstruction using 1 $^{\circ}\text{C}/10$ nm gradient setting. Furthermore, when the gradient is too large, with 1.5 $^{\circ}\text{C}/10$ nm, the final BTO layer becomes very Ba rich as the streaks disappear and Ba reconstruction pattern appears. The direct compensation on Ba temperature shows that with optimized gradient, the stoichiometric BTO can be maintained during the epitaxy process.

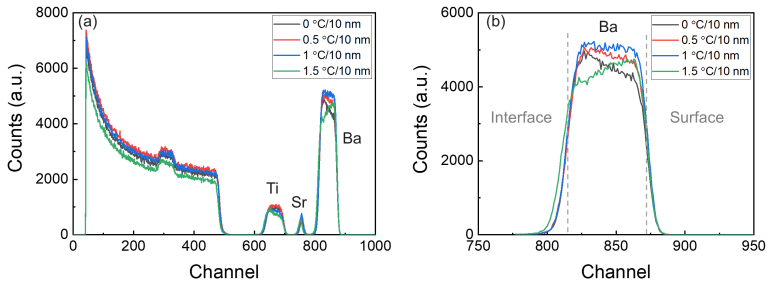


Figure 4.2: RBS analysis results of BTO with different Ba gradient settings.
(a) RBS peaks with different elements. (b) Ba peak slope comparison.

The RBS analysis results of different gradient BTO are shown in Figure 4.2. Since the thickness of STO buffer is only of ~ 4 nm, the signal of Sr is relatively small and narrow without clear differences between the 4 samples. On the contrary, for the thick BTO layer, the Ba signal shows obvious slope differences, which is in good agreement with the RHEED observations. As demonstrated in Figure 4.2(b), the Ba intensity decreases from interface to sample surface with gradient smaller than $0.5\text{ }^{\circ}\text{C}/10\text{ nm}$. However, with over-compensation, the gradient of $1.5\text{ }^{\circ}\text{C}/10\text{ nm}$ shows reverse slope with higher Ba signal intensity close to the surface. These results confirm the stoichiometry changes initially observed by RHEED pattern evolution and show that with appropriate setting of $\sim 1\text{ }^{\circ}\text{C}/10\text{ nm}$, the Ba signal intensity is stable during the full growth.

The XRD characterization results for these 100-nm BTO samples are shown in Figure 4.3 and Figure 4.4. The extracted out-of-plane lattice parameters are between 3.99 \AA and 4.02 \AA , with the $1.5\text{ }^{\circ}\text{C}/10\text{ nm}$ showing the smallest out-of-plane lattice parameter and the $0\text{ }^{\circ}\text{C}/10\text{ nm}$ the largest, except the $1\text{ }^{\circ}\text{C}/10\text{ nm}$ BTO also showing larger value. These variations in lattice parameter are linked to the different degree of relaxation in the BTO / STO / Si heterostructure. Due to lattice parameter and thermal expansion coefficient differences, the BTO epitaxy on Si using thin STO as buffer layer results in compressive strain thus tends to favor the elongation along the c-axis[69, 146]. Naturally, the BTO with different crystal quality is expected to impact the strain relaxation. The crystallinity analysis results are shown in Fig. 4.3(b) and (c), and the FWHM values are summarized in Fig. 4.4, which confirms the quality is largely impacted by stoichiometry variation in the layer. The BTO layer with stable Ba flux shows the smallest FWHM of both BTO(002) and BTO(101) peaks, while other samples with stoichiometry variation along the thickness all show

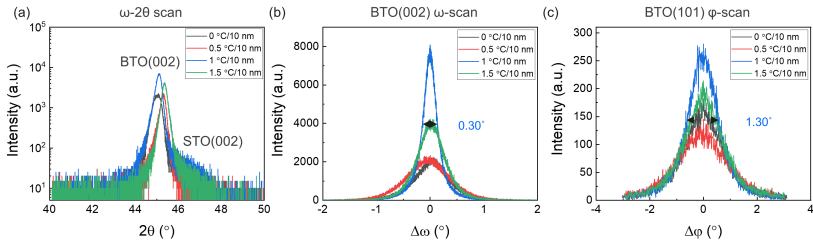


Figure 4.3: (a) symmetric ω - 2θ scan around BTO(002) peak (b) BTO(002) ω -scan and (c) BTO(101) φ -scan of BTO with different Ba temperature gradients.

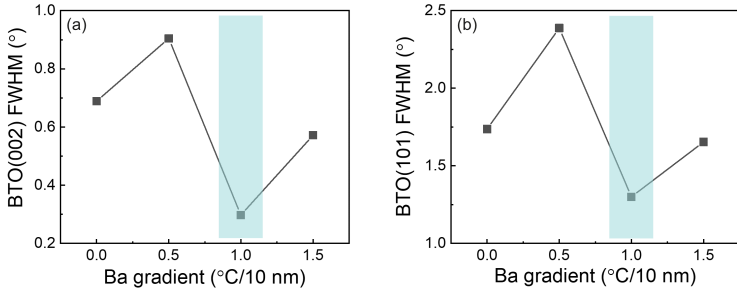
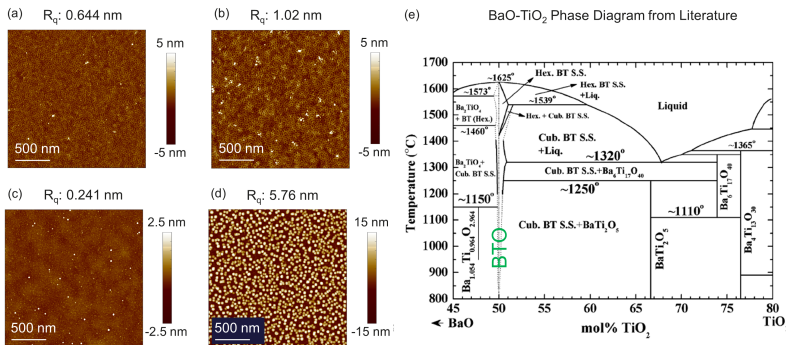


Figure 4.4: Crystallinity comparison of 100-nm BTO with different Ba temperature gradients. (a) FWHM values from BTO(002) ω -scans. (b) FWHM values from BTO(101) φ -scans. With the BTO composition closest to the stoichiometric, the FWHM values are the smallest.

obvious increase in the FWHM values. However, this result could only partially explain the larger c-axis lattice parameter in the BTO with 1 °C/10 nm since the defectivity is rather small. The other trend in the c-axis distribution for the relaxed samples shows deviations from the crystal quality, suggesting there are other factors involved such as different phases formation from stoichiometry instability which impacts the lattice parameters[147].

The surface roughness is also investigated and presented in Figure 4.5. It is obvious that the stable Ba/Ti ratio results in the smoothest surface. Based on the phase diagram of BaO and TiO₂, only the Ba/Ti ratio close to 1 would result in BTO formation. Otherwise, additional phases such as BaTi₂O₅ or Ba₂TiO₄ could easily be formed[147]. In our BTO films, these phases from inappropriate



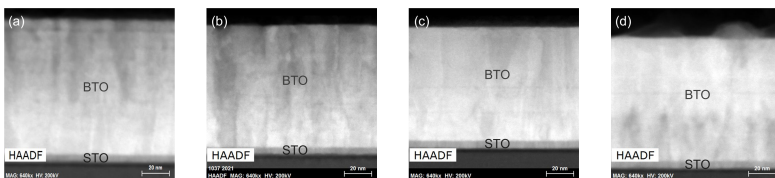


Figure 4.6: STEM HAADF images of BTO with different gradients of (a) 0 °C/10 nm (b) 0.5 °C/10 nm (c) 1 °C/10 nm and (d) 1.5 °C/10 nm.

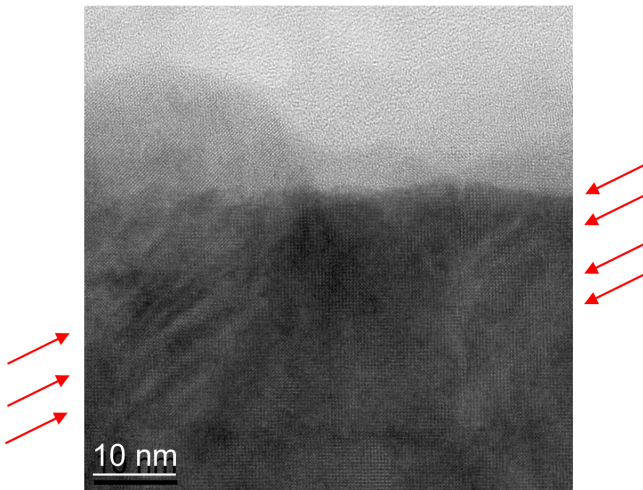


Figure 4.7: Dislocations around BTO islands by HRTEM. The red arrows are a rough indication for the dislocation positions.

relaxed lattice parameter. In the in-plane direction, the relaxation results in larger lattice parameter, which is more obvious in the 1.5 °C/10 nm sample as shown in Fig. 4.8(h). For the 1 °C/10 nm BTO in Fig. 4.8(g), the in-plane lattice parameter is small with good uniformity, confirming the film is surprisingly still strained in c-orientation despite the large thickness of the BTO layer. On the other hand, the BTO film with 1.5 °C/10 nm gradient not only has larger contrast by HAADF, but also presents islands capturing defects around. These additional defects all accelerate the strain relaxation of the BTO lattice.

The local BTO lattice parameter can be quantitatively compared by using the

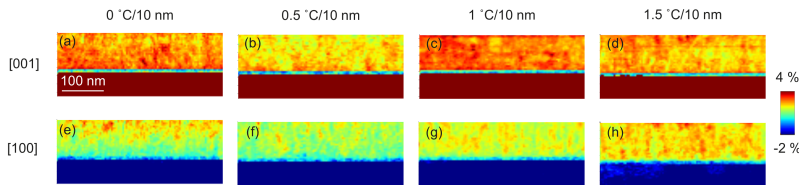


Figure 4.8: Strain mapping by NBD analysis of 100-nm BTO with different Ba gradients in (a)-(d) out-of-plane and (e)-(h) in-plane direction.

STO as reference from the NBD analysis results. The lattice mismatch profile relative to the STO underneath is plotted in Figure 4.9, which confirms the sample with 1 °C/10 nm is indeed strained with larger out-of-plane lattice parameter while the 1.5 °C/10 nm sample is fully relaxed with the in-plane and out-of-plane lattice parameters almost equal. The Ti-rich samples (no gradient and 0.5 °C/10 nm gradient) show larger out-of-plane lattice parameter close to STO interface, suggesting the initial lattices are strained and gradually relax with the increased thickness of the thin film. This strain relaxation is similar with the results reported by Dubourdieu et al., who demonstrated the BTO film was highly strained in c-orientation for the first ~8 nm, then started to relax as the thickness increased[66]. On the other hand, our BTO film with 1 °C/10 nm compensation shows the strain is still maintained for 100-nm thickness, which can be resulted from the almost perfect stoichiometry. As a result, the stoichiometry control affects not only the crystal quality but also the strain distribution, and thus is proved to be the most critical parameter to oversee in the MBE epitaxial process of perovskite oxides.

4.2 BaTiO₃ Deposited Using Different Growth Rates

The Ba gradient shows to be a promising technique for controlling the stoichiometry in the MBE oxide chamber. However, we still investigate the Ba oxidation effect for different source temperatures, trying to find the transition temperature similarly to the strontium case described in chapter 3. As illustrated in Figure 4.10, the Ba source also shows less difference in the stable pressure under different ambient conditions for temperatures higher than ~580 °C. During the experiment, the MBE chamber environment is set with the same oxygen pressure and plasma power as applied for the BTO epitaxy growth.

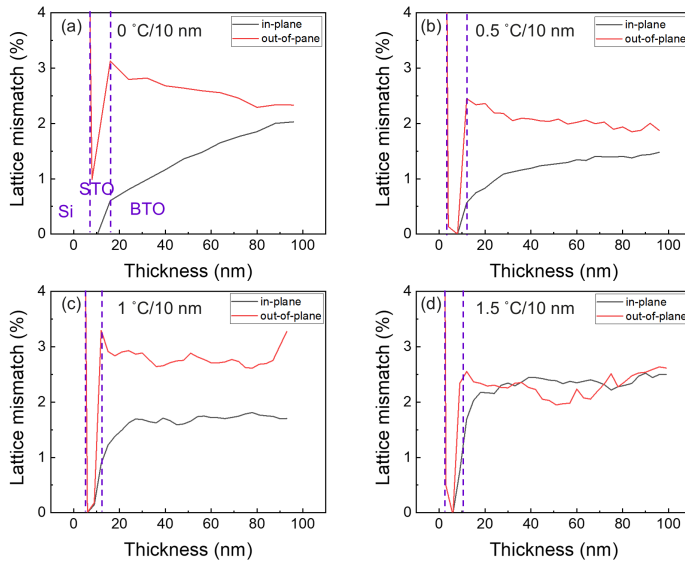


Figure 4.9: BTO NBD profiles in in-plane and out-of-plane directions with (a) 0 °C/10 nm (b) 0.5 °C/10 nm (c) 1 °C/10 nm and (d) 1.5 °C/10 nm gradient. The STO layer is used as lattice reference.

The BTO growth without gradient compensation is tested for the Ba cell temperature higher than 600 °C, but Ba loss is still observed by RHEED. The higher temperature shows less degradation, but in order to maintain the Ba flux stable, the temperature gradient is still applied even for source temperature higher than the transition temperature. Based on this, three BTO films with different Ba effusion cell temperatures higher than 580 °C are grown in combination with the Ba gradient; the observed RHEED images after 100-nm BTO deposition are shown in Figure 4.11(a). For high Ba source temperature and gradient compensation, no additional spots are observed on the RHEED images.

These 3 different BTO layers with varied growth rate are further analyzed by XRD, and the ω -scan results are shown in Figure 4.11(b). The FWHM values of the BTO(002) peak become larger with increasing of Ba cell temperature, i.e. growth rate, suggesting that more defective BTO layers are formed. The XRD results are used to estimate the screw dislocation density in the BTO thin films by using symmetric ω -scans, with the equation[148]:

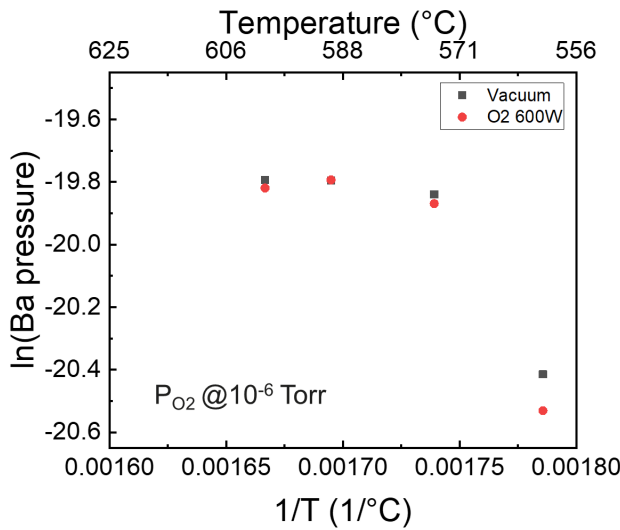


Figure 4.10: Ba stable pressure comparison for different Ba cell temperatures under an oxygen pressure of 1×10^{-6} Torr.

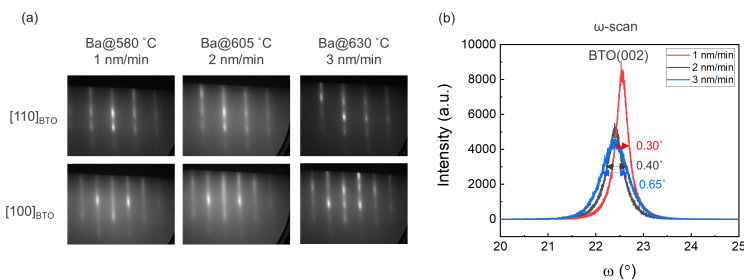


Figure 4.11: (a) RHEED with different Ba source temperature after 100-nm growth. (b) BTO(002) ω -scan of BTO for different growth rates.

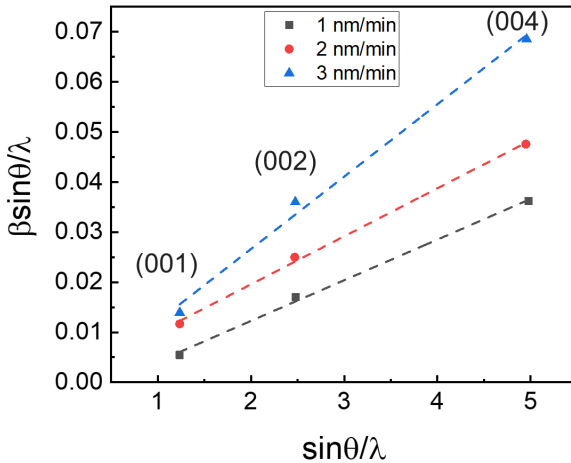


Figure 4.12: FWHM values of ω -scan from different BTO symmetric peaks plotted versus incident angle $\sin \theta / \lambda$. The slope corresponds to the tilt angle.

$$N_s = \frac{\alpha_\Omega^2}{4.35 b_c^2} \quad (4.1)$$

where α_Ω is the tilt angle and b_c the Burgers vector magnitude. To obtain the tilt angle, the Williamson-Hall plot method is applied, which can extract the tilt angle and the lateral crystallite size by using the FWHM values from ω -scans[149, 150]. The tilt angle extraction is plotted as in Figure 4.12, in which the extrapolation to the x-axis is linked to the lateral grain size while the slope is related to the tilt angle. For our BTO, 3 symmetric peaks are chosen to do the ω -scan, but without using BTO(003) due to its peak position being too close to the Si(004) reflection. The results show that with increased growth rate, the slope becomes steeper. From the BTO film with the lowest growth rate of 1 nm/min, the extracted slope is 0.0081 rad, which results in $\sim 1 \times 10^{10}$ (cm $^{-2}$) screw dislocation density.

The screw dislocation densities of BTO films for different growth parameters are summarized in Table 4.1. When the growth rate is increased from 1 nm/min to 3 nm/min, the screw dislocation density is also increased to roughly three times. As for the stoichiometry variation, any deviation from stoichiometric

Table 4.1: Summary of a defect density of BTO films with different growth parameters.

BTO parameter	Tilt angle (rad)	N _s (cm ⁻²)
1 nm/min	0.0081	9.9×10 ⁹
2 nm/min	0.0096	1.4×10 ¹⁰
3 nm/min	0.0145	3.2×10 ¹⁰
0 °C/10 nm	0.0161	3.9×10 ¹⁰
0.5 °C/10 nm	0.0148	3.3×10 ¹⁰
1 °C/10 nm	0.0098	1.4×10 ¹⁰
1.5 °C/10 nm	0.0131	2.6×10 ¹⁰

composition will result in obvious increase in defect density, thus is one of the most crucial parameters of obtaining high-quality epitaxial BTO films by MBE.

The degradation of film quality obtained by using higher growth rate is also reflected on the surface roughness. As shown in Figure 4.13, where the surface roughness is measured by AFM, the higher growth rate shows a rougher surface. The BTO with 2 nm/min shows slightly larger roughness than the 1 nm/min one, but is still relatively flat without showing islands nor pinholes. On the other hand, when the growth rate becomes too high, clusters of diameter ~100 nm start to appear on the BTO surface. In addition to the large clusters, smaller grains are also observed with diameter ~30 nm, suggesting the film is grown in a 3D island configuration. Combining results from XRD and AFM, the BTO films with growth rate smaller than 2 nm/min are grown in 2D mode; however, more dislocations will be generated with higher growth rate. For the BTO with growth rate larger than 3 nm/min, the growth mode evolves towards 3D growth, with grains and clusters formed which further degrade the final film quality.

4.3 BaTiO₃ Optical and EO Properties Comparison

As shown in Fig. 4.14(a), the BTO films with different growth rates and gradients shows obvious deviation of the refractive index n . Among all the samples, the low growth rate with proper gradient setting presents almost identical n values compared with the bulk reference[151, 152]. However, the high growth rates BTO films show slightly lower n in the visible light range, while the non-optimal gradients BTO films show even larger deviations. In combination with the results from STO in Fig. 3.16, the refractive index n

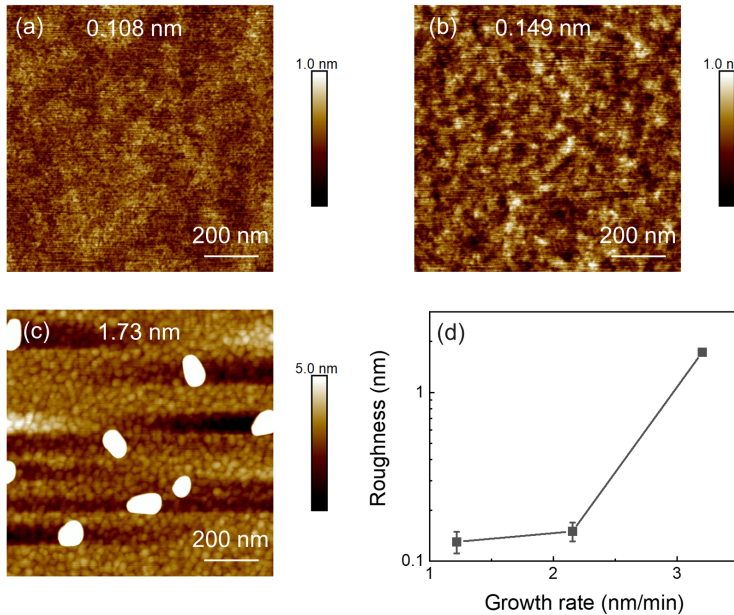


Figure 4.13: 100-nm BTO surface roughness by AFM for a growth rate of (a) 1 nm/min (b) 2 nm/min and (c) 3 nm/min. The numbers shown are the root-mean-square roughness, with the higher the growth rate, the rougher the surface as in (d).

proves to be largely impacted by stoichiometry, while the film quality shows less obvious effect.

Other than refractive index n , another important optical index of extinction coefficient k is also analyzed, and the comparison is shown in Fig. 4.14(b). Compared with the ultra-thin STO layer in chapter 3, all extinction coefficient values are not zero in the longer wavelength range for these 100-nm BTO films. This increase in absorption suggests the presence of additional oscillators in the infrared (IR) range, which could be linked to oxygen vacancies or defects generated due to non-stoichiometric composition and worse crystallinity[72]. As a result, the BTO with Ba gradient of $1\text{ }^{\circ}\text{C}/10\text{ nm}$ shows the lowest absorption in the visible light range. Even with the increased absorption in IR, we can still extract the BTO bandgap using the extrapolation from the oscillators in the visible light range. As shown in Figure 4.15, the bandgap is extracted by extrapolating the absorption coefficient with the intercept of x-axis. As

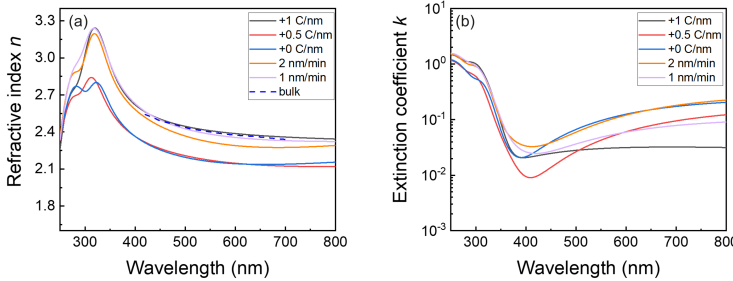


Figure 4.14: (a) refractive index n and (b) extinction coefficient k of 100-nm BTO with different growth parameters. The bulk values are adopted from Refs.[151] and [152].

indicated in Fig. 4.15, the increase in absorption in IR shows little impact on the BTO bandgap value, which are in both cases ~ 3.3 eV despite slightly different profiles. This further validates that the absorption in IR is preferentially related to defects generated during the process. Compared with the absorption curve from literature, the bandgap is slightly larger than the bulk, which could be due to the presence of strain in the thin films compared with bulk BTO. With the strain, the bandgap could be slightly modified, and this blue shift could be explained by the raised conduction band from slight displacement of titanium cations toward the oxygen anions in thin films[153, 154].

The EO effect is mainly dominated by Pockels effect for BTO. In this work, the Pockels measurement was outsourced with the setup similar to and referenced from the publication of S. Abel[48]. In the measurement, a transmission laser beam with wavelength of 1550 nm is used. The electrodes are deposited on BTO sample surface with a gap $\sim 7 \mu\text{m}$. In order to obtain the largest response of Pockels effect, the electrodes are rotated 45° on BTO surface and high temperature of $\sim 600^\circ\text{C}$ annealing under O₂ ambient is performed to reduce the leakage current[48, 64, 67]. When the laser beam passes through the sample, with DC voltage magnitude larger than 30 V and a small AC voltage of 1 V applied on the electrodes, the BTO polarization is changed which induces the refractive index change. By measuring the change of beam ellipticity, the BTO Pockels coefficient could be calculated.

The Pockels coefficient of BTO samples with different gradients is shown in the 4.16(a), which presents the opposite trend as the BTO(002) FWHM by XRD ω -scan as in Fig. 4.4. This trend, however, shows obvious deviation when

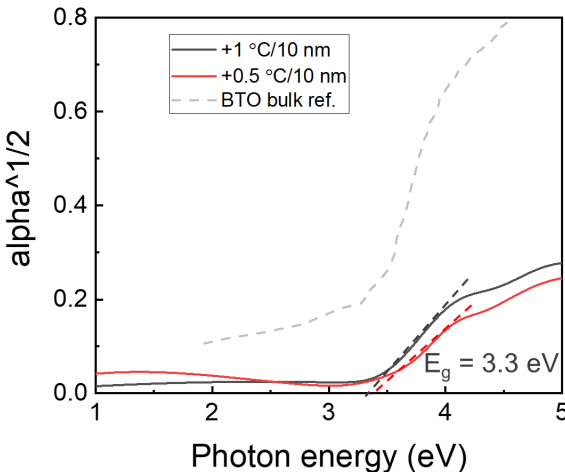


Figure 4.15: Absorption coefficient as a function of photon energy for BTO bandgap extraction. The extracted bandgap is very similar for BTO with different gradient settings despite different amount of absorption in IR. The bulk absorption is re-plotted from Ref.[153].

comparing with the BTO domain orientation from the NBD results. Since the applied electric field is stronger in the in-plane direction, the a-oriented BTO is expected to have higher Pockels coefficient. However, the sample with the highest Pockels coefficient is in final the strained one along the c-orientation, while the fully relaxed sample only shows to have the 2nd highest value. This result indicates that even though the orientation of BTO is important, the film crystallinity can also largely affect the Pockels coefficient. As illustrated in Fig. 4.16(b), the Pockels coefficient shows high correlation with the defect density. Thus, in order to obtain BTO films with high Pockels coefficient, not only the domain orientation control but also the film crystallinity optimization is mandatory.

4.4 Conclusion

The BTO layer grown by MBE suffers from the source oxidation effect, which results in a stoichiometry instability and degrades the film crystallinity. In order

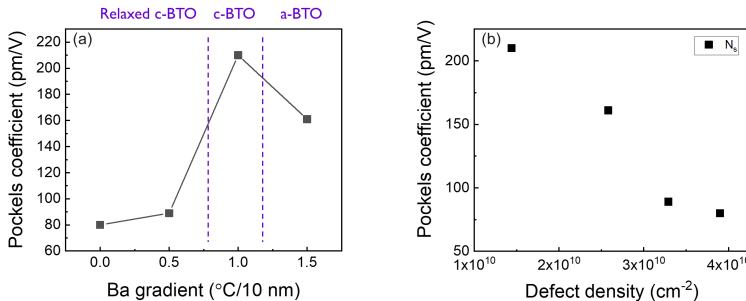


Figure 4.16: (a) Pockels coefficient of BTO with different Ba gradient settings. (b) Pockels coefficient shows reverse trend with the defect density.

to compensate the Ba concentration loss, a temperature gradient is applied on the Ba source, which effectively influences the film stoichiometry. With the appropriate settings, the Ba/Ti ratio in a thick BTO film can be controlled, leading to optimal thin film quality with (002) FWHM $\sim 0.3^\circ$ and roughness $\sim 0.25 \text{ nm}$. Moreover, the strain relaxation is largely affected by the Ba/Ti ratio, with the stoichiometric BTO maintaining strained in c-orientation in 100-nm thickness. This finding is deviating from the literatures, and can be resulted from the almost perfect BTO stoichiometry.

On the other hand, Ba with higher temperature is also investigated to counteract the source oxidation effect. However, a small gradient is still required to stabilize the Ba flux. The BTO with increased growth rate shows larger defect density, and with too high growth rate, the value of the surface roughness increases, with the presence of clusters and small grains. The change in morphology suggests the growth mode shifts from 2D to 3D. All the changes in physical properties reflect on the optical properties. With the optimized stoichiometry and growth rate, the refractive index n shows to be identical with the bulk value, and the extinction coefficient k the smallest in the visible light range.

Finally, the Pockels effect is measured, and the Pockels coefficient of BTO films with different growth conditions are compared. Instead of orientation-dependent, the coefficient shows to be more largely affected by the film crystallinity. With smaller defect density, the Pockels coefficient is higher in value. Due to the measurement is outsourced, the correlation between Pockels coefficient and the physical properties is still lacking, and an in-house set-up is needed for more solid conclusions.

Chapter 5

PLD-grown BTO using STO / Si(001) Pseudo-substrate

The BTO grown by MBE on STO / Si was demonstrated to be elongated in the c-axis, and will transform to a-BTO only with strain relaxation by increasing in defectivity and thickness[69, 70]. To further study BTO epitaxy as well as the strain and relaxation, another growth technique is proposed, and PLD-grown BTO on STO / Si(001) pseudo-substrate is investigated in this chapter.

Compared with other deposition techniques, PLD possesses some promising features, including almost congruent deposition from ceramic target with wide material selection and epitaxial growth with higher growth rate than MBE. The higher growth rate with good uniformity after optimization are important factors for the possibility to upscale and industrialization. In addition, the chamber pressure can reach \sim 0.1 Torr, which is much larger than the \sim 1 \times 10⁻⁶ Torr for MBE chamber. The higher oxygen working pressure is expected to reduce the oxygen vacancies in the deposited films and further reduce the leakage current. However, due to the much higher working pressure, BTO epitaxial films grown by PLD are mostly reported by using oxide substrates such as MgO or perovskite oxides[155, 156, 157]. The integration of BTO on Si(001) by PLD was demonstrated by Lyu et al., who used a multi-layer oxide as the buffer layer[65]. As for the PLD-grown BTO on STO / Si(001), it still requires more detailed studies.

5.1 BaTiO₃ Epitaxial Growth on SrTiO₃ / Si(001) Pseudo-substrate

The direct STO on Si(001) epitaxy by PLD is difficult due to higher base and working pressure, which make the Si surface easily oxidized. In 2020, M. Spreitzer et al. reported the first STO epitaxy by PLD with precise pressure control to regulate both the film oxidation and growth rate, and two-step growth was required to properly oxidize the Ti without damaging the interface[158]. In addition, special chamber design in combination with RHEED was used to control the growth, including a load-lock to transfer samples and targets without affecting the main chamber, and the glovebox connected to load-lock to prevent Sr from air exposure. Instead of focusing on PLD-grown STO, here we propose another way to achieve BTO epitaxy by using a MBE STO / Si(001) pseudo-substrate. For all the PLD depositions in the following, the sample size is $38 \times 38 \text{ mm}^2$, with the STO / Si(001) pseudo-substrate diced from the 8-inch wafer. In this way, the additional error from different buffer layer quality is largely reduced, which is beneficial for the subsequent BTO lattice parameter and crystallinity comparison.

After dicing, the coupon is introduced to the PLD chamber and pumped down from atmospheric pressure for the subsequent deposition. The base pressure in the chamber is $\sim 1 \times 10^{-4}$ mbar, and after reaching the target pressure value, the substrate is heated to above 650 °C to remove impurities and for the BTO epitaxy. The pseudo-substrate stability under this high temperature and vacuum environment is confirmed by investigating the XRD and AFM differences before and after the process, and the results are shown in Figure 5.1. As shown in the XRD results, no obvious peak shift or additional phases are observed, and the ω -scan shows almost identical peak shape after annealing in the PLD chamber. For AFM analysis, improved surface roughness is observed, with smooth surface of ~ 0.13 nm is measured after the annealing. Furthermore, steps and terraces are also observed, which is resulting from the enhanced surface diffusion at high temperature. With the smooth surface, the STO / Si(001) can be used to grow BTO epitaxially as in the MBE system.

However, since PLD possesses higher growth rate and the deposition is from ceramic BTO target instead of separate metallic elements, it requires some optimization of the growth parameters to epitaxially grow BTO thin films. In addition, the vacuum break after MBE also adds uncertainty to the interface control, thus the first mission is to make sure the BTO can be epitaxially grown on this STO / Si(001) pseudo-substrate. For thin film epitaxy, the control of growth rate is crucial, which in the PLD technique is directly linked to the laser repetition rate. Different repetition rates result in ablated amount variation in a

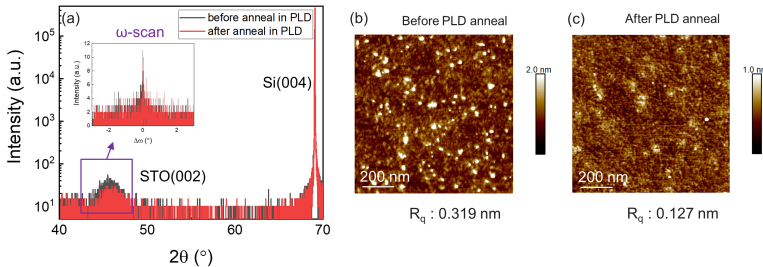


Figure 5.1: (a) XRD comparison of 4-nm STO before and after the annealing. STO AFM images of (b) before and (c) after annealing in the PLD chamber.

given duration, thus impacting the material deposition rate. As shown in Figure 5.2(a), the film with varied laser repetition rate is translated to the growth rate, and the 100-nm BTO with growth rate of 0.1 nm/s shows additional peaks other than the BTO and STO(002) peaks from symmetric ω - 2θ scan. This additional peak is from another orientation of BTO, indicating the film is polycrystalline. On the contrary, with the growth rate smaller than 0.04 nm/s, only the BTO(002) peak is observed in the symmetric scan. To verify the epitaxial characteristic, φ -scans of the asymmetric $\{202\}$ planes are measured, and the results are shown in Figure 5.2(b). The BTO structure is tetragonal, thus 4 peaks with interval of 90° are expected. The same scan is carried out for the Si $\{202\}$ peak, with 4 peaks also being observed in the 360° range. Moreover, the peaks between Si and BTO show to have a 45° -interval, which further confirms the epitaxial relationship of [110]BTO(001) // [110]STO(001) // [100]Si(001).

The STEM analysis is also used to investigate the crystallinity of BTO, and the HAADF results are shown in Figure 5.3. In Fig. 5.3(a), the BTO layer with high growth rate shows to have different orientations in lattice, confirming the polycrystalline XRD results. Moreover, the lattice misorientation starts very early in the deposition, suggesting the atoms don't have sufficient time to arrange from the beginning of the growth. On the contrary, the BTO cross-sectional STEM image with growth rate of 0.04 nm/s is shown in Fig. 5.3(b), with only occasional dislocations being observed but no polycrystalline regions are spotted. We also investigate the surface with plan-view STEM as shown in Fig. 5.3(c), which can measure the sample surface in atomic resolution. It is shown that the atoms are perfectly well-aligned after 100-nm growth without obvious defects presented, suggesting the whole BTO film is epitaxial using the STO / Si(001) pseudo-substrate. These images confirm the XRD results,

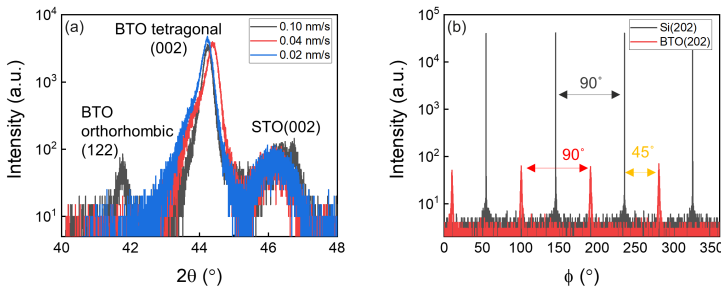


Figure 5.2: (a) XRD ω - 2θ scan results for 100-nm BTO with different growth rate. (b) XRD asymmetric ϕ -scan of Si and BTO{202} peaks for the BTO with growth rate of 0.04 nm/s. The Figure (a) is taken from the previous published work[159].

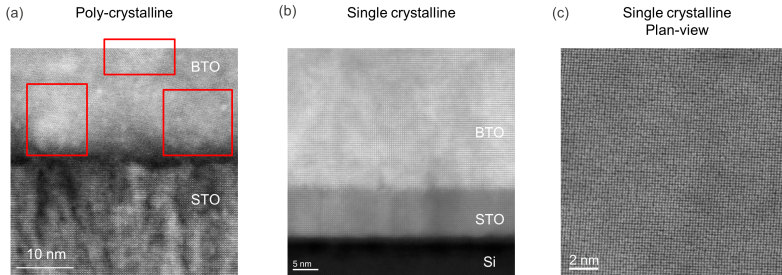


Figure 5.3: STEM HAADF analysis results. (a) poly-crystalline BTO cross-section (b) single crystalline BTO cross-section and (c) single crystalline BTO plan-view images. The red boxes highlight the different lattice orientations.

demonstrating that a too large growth rate prevents the atoms from the epitaxy on the STO buffer.

Other than growth rate, the substrate temperature is also expected to affect the crystal quality, thus the BTO with growth rate of 0.04 nm/s is further investigated by varying the substrate temperature. The XRD results are shown in Figure 5.4(a), and no additional peaks other than BTO and STO(002) peaks are observed, suggesting the growth rate is more crucial for achieving single crystalline epitaxy of BTO. Moreover, the FWHM of BTO(002) ω -scans is compared, and the growth rate also shows to have larger impact on the BTO

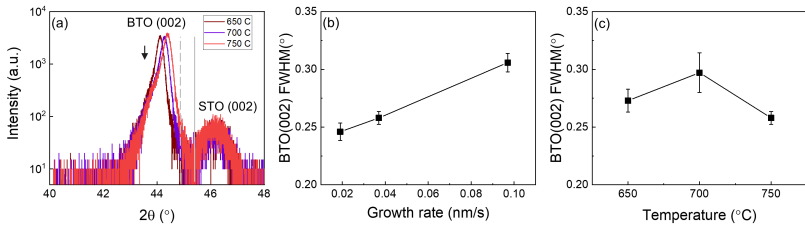


Figure 5.4: (a) ω - 2θ scans around BTO(002) with different substrate temperatures. The arrow indicates the presence of shoulder peak while the dashed and solid lines represent the bulk tetragonal BTO(002) and BTO(200) position, respectively. Comparison of BTO(002) FWHM by ω -scans as a function of (b) different growth rates and (c) temperatures. The figure is adapted from the previous published work[159].

quality than the temperature. As shown in Fig. 5.4(b), the FWHM values linearly decrease from 0.32° to 0.24° as the growth rate is reduced. On the other hand, the substrate temperature shows less impact with only slight decrease of FWHM from 0.29° to 0.26° using $750\text{ }^\circ\text{C}$.

Other than slightly improved crystal quality, the raised temperature also slightly shifts the BTO(002) peak position. As indicated in Fig. 5.4(a), the BTO with $750\text{ }^\circ\text{C}$ shows to have peak position in the largest angle, with the hint of a small shoulder peak at lower angle marked with arrow. This shift in peak position results in the out-of-plane lattice parameter variation, ranging from 4.10 \AA to 3.90 \AA with $750\text{ }^\circ\text{C}$ sample showing the smallest out-of-plane lattice parameter. The bulk BTO(002) and (200) peak positions are marked with dashed and solid lines respectively, which is used as reference for the domain orientation comparison[146]. In Fig. 5.4(a), all the BTO films are still c-oriented, but it shows that the growth conditions influence the BTO domain orientations.

5.2 BaTiO₃ Orientation Control by Growth Parameter Variation

The change of substrate temperature shows the impact on lattice parameter, suggesting the strain inside BTO film can be manipulated through the PLD growth parameters. Therefore, we vary the oxygen pressure during the growth, and it shows to largely affect the BTO lattice parameter as shown in Figure 5.5(a).

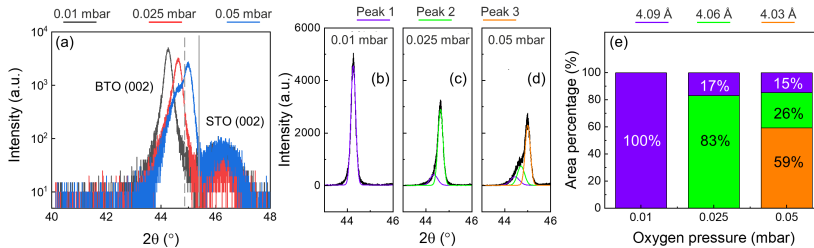


Figure 5.5: (a) symmetric ω - 2θ scan of BTO with different oxygen pressure. (b)-(d) deconvolution of BTO(002) peak with the same color represented the same sub-peak position. (e) area percentage summary of deconvoluted sub-peaks. The figure is adapted from the previous published work[159].

As the oxygen pressure increases, the BTO(002) peak position shifts toward higher angle, which indicates the out-of-plane lattice parameter becomes smaller. Among these BTO, the 0.05 mbar sample shows even larger peak position than the bulk tetragonal (002) peak, suggesting the change of elongation axis into the in-plane direction. Together with peak position shift, the peak shape also becomes asymmetric with the clear appearance of a shoulder peak at smaller angle. Thus, an accurate peak deconvolution is performed to further analyze the complex diffraction peak, and the results are shown in Fig. 5.5(b)-(d). For the 0.01 mbar sample, only a single peak is observed with the calculated lattice parameter of 4.09 Å. The 0.025 mbar sample shows to have one shoulder peak with a lattice parameter of 4.09 Å while the main peak is located at higher angle with the lattice parameter of 4.06 Å. For the 0.05 mbar BTO, the main peak is located at even higher angle while two sub-peaks are fixed at lower angle with the same position compared with the 0.025 mbar sample. The area percentage of these various contributions is summarized in Fig. 5.5(e). As the oxygen pressure increases, the out-of-plane lattice parameter slowly shrinks, with 0.05 mbar BTO shows ~60 % of the film possessing the lattice parameter of 4.03 Å. The change of lattice parameter is strongly linked to the strain relaxation effect, with the high oxygen pressure accelerating this process. In the 0.05 mbar BTO sample, there are still small fractions of the film that are measured with larger lattice parameter of 4.09 Å, suggesting some parts are still strained. Based on the XRD results, the BTO can be categorized into c-BTO, mixed-BTO and a-BTO with the increase of oxygen pressure during the growth by PLD.

A reciprocal space mapping (RSM) around BTO(002) is performed and the results are shown in Figure 5.6. With the increase of oxygen pressure, the BTO contour clearly becomes asymmetric, which corresponds to the observation of

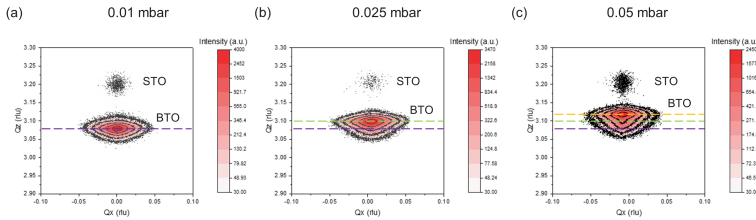


Figure 5.6: RSM around BTO and STO(002) for BTO with (a) 0.01 mbar (b) 0.025 mbar and (c) 0.05 mbar oxygen pressure. The dashed lines with different colors are corresponded to the sub-peak positions from the Fig. 5.5(b)-(d).

shoulder peak as in Fig. 5.5(a). We can extract the FWHM of BTO(002) reflections from these scans to compare the crystallinity, and it shows the value is raised from 0.25° to 0.45° with the elevated oxygen pressure, suggesting the mosaicity is increased in the film. This increase in mosaicity is the result of the accelerated strain relaxation, which creates defects and broadens the XRD peak[160, 161].

The crystallinity evolution due to the change in oxygen pressure is also reflected on the final film morphology. As shown in Figure 5.7, the surface roughness shows clear deviation among BTO samples with different oxygen pressure. Similar to XRD results, the BTO with lower oxygen pressure not only shows smaller FWHM, but also the smoother surface of ~ 0.5 nm. However, compared with MBE-grown BTO, the surface is much rougher by PLD deposition, and a granular structure of BTO is observed in all samples. The increased roughness shows the growth in PLD is changing from 2D growth to 2D + 3D mode, and the variation in growth conditions further enhance this difference. With higher oxygen pressure, the granular size becomes smaller with larger roughness, and the 0.05 mbar sample even shows large clusters above these granular structure with the diameter of ~ 100 nm and height of $\sim 10\text{-}15$ nm. The high oxygen pressure sample shows similar AFM results with the high growth rate MBE-grown BTO (see Fig. 4.13(c)), suggesting the atoms don't have enough time or energy to diffuse and form the layer-by-layer growth. When performing the PLD deposition, the ambient pressure will impact the kinetic energy of the species from target[162]. With high ambient pressure, the chances of collision increases, thus the final kinetic energy of the deposited species is lowered. With smaller kinetic energy, these deposited atoms are expected to travel less, thus various clusters are formed and roughen the surface as shown in Fig. 5.7(c).

The increased boundaries between granular structures can impact and accelerate

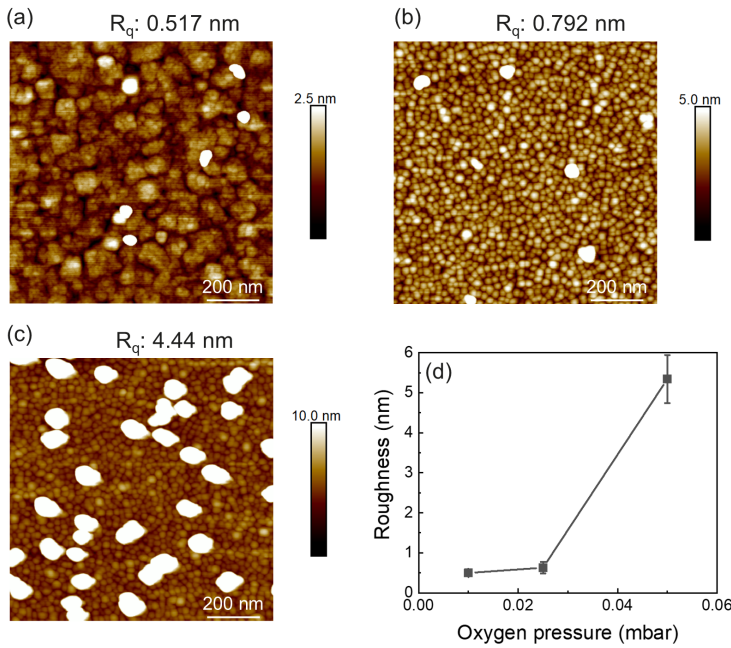


Figure 5.7: BTO surface roughness by AFM with oxygen pressure of (a) 0.01 mbar (b) 0.025 mbar and (c) 0.05 mbar. The values shown are the root-mean-square roughness. (d) shows the surface roughness increases together with the oxygen pressure.

the strain relaxation, thus the NBD analysis is performed on different orientated BTO (a-, mixed, c-) with the mapping of the in-plane and out-of-plane lattice parameter as shown in Figure 5.8. From in-plane NBD mapping, we can identify BTO domains with regions in the same lattice parameter. In Fig. 5.8(a), the c-oriented BTO shows to have domain size ~ 50 nm with clear domains presented in the mapping. On the contrary, the a-BTO in Fig. 5.8(c) shows much smaller domain size with only ~ 20 nm in lateral direction, and the boundaries between different domains are less obvious. The decrease of domain size is consistent with AFM results, showing the granular structures do affect the domain and strain distribution. For the out-of-plane NBD results, the strain relaxation is much more obvious. As shown in Fig. 5.8(f), the out-of-plane lattice parameter is larger close to the BTO / STO interface, and gradually becomes smaller with increasing thickness. Compared with a-BTO, the BTO lattice parameter of c-BTO is more uniform throughout the whole thickness as shown in Fig. 5.8(d).

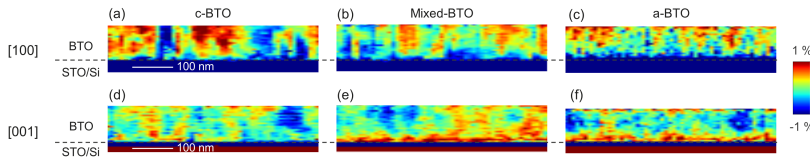


Figure 5.8: Strain mapping by NBD analysis results of BTO with different domain orientations. (a)-(c) are along [100] in-plane direction and (d)-(f) are in out-of-plane [001] direction.

The NBD can further be quantitatively compared by using STO lattice as reference, and the lattice mismatch profiles based on the reference are plotted in Figure 5.9. For the in-plane lattices, the a-BTO and mixed-BTO show slightly larger lattice parameter than the c-BTO, which means the compressive strain is more relaxed in these films. For the out-of-plane profile, even more obvious differences are observed, with a-BTO presenting the smallest lattice parameter. When comparing the out-of-plane profile with XRD results, the three deconvoluted peaks in 0.05 mbar BTO can be attributed to the varied lattice parameters from Fig. 5.9(b) in different thickness. As demonstrated, the largest lattice parameter is close to the STO interface, which corresponds to the 4.09 Å from XRD analysis. Likewise, the 4.03 Å corresponds to the central part of the BTO while the 4.06 Å is linked to the part close to sample surface. Moreover, the area percentage matches well with the thickness distribution. In the 100-nm BTO, the largest lattice parameter close to STO shows to have thickness around 15-20 nm, while the smallest lattice parameter possesses the largest percentage. The deconvoluted peak area is consistent with the thickness shown in the lattice mismatch profile.

The granular structure observed by both AFM and TEM is linked to different degree of relaxation in BTO films. For the high oxygen pressure sample, the film shows to have smaller domain size with higher density of boundaries, which facilitate the strain relaxation via these domain boundaries[163]. Another possible explanation for the accelerated strain relaxation using higher oxygen pressure could be linked to the amount of oxygen vacancy. It is reported in some perovskite systems such as LaSrCoO (LSCO), that the large amount of oxygen vacancies would re-order on the Co-O planes, which retains strain inside the perovskite films[63, 164, 165]. However, the re-ordering of oxygen vacancies is not reported in BTO films, thus the mechanism for PLD-grown BTO strain relaxation still requires more experiments and deeper analyses before jumping to the final conclusion.

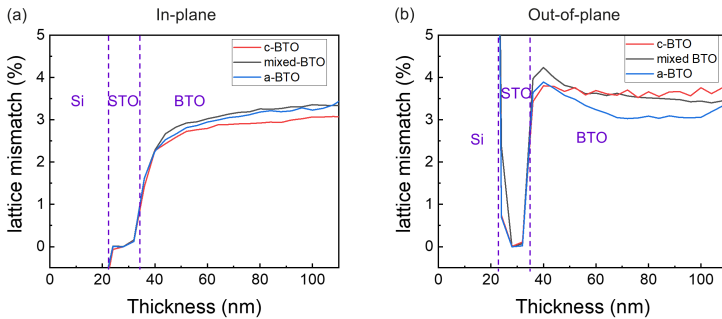


Figure 5.9: Lattice mismatch profile from NBD analysis using STO as reference in (a) in-plane and (b) out-of-plane direction. For the a-BTO, it still contains $\sim 15\text{-}20$ nm thickness which is strained in c-orientation close to the BTO / STO interface. The figure is adapted from the previous published work[159].

5.3 Electrical and Optical Characterization of BaTiO₃ with Different Orientation

The change of domain orientation is expected to have a large influence on the electrical and optical properties. Due to the fact that BTO is a ferroelectric material, the domain orientation in BTO thick film will also impact the piezo-response from the ferroelectric materials as measured by piezo-force microscopy (PFM) characterization. Thus, the BTO with different oxygen pressure is investigated by PFM to electrically characterize domain orientations, and the PFM amplitude and phase mapping results are shown Figure 5.10. In our PFM analysis, the conductive tip is scanning on the BTO surface while the heavily doped p-type Si(001) substrate is grounded; thus, the electric field is oriented along the z direction. As shown in the Fig. 5.10, the c-BTO shows large response while the mixed-BTO also responds but with smaller magnitude; on the contrary, the a-BTO shows no response even with high voltage applied to the tip, suggesting the BTO domain orientation is parallel to the in-plane direction.

The PFM butterfly curves also confirm the amplitude mapping results, which are plotted in Figure 5.11. When applying the electric field along the BTO domains, the dipoles will align with the field when the voltage is large enough, resulting in strong piezo-response from the ferro-material. Thus, with more dipoles following the applied electric field, a larger response will be measured. In Fig. 5.11, the c-BTO shows much larger hysteresis loop compared with the mixed-BTO,

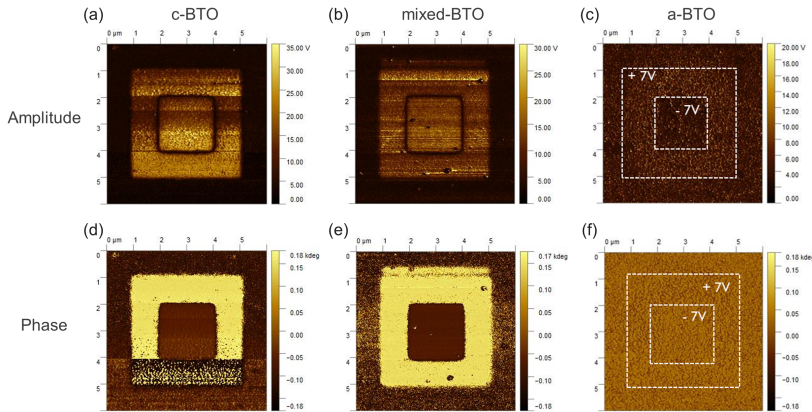


Figure 5.10: PFM amplitude maps of (a) c-BTO (b) mixed-BTO and (c) a-BTO. The phase maps are shown in (d)-(f). The a-BTO sample shows no piezo-force response.

suggesting more domains lying along the out-of-plane direction. Moreover, for the a-BTO, no butterfly curve could be obtained, which further confirms the dominating in-plane domain orientation presented in the high-oxygen a-BTO film.

The I-V and C-V measurements are also used to characterize the PLD-BTO domain orientations. Prior to the characterization, 10-nm Au is deposited on BTO surface using shadow mask to define the electrodes. On the backside of the substrate, 100-nm Al is deposited to further reduce the contact resistance with the measuring chuck. The circular top electrode with diameter of 200 μm is used for both I-V and C-V measurements, and the electrical characterization results are demonstrated in Figure 5.12. For the I-V measurement, different voltage biases are applied on the top Au electrode while the p⁺Si(001) substrate is in direct contact with the chuck and grounded. When applying small bias to the stacking, no obvious hysteresis loop is observed. However, when the voltage is larger than 2.5 V, a small hysteresis loop starts to appear, as plotted in Fig. 5.12(a). More obvious hysteresis is observed with even larger bias, and all the BTO samples show this similar behavior. These results are explained by the ferroelectric properties of the BTO films, with the poling electric field of ~ 500 kV/cm matching well with the reported values[166, 167].

For BTO samples with different oxygen pressure, the I-V measurement doesn't show much deviation with different growth parameters. Thus, other electrical measurement using C-V analysis is performed, and the results are shown in Fig.

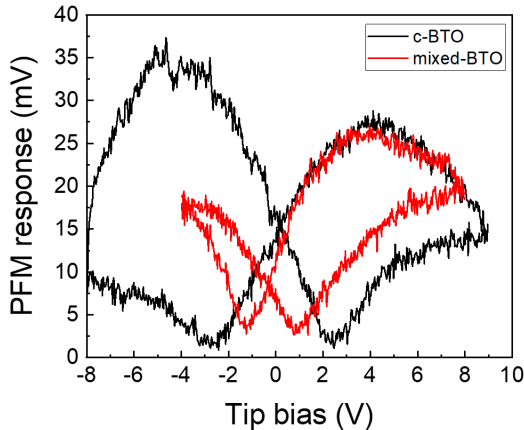


Figure 5.11: Butterfly curve by PFM. The hysteresis effect is result from dipoles alignment, thus the more dipoles aligning to the electric field, the larger the hysteresis loop can be observed. The a-BTO shows no response when applying a tip bias to the sample.

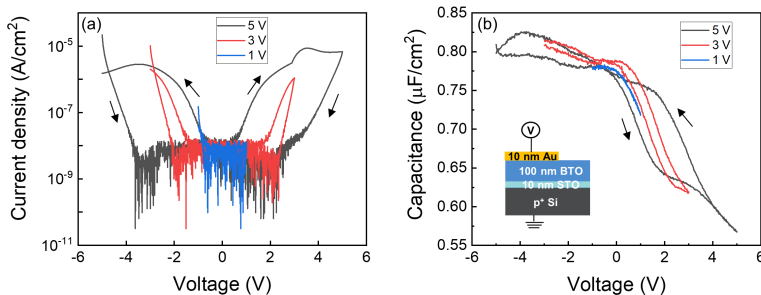


Figure 5.12: Electrical measurement results of (a) I-V curve and (b) C-V curve at 1 MHz using different voltage biases. The hysteresis behavior is not observed in small bias. Figure (a) is taken from the previous published work[159].

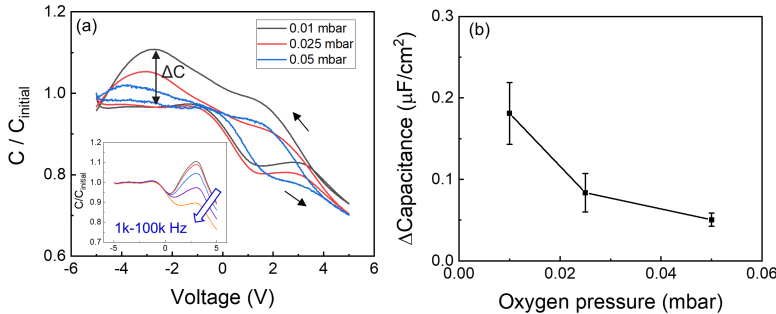


Figure 5.13: (a) Normalized C-V curve at 1 MHz of different oxygen pressure BTO films. The inset is the multi-frequency C-V from 1 kHz to 100 kHz, which shows a clear inversion layer formation after normalizing the values to the initial accumulated capacitance. (b) the maximum capacitance difference between the forward and backward accumulated capacitance values. The figure is adapted from the previous published work[159].

5.12(b)). At 1 MHz frequency, the similar trend as I-V measurement is observed, with large enough of applied voltage shows the hysteresis behavior.

When the voltage is larger than ± 2.5 V, the loop is observed in all BTO samples but with different magnitude of hysteresis, as presented in Figure 5.13(a). During the measurement, the voltage is applied on the top electrodes from -5 V to 5 V, and then back to -5 V with frequencies variation from 1 kHz to 1 MHz. As shown in the inset of Fig. 5.13(a), at low frequency, the C-V curve shows obvious inversion layer formation with the increase in capacitance after 0 V; on the other hand, with the increase of frequency, the capacitance curves become flatter in the positive voltage range because the charges are not able to follow at high frequency[168]. Among all the BTO samples, the 0.01 mbar BTO film shows the largest hysteresis response, and the capacitance difference in the accumulation region between forward and backward curve is summarized in Fig. 5.13(b).

Considering dipoles together with the charge distribution, the hysteresis C-V curve could be explained by these combined effects, and the detailed mechanisms are plotted in Figure 5.14. When the C-V measurement starts with -5 V, the stacking is in accumulation region with many positive charges accumulated in the oxide / p-Si interface. Moreover, since -5 V is large enough to pole the dipoles, the dipoles are aligned inside the BTO film with positive charge

closer to the surface. As the voltage starts to increase toward zero, less charge is accumulated, and the number of polarized-up dipoles also reduces, finally reaching the flat-band condition. After the flat-band voltage, the positive bias mainly depletes the p-type Si, with little voltage change crossing the BTO film. Thus, the dipoles inside BTO remain unchanged. However, when the applied voltage is larger than 3 V, the capacitance is further reduced, as now the dipoles are poled again in reverse direction. Due to the formation of polarized-down dipoles, the total charge at the interface is decreased. By the definition of capacitance, where

$$C = \frac{dQ}{dV} \quad (5.1)$$

as the dQ is decreasing, the measured C is thus lowering too[168]. For the backward curve, similar dipoles and charge behavior are expected but in reverse direction. Finally, when the voltage is further decreased to smaller than -3 V, the dipoles are formed and polarized-up again, reducing the capacitance and ending the backward curve to the same initial value. Based on the illustrated mechanism, the capacitance difference in the accumulation region between backward and forward curve roots from BTO dipoles in the out-of-plane orientation, thus the ΔC is linked to the number of c-oriented domains. As shown in Fig. 5.13(b), the largest ΔC is observed in the 0.01 mbar sample, which further confirms the domain orientation shift from c-BTO to a-BTO when using higher oxygen pressure.

Other than ferroelectricity, C-V hysteresis loop could also be correlated to the charged defects inside BTO films. For the film deposited in vacuum, the positively charged oxygen vacancies have high chance to exist, which will result in the opposite hysteresis direction compared to the effect resulted from ferroelectric dipoles[169, 170]. Since the overall hysteresis loop is affected by both charged defects and ferroelectric dipoles, it would be difficult to use C-V measurement for oxygen vacancy analysis in the BTO films.

Dielectric constant of BTO can also be obtained by the C-V measurement, with the calculation from accumulated capacitance expressed by the equation[171]:

$$C_{meas}^{-1} \propto \left(\frac{\varepsilon'_{eff,BTO}}{t_{BTO}} \right)^{-1} + \left(\frac{\varepsilon'_{STO}}{t_{STO}} \right)^{-1} \quad (5.2)$$

where the ε' is the real part of permittivity and t is the thickness of the layer. For the STO buffer layer, the permittivity should be a constant since almost no ferroelectricity existed in the very thin and cubic STO layer. If considering a

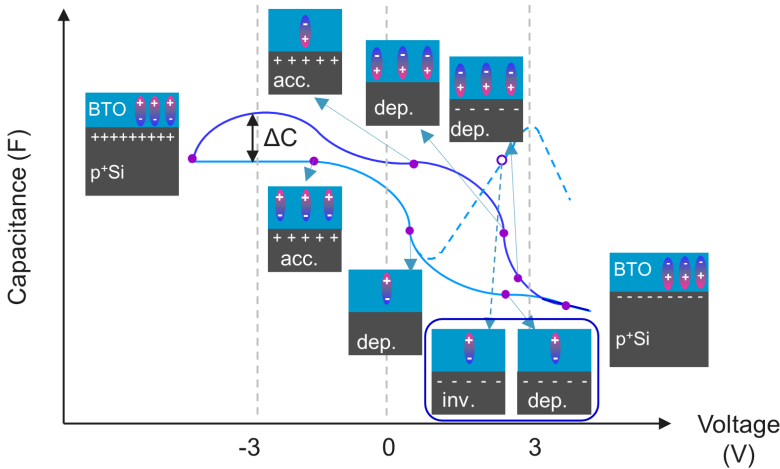


Figure 5.14: Illustration of hysteresis BTO C-V curve with detailed dipoles and charge distribution. The dashed curve represents the behavior at low frequency. The figure is adapted from the previous published work[159].

wide frequency range, the permittivity is dependent on the frequency, with the higher the frequency, the smaller the permittivity. Different mechanisms are responsible for the dielectric relaxation as the applied frequency changes, and within 1 kHz to 1 MHz the dipolar relaxation is dominating[172, 173]. Based on the C-V curve, the dielectric constant at frequency smaller than 100 kHz is calculated, and the averaged value is 130, which is in the range of reported values[174, 175].

The change of domain orientation using different oxygen pressure not only impacts the electrical properties, but also influences the optical indices. The optical indices of different orientation BTO films are investigated by SE using Mueller matrix measurement, which can extract the refractive index from different optical axes. When performing the measurement, the polarizations of incident and reflected beam are collected, and the Mueller matrix can then be calculated and fitted to connect the beam polarizations with the equation:

$$\begin{bmatrix} S'_0 \\ S'_1 \\ S'_2 \\ S'_3 \end{bmatrix} = \begin{bmatrix} m_{11} & m_{12} & m_{13} & m_{14} \\ m_{21} & m_{22} & m_{23} & m_{24} \\ m_{31} & m_{32} & m_{33} & m_{34} \\ m_{41} & m_{42} & m_{43} & m_{44} \end{bmatrix} \begin{bmatrix} S_0 \\ S_1 \\ S_2 \\ S_3 \end{bmatrix} \quad (5.3)$$

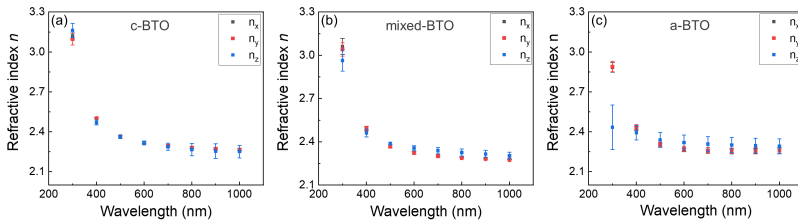


Figure 5.15: Refractive indices in different axes of (a) c-BTO (b) mixed-BTO and (c) a-BTO, which are extracted by SE with Mueller matrix measurement.

where the S_0-S_4 is the component in Stokes vector representing different beam polarization orientations[176, 177]. By carefully measuring the beam polarization, the component inside the Mueller matrix can be fitted, hence the refractive index in different optical axes can be extracted.

The refractive index n of BTO layers with various oxygen pressure is extracted after fitting the Mueller matrix, and the results are shown in Figure 5.15. Multiple fittings are performed on the sample to test the stability of the model, and the generated deviation between different fittings are included in the figure for a more thorough comparison. In all BTO samples, the refractive indices in x - and y -direction are very similar, while in the z axis, more prominent deviations are observed. For the c-BTO in Fig. 5.15(a), the refractive indices of the 3 axes are very close, with only slightly larger n_z at 300 nm wavelength and becomes slightly lower than n_x and n_y at wavelength longer than 800 nm. As the domain orientation starts to change, the n_z also shifts to flatter slope, with obvious decrease in n values at 300 nm. For a-BTO in Fig. 5.15(c), the n_z at 300 nm shows obvious decrease with large refractive index difference reaching ~ 0.5 between z and other 2 axes. Moreover, the increase in n_z after 500 nm also results in the refractive index difference of ~ 0.05 with now the n_z larger than the other 2 axes. As a reference, the refractive indices of bulk BTO also show differences in different axes, with n_o of 2.488 along x - and y -axes and n_e of 2.424 along z axis at 514 nm, suggesting the refractive index is smaller along the elongated axis[22]. Considering the refractive indices in a-BTO, the reverse correlation between n_z to n_x and n_y can be another indication of the change of elongated axis direction.

Unlike stoichiometric MBE-grown BTO, even with the reverse of refractive index, the n values of PLD-grown BTO are still smaller compared with the bulk BTO values. The refractive index comparison of PLD-grown BTO with the MBE stoichiometric one as a function of density is summarized in Figure

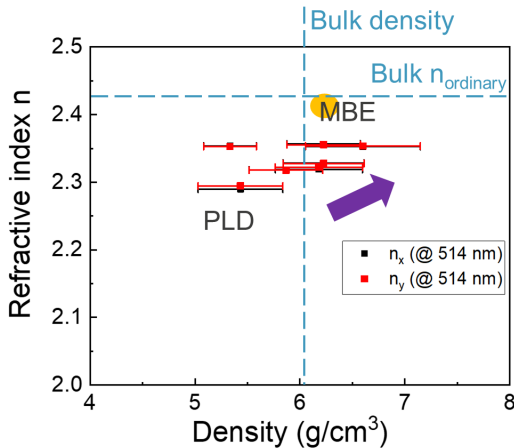


Figure 5.16: Refractive index n comparison as a function of film density obtained by XRR.

5.16. The refractive index is reported to be impacted by density, with the larger the density, the higher the refractive index could become[122, 178]. In Fig. 5.16, the film density is extracted by XRR measurement, and all the BTO films with different PLD parameters are included. The BTO refractive indices do increase with larger fitted film density, but the highest n value is still smaller than MBE samples. For the PLD samples, the granular structure observed by AFM reduces the film density; moreover, even with high density, more defects are expected in the PLD-grown BTO film since the deviation from the bulk refractive index is an indication for the deviation from pure monocrystalline thin film[154].

5.4 Conclusion

Compared with MBE, PLD shows easier stoichiometry control and higher in oxygen pressure to reduce the leakage current and oxygen vacancies. However, the controllability of deposited atoms is worse, making the direct epitaxy of perovskite oxide on Si substrate extremely difficult. In this chapter, we demonstrate the combination of MBE and PLD technique by using the MBE-grown STO / Si(001) pseudo-substrate for the PLD epitaxy. The STO grown on

Si is stable, and with proper setting of growth parameters, the BTO is proved to follow the lattice of STO and to grow epitaxially.

The PLD parameters can be further adjusted to change the BTO domain orientation, which evolves from c- to a-BTO with raised oxygen pressure. As the oxygen pressure increases, both XRD and NBD show the lattice parameters are changed, with now the elongated axis lying in the in-plane direction for the 0.05 mbar BTO samples. By AFM analysis, the film also shows the change of domain size with higher domain boundary densities observed for high-oxygen pressure sample. This increase in boundary densities could accelerate the strain relaxation, finally leading to the BTO domain orientation change.

The effect of different domain orientations is also inspected both electrically and optically. For I-V measurement, all the BTO films show hysteresis behavior when applying a large enough electric field, suggesting the dipoles inside the BTO are poled. Similar behavior is also observed in C-V measurement with backward curve shifts counterclockwise to the forward curve, which is linked to the charges and dipoles orientations. The domain orientations in BTO film also impact the optical properties, and the SE with Mueller matrix is used to extract the n values along different optical axes. With high oxygen pressure, the n values in z -axis are shown to be slightly larger than the values in x - and y -axis. This correlation between out-of-plane and in-plane refractive indices are reversed for low-oxygen pressure sample, with n values in z -axis smaller than the other two axes. Finally, n values comparison with MBE-grown BTO is performed as a function of film density, and the results show the PLD-grown BTO is still not as perfect as MBE ones with smaller n values being extracted which is linked to film density and quality.

Chapter 6

Alternative Buffer Layer and Substrate for BTO Orientation Control

In our MBE or PLD-grown BTO, the BTO grown on STO / Si(001) shows to favorize c-oriented BTO growth. Based on Pockels tensor described in Equations 1.3 and 1.4, the a-BTO poled by in-plane electric field can generate larger Pockels response than c-BTO. As demonstrated in previous chapters, to change BTO orientation into a-oriented, the compressive strain will need to be relaxed via dislocations or domain boundaries. This c-to-a transition will sacrifice the BTO film crystallinity which will then penalize devices that require high quality of BTO films. In this chapter, we propose another approach to control the BTO orientation. By replacing the usual STO / Si pseudo-substrate by alternative perovskite buffers or different substrates, the strain in BTO can be controlled in between compressive and tensile strain. In this way, the film is expected to obtain the desired orientation without the necessity to relax it by defects generation. In this chapter, the first section contains literature reviews on the possible candidates for alternative substrates and buffers to generate tensile strain in BTO. Then, the experimental works on SrZrO_3 buffer layer, as well as the BTO grown on different buffers will be discussed in the 2nd and 3rd section.

6.1 Alternative Substrate and Buffer Candidate: Literature Review

6.1.1 Alternative Substrate

Ge substrate

The direct growth of BTO on Ge without buffer layer is feasible due to the negligible lattice mismatch of only $\sim 0.3\%$ after 45° rotation of the BTO lattice with respect to the germanium one. Moreover, compared with Si, the GeO_x is less stable than SiO_x , and can be easily removed with high temperature[179]. It is demonstrated that a clean (2×1) reconstructed $\text{Ge}(001)$ surface can be obtained using oxygen plasma first to remove surface impurities, followed by a high temperature anneal in vacuum environment[180]. Since the GeO_x is less stable and can be easily removed via annealing in vacuum, other deposition techniques such as PLD and ALD are also proposed for the BTO / Ge epitaxy[181, 182].

For the BTO-on-Ge epitaxy, the $\text{Ge}(001)$ surface is passivated by a $1/2$ ML of Ba, identical to the case Sr on $\text{Si}(001)$, in order to prevent the GeO_x formation and promote the 45° rotation of the BTO lattice[183, 184]. With such BaO / Ge template, the epitaxial BTO layer was reported by Fredrickson et al. to possess good crystallinity, who demonstrated a sharp BTO / Ge interface by HAADF TEM and a FWHM value of 0.7° for a 40-nm thick film, as shown in Figure 6.1[185]. Due to the small lattice mismatch, the epitaxial film grows relaxed, resulting in a near-cubic BTO film with the c/a ratio very close to unity. Such cubic BTO phase on Ge substrate thus shows no obvious ferroelectric property, and a buffer layer like SrTiO_3 is required in order to induce strain for c-oriented BTO growth using Ge substrate[181, 186].

MgO substrate

The MgO substrate option can be a promising candidate due to its large bandgap and low refractive index of $n \sim 1.73$, which is ideal for the BTO waveguides application[187, 188]. Moreover, this stable oxide substrate opens up various growth techniques for BTO epitaxy, including PLD, CVD and RF-sputtering[189, 190, 191]. The BTO / MgO is epitaxial, and the BTO(002) FWHM by XRD can reach $\sim 0.5^\circ$ for 300-nm thickness[190]. When comparing the BTO lattice parameter with MgO one, the lattice mismatch is around 4.2% with MgO having a larger lattice parameter, which will produce a tensile strain in the BTO layer. However, the thermal coefficient mismatch between BTO and MgO is $> 65\%$ with MgO larger than BTO, which results in

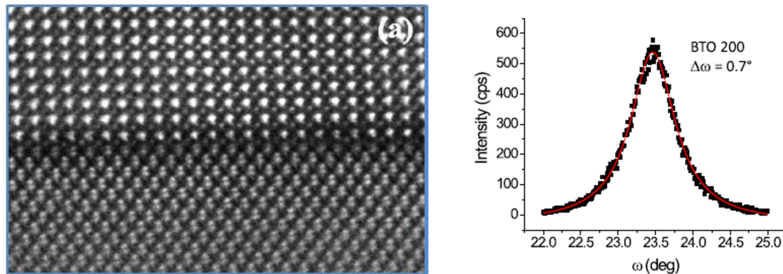


Figure 6.1: BTO on Ge(001) epitaxy with TEM and XRD results adapted from Ref.[185]. The growth procedure is similar to that of STO / Si(001) epitaxy, with Ba atoms sit in between Ge dimers to enable the 45° lattice rotation. Due to the very small lattice mismatch, the BTO grown on Ge tend to be in cubic phase.

compressive strain[175]. Combining these two opposite effects, the final BTO is reported to possess different orientations of both c- and a-BTO, and the polarization orientation is largely impacted by the growth parameters[188, 192]. To control the BTO orientation on MgO substrate, various approaches are reported, including oxygen pressure variations and annealing to accelerate the strain relaxation, as shown in Figure 6.2(b)[157, 193]. This procedure produces similar effect to the work we performed on the PLD-grown BTO in the previous chapter (chapter 5). When comparing with the BTO grown on STO, the large lattice mismatch between BTO and MgO results in worse crystallinity[194]. Moreover, MgO is reported to easily absorb the moisture and form the $Mg(OH)_2$ clusters on the surface[195]. All these effects produce disadvantages when considering the use of this substrate.

6.1.2 Alternative Buffer

To change the strain direction from compressive to tensile inside the BTO layer, other than alternative substrates, new buffer layers with larger lattice parameters than BTO are considered as potential solutions. The lattice parameter comparison between some perovskite oxides is summarized in Figure 6.3, and a few important buffer candidates is reviewed in the following section. As depicted, with lattice mismatch larger than zero, the oxide epitaxial layer will tend to be oriented in c-orientation. When comparing lattice parameters

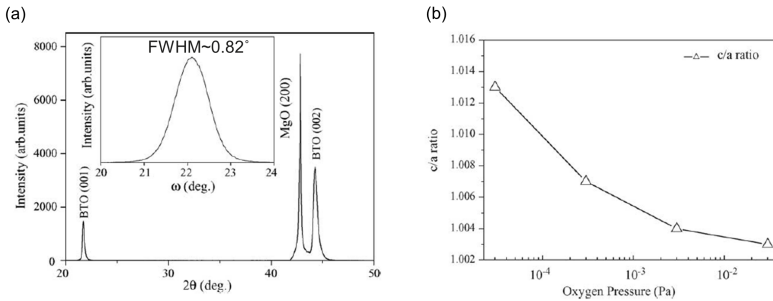


Figure 6.2: (a) XRD results of BTO epitaxy on MgO substrate. (b) The lattice parameter c/a ratio of BTO changes as a function of different oxygen pressure. The BTO domain orientation largely depends on the growth parameters, with the strain relaxation process similar to the PLD-grown BTO described in chapter 5. These figures are adapted from Ref.[192].

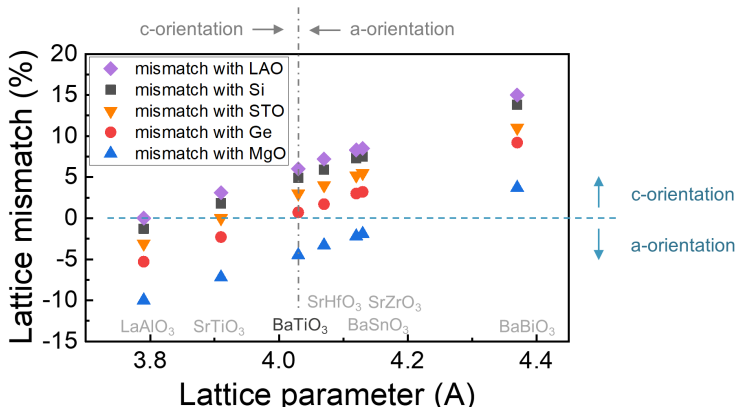


Figure 6.3: Different perovskite oxides lattice parameter comparison, including lattice mismatch grown on both Si, Ge, and oxides substrates. On the y-axis, lattice mismatch with BTO is shown. The lattice parameter values are adapted from Ref.[196, 197, 198, 199].

between different perovskite oxides, the buffer layer with larger lattice parameter than BTO should create tensile strain, resulting in a-BTO formation.

BaSnO₃

The BaSnO₃ (BSO) perovskite oxide presents a lattice parameter of 4.12 Å, resulting in 2.2 % lattice mismatch with BTO, which should create an in-plane tensile strain if used as buffer layer. To epitaxially grow this material, however, almost all growths are reported using oxide substrates, such as STO and DyScO₃; together with the substrate choice, a wide range of growth techniques ranging from high-vacuum MBE to chemical solution deposition are reported[200, 201, 202]. Due to the high vapor pressure of Sn in vacuum, the growth of BSO requires more reactive oxidation gas or chemical precursors, in which the species already bonded to oxygen, to fully oxidize the metallic species and then to control the stoichiometry in the film[203, 204]. Thus, the direct epitaxy of BSO on Si or Ge substrate is impossible. The integration of epitaxial BSO on Si was reported by Wang et al., but it required a thin STO buffer layer on Si first, then the BSO could be grown in adsorption-controlled regime, as shown in Figure 6.4[205]. The BTO grown on BSO buffer was also demonstrated by Reynaud et al. with the usage of a STO bulk substrate, and it shows good crystallinity with small BTO(002) FWHM of only ~0.12°[206]. Furthermore, the polarization of BTO / BSO / STO was illustrated to align in in-plane orientation, which further consolidated the expectation to control BTO orientation by using alternative buffer layers.

SrHfO₃

The perovskite oxides that can be directly grown on Si or Ge substrate are scarce, since it requires thermodynamically stability of the different elements to form clean and sharp interface and should also be properly oxidized with limited oxygen pressure. The SrHfO₃ (SHO) is a promising candidate since both the Sr and Hf elements are stable in contact with Si and can be gently oxidized by molecular oxygen to form stoichiometric film, which enables the direct epitaxy on Si and Ge substrate. Due to the atomic radii of Hf, the lattice parameter of SHO is quite large (4.07 Å), which will create 5.9 % and 1.7 % of mismatch on Si and Ge substrates respectively with the 45° in-plane rotation[207, 208]. Despite the large mismatch on Si, the epitaxy of SHO is reported on both substrates, showing excellent insulating properties such as high dielectric constant of ~19 and low leakage current density, which are all promising for MOSFET applications[209, 210, 211]. The usage of SHO as gate oxide was reported by Rossel et al., and the results were shown in Figure 6.5[210]. With the 4-nm epitaxial SHO / Si(001) grown by MBE, the characteristics as gate dielectric for both n- and p-MOSFET were demonstrated.

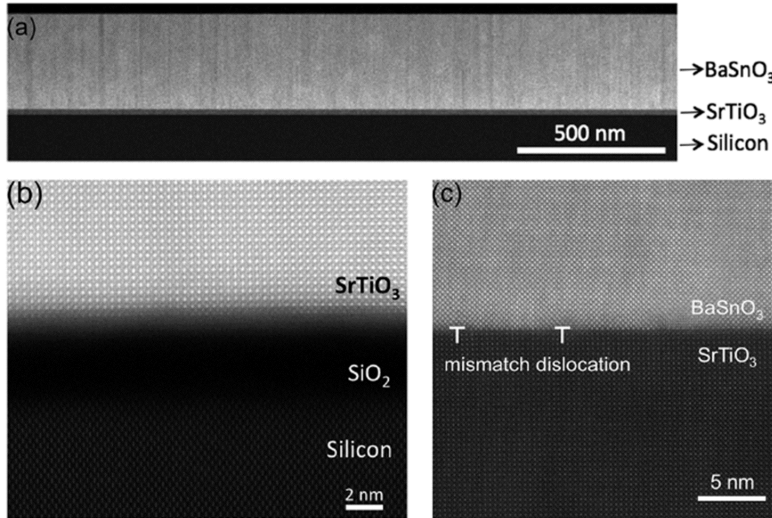


Figure 6.4: Epitaxial BSO on Si(001) was demonstrated using thin STO as buffer. (a) low magnification STEM image of the whole stacking. (b) STO / Si(001) interface and (c) BSO / STO interface high-resolution STEM images. The figures are adapted from Ref.[205].

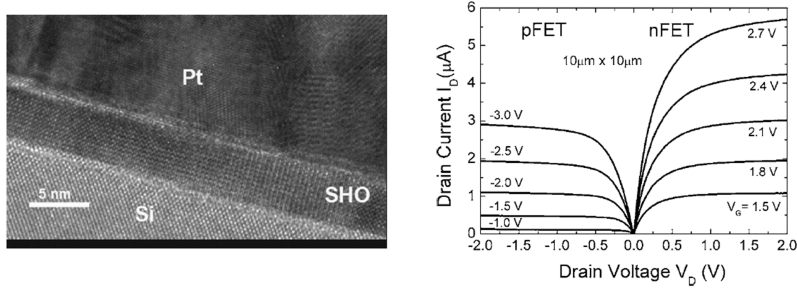


Figure 6.5: The epitaxial SHO on Si could be a promising candidate for gate-dielectric application. The figures are taken from Ref.[210].

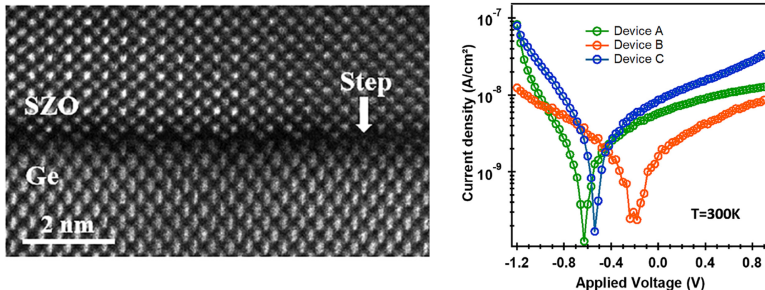


Figure 6.6: The epitaxial SZO on Ge is demonstrated, and the leakage current density is very low, making the material a promising candidate for gate oxide application. The different samples marked in the I-V curve correspond to different oxygen treatments. These figures are taken from Ref.[213].

SrZrO₃

Another promising candidate is SrZrO₃ (SZO) perovskite oxide, which generates similar lattice mismatch (2.5 %) than BTO on STO but in the opposite strain direction. Lim et al. demonstrated the SZO on Ge(001) by MBE, who reported a 15-nm film with small XRD FWHM value of 0.63° for the SZO(002) reflection and a relaxed lattice parameter of 4.13 Å[212]. The SZO is a promising gate oxide material, with the epitaxial film on Ge substrate showing a very low leakage current density, as illustrated in Figure 6.6[213]. Moreover, the dielectric constant is reported to be ~ 30 , which can reduce the equivalent oxide thickness (EOT) to 0.8 nm at 1 MV/cm with the leakage current density of 2×10^{-8} A/cm². However, the available SZO epitaxy studies are still scarce, and more optimization is needed to further improve SZO crystalline quality.

6.1.3 Literature Summary and Outlook

The BTO orientation control approaches via using different substrates and buffers are summarized in Figure 6.7, which clearly shows that the use of STO favorizes the c-orientation of BTO. For a-oriented BTO, new buffer layers present today the largest potential for controlling tensile strain in BTO with good quality. Other than the lattice parameter, the thermal expansion coefficient of the substrate and buffer layer can also affect the strain in BTO. Considering the thermal expansion coefficient of the Si substrate and these perovskite oxides, Si shows to be the smallest among these materials, thus the lattice parameter

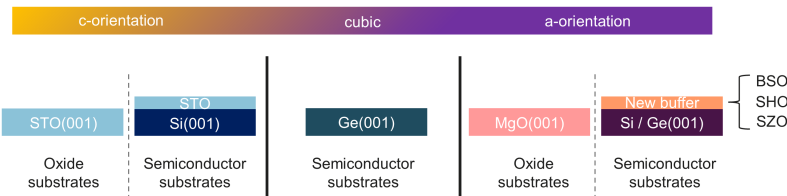


Figure 6.7: Summary of BTO orientation as a function of different buffers and substrates.

of the grown material will all be slightly larger than their bulk values when using Si as the substrate[69, 214, 215]. As a result, for the already larger lattice parameters of these alternative buffers, the tensile strain is thus expected. Various epitaxial perovskite oxides grown on semiconductor substrates are reported, and we selected SZO as the first candidate especially because of the opposite mismatch compared to the BTO / STO case. In this chapter, the epitaxial growth of SZO will be studied on both Si and Ge substrates. In a second stage, we will grow BTO on top of the SZO epitaxial layer and study the strain and relaxation in the BTO layer.

6.2 SrZrO₃ Buffer Layer Epitaxy

6.2.1 SrZrO₃ on Si Epitaxy

The SZO is first grown on 8-inch Si(001) substrate with the procedure presented in Figure 6.8. The starting procedure is identical to the STO growth on Si, with 1/2 ML Sr deposited on the (2 × 1)-reconstructed Si(001) surface at high temperature, and then cooled down for the SZO growth. The initial stage of SZO epitaxy is similar to the STO, with first a controlled oxygen exposure prior to the growth, followed by the co-deposition of Sr and Zr under molecular oxygen environment. The gas pressure is kept in the same range as STO growth, but the thin SZO with the thickness around 3 unit cells grown at low temperature shows to be highly amorphous with bright background and only very faint streaks, in contrast to STO buffer grown at the same temperature and thickness.

The initial stage of SZO growth is then optimized to achieve better epitaxial quality, and the results of varying substrate temperatures are shown in the Figure 6.9. Due to the large mismatch between SZO and Si, the deposition at low

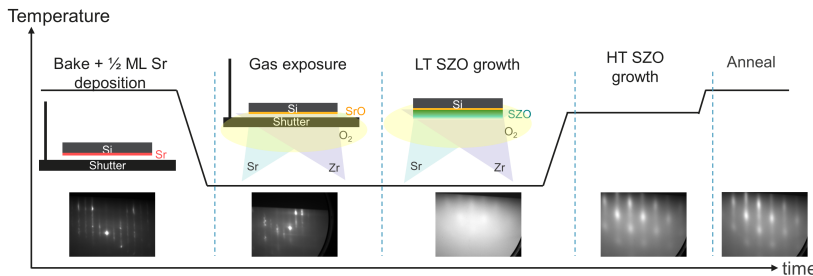


Figure 6.8: Deposition procedure for SZO grown on Si(001) substrate. The steps of Sr-Si template formation are similar with the STO / Si(001) epitaxy. Two steps are used for SZO growth, and a high temperature annealing after the growth is applied to further improve film crystallinity.

temperature (LT) is highly amorphous even after optimization, and it requires higher temperature annealing to recrystallize the SZO lattice. The temperature variations at the initial stage of growth show to impact recrystallization behavior, and the optimal growth temperature for SZO is around 400 °C. After a recrystallization step at 650 °C in UHV of $\sim 5 \times 10^{-8}$ Torr, the SZO is grown at this temperature for another 15 nm, and the final RHEED images show even more distinct differences. The darker background of the 400 °C condition suggests the film crystallinity is better with less diffused scattering from random atomic arrangement. The crystallinity can be further improved by annealing the SZO layer up to 750 °C after the epitaxy in UHV.

The XRD comparisons between SZO and STO layers with identical thicknesses are shown in the Figure 6.10. For the (002) peak from ω -2θ scan, the SZO shows smaller 2θ position, which indicates a larger lattice parameter compared with STO. The extracted lattice parameter is 4.12 Å, which is in perfect agreement with the theoretical value of 4.13 Å, indicating the SZO film is fully relaxed after the epitaxy and annealing. The highly amorphous RHEED image at the initial stage shows large impact on the crystallinity. As shown in the Fig. 6.10(b), the FWHM of SZO(002) peak is much larger than STO(002). The variation in crystallinity is also clearly highlighted by the lower intensity of the (002) reflection. With the same thickness and measurement parameters, the smaller peak intensity suggests the diffraction from crystalline phases is strongly reduced. This difference in crystallinity between the same thickness SZO and STO are resulted from the much larger lattice mismatch between the SZO film and the Si substrate. With large mismatch of ~7.5 %, the epitaxial growth becomes difficult, and more defects inside the film are expected.

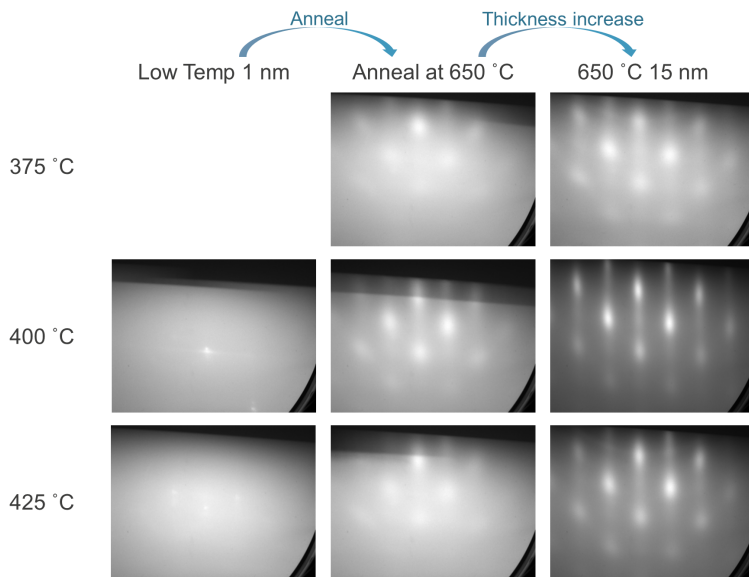


Figure 6.9: RHEED evolution along [100]SZO of the SZO films grown on Si with different substrate temperatures.

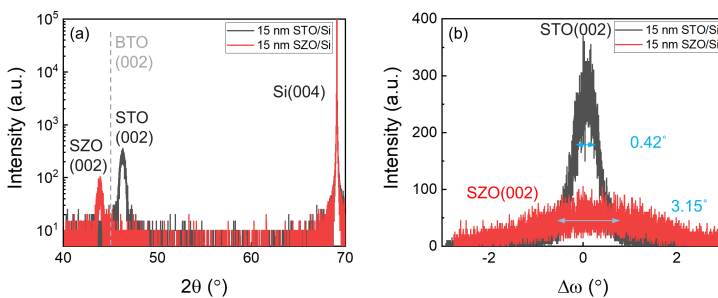


Figure 6.10: XRD patterns comparison of SZO and STO grown on Si with the same thickness. (a) out-of-plane ω - 2θ scan and (b) ω -scan of the (002) peak.

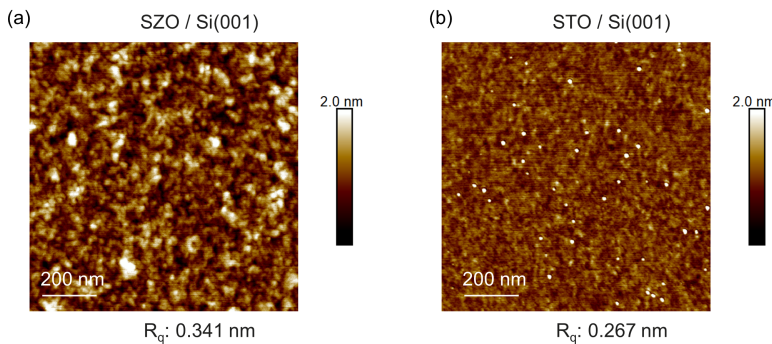


Figure 6.11: AFM comparison of (a) SZO and (b) STO grown on Si with the same thickness.

The surface roughness of SZO and STO is compared in Figure 6.11. The SZO is rougher than STO, with the roughness of 0.34 nm for the 15-nm thick film. For the STO film, the small spots observed on the surface is resulted from Sr-rich phase due to slightly off-stoichiometric composition.

6.2.2 SrZrO₃ on Ge / Si(001) Epitaxy

The large lattice mismatch between SZO and Si increases the difficulty in obtaining high quality epitaxial SZO films, thus another option of using Ge instead of Si is proposed. The change of substrate can reduce the lattice mismatch amount from 7.5 % to 3 %, which should largely help in the growth process. In this study, the change of substrate material is implemented by growing a thick 1 μm Ge layer on Si by CVD as the starting substrate for SZO epitaxy. The Ge grown by CVD is done with Imec standard epitaxy process, with GeH₄ vapor being used and the substrate at elevated temperature to form the epitaxial layer. A high temperature annealing ($\sim 850^\circ\text{C}$) after the Ge growth is carried out to reduce the defect density. The detailed growth procedure and the subsequent material analyses are reported elsewhere[216].

The basic procedure for SZO / Ge / Si epitaxy is the same than the growth on Si substrate, starting with HF cleaning to remove impurities and the subsequent high temperature bake to remove the native oxide, resulting in a (2 \times 1) surface reconstruction of Ge(001). Similar to STO epitaxy, the substrate temperature for SZO / Ge / Si epitaxy is first optimized, and the RHEED images are shown in Figure 6.12. Prior to the growth, 1/2 ML of Sr is introduced to form the

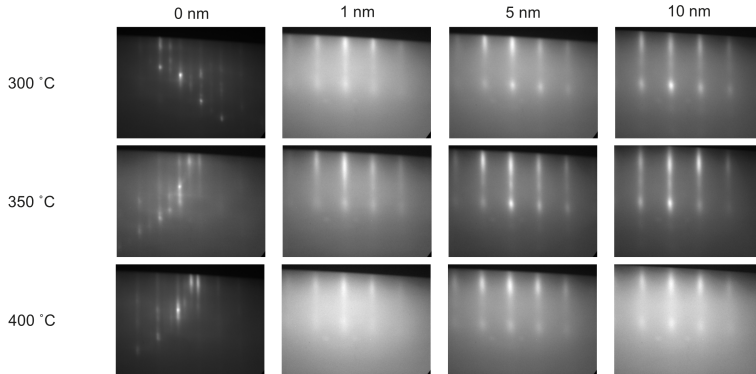


Figure 6.12: RHEED evolution along $[110]_{\text{SZO}}$ of SZO epitaxy on Ge / Si(001) as a function of substrate temperature.

Zintl template with Sr atoms sat in between Ge dimers. As in the STO epitaxy on Si, the clear (2×1) reconstruction prior to the growth is the result of clean surface with the coverage of $1/2$ ML Sr, showing the substrate is ready for the subsequent growth. By varying the growth temperature, the RHEED images show obvious differences in background intensity, with 350 °C possessing the maximum contrast. These differences are already appearing after 1 nm growth, and maintained as the thickness increases. The RHEED variations are similar to the STO / Si epitaxy, showing the optimal temperature is ~ 350 °C. Outside this temperature range, thicker interface would be formed, resulting in worse crystallinity and more diffused scattering in the RHEED images.

The XRD comparison for SZO with different substrate temperatures is presented in Figure 6.13. The lattice parameter calculated from SZO(002) peak is 4.14 Å for all the SZO films independent from the growth temperatures. For the FWHM of the ω -scans from the SZO(002) reflection, the trend is following the RHEED analysis, with the buffer grown at 350 °C showing the smallest value of 0.85° . In Fig. 6.13(b), the high temperature shows larger impact on the crystallinity as the FWHM increases rapidly when the temperature changes to from 350 °C to 380 °C, which is also observed on the RHEED images in Fig. 6.12. For the 400 °C sample, the RHEED shows obvious degradation after 5 nm, while the streaks of 300 °C sample maintain visible as the growth continues. Compared with STO / Si, the optimal temperature range is smaller for SZO / Ge / Si(001) epitaxy, which can be due to larger oxidation energy differences between Sr to Zr than Sr to Ti[139]. With SZO, it requires more precise temperature control for both elements to be properly oxidized. Nevertheless, the mismatch of SZO /

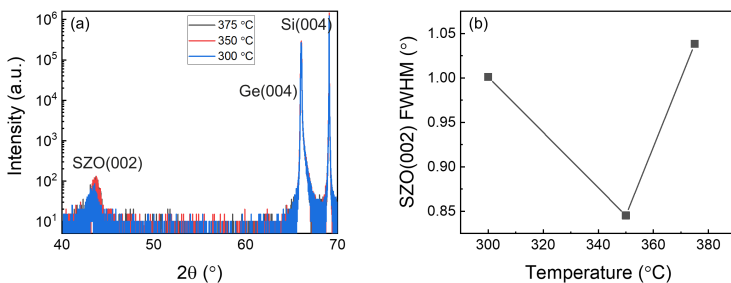


Figure 6.13: Different temperatures SZO / Ge / Si(001) XRD results of (a) symmetric ω - 2θ scan and (b) SZO(002) FWHM comparison from ω -scan.

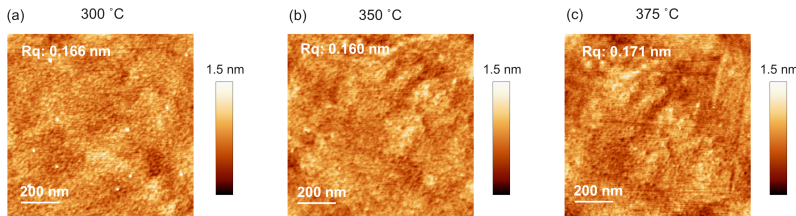


Figure 6.14: AFM results of 10-nm SZO grown on the Ge / Si(001) substrate using (a) 300 °C (b) 350 °C and (c) 375 °C growth temperature.

Ge / Si is still smaller than the SZO / Si system, which is immediately reflected on the RHEED pattern as clear diffraction streaks could be obtained at low temperature without further annealing step in UHV.

The surface roughness is also examined by AFM with the results shown in Figure 6.14. The surface of SZO layers is smooth, with all the roughness smaller than 0.2 nm even with different growth temperatures, and the 350 °C sample shows the flattest surface of only 0.16 nm in roughness. The flat surface is beneficial for the subsequent BTO epitaxial growth.

To further reduce the XRD peak FWHM, a 580 °C annealing in the MBE chamber right after the deposition is performed, and the XRD results as compared to the same thickness of STO / Si(001) are shown in Figure 6.15. The out-of-plane lattice parameter for SZO is 4.15 Å, which is much larger than the 3.93 Å of the same thickness STO. For the crystallinity, the SZO grown on

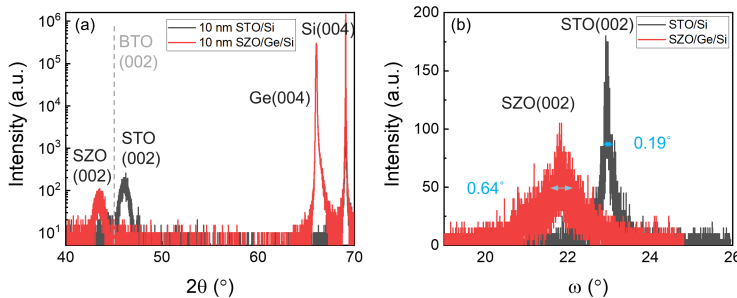


Figure 6.15: XRD results comparison between the same thickness STO / Si and SZO / Ge / Si of (a) symmetric ω - 2θ scan and (b) ω -scan around (002) peak.

Ge after annealing shows improvement with the FWHM of the (002) reflection reduced down to 0.64° . However, the FWHM is still larger than the STO / Si system, which can reach $\sim 0.2^\circ$ with careful stoichiometry and interface control, suggesting the SZO epitaxial procedure needs further optimization to obtain better control of the quality.

The optical properties of SZO film are summarized in Figure 6.16. As shown in Fig. 6.16(a), the refractive index of 10 nm SZO is smaller than theoretical bulk values, which could be contributed to the small thickness of the SZO layer as already discussed in the chapter 3. The bandgap is also extracted from absorption coefficient as shown in Fig. 6.16(b). The extracted bandgap from the measurement is of 5.6 eV, which matches perfectly with the previously reported values[213, 217].

6.3 BaTiO₃ Orientation Control Using Alternative SrZrO₃ Buffer

After the optimization of SZO epitaxy on both Si(001) and Ge / Si(001) substrates with good crystallinity and flat surface, the next step is to grow BTO in order to obtain a-oriented phase on this larger lattice parameter buffer layer. The BTO growth is performed by MBE technique using the same conditions previously described in the chapter 4, with the growth rate kept small and the temperature gradient applied on the Ba source to maintain good epitaxial characteristics and low defectivity. A 100-nm-thick BTO layer is grown on

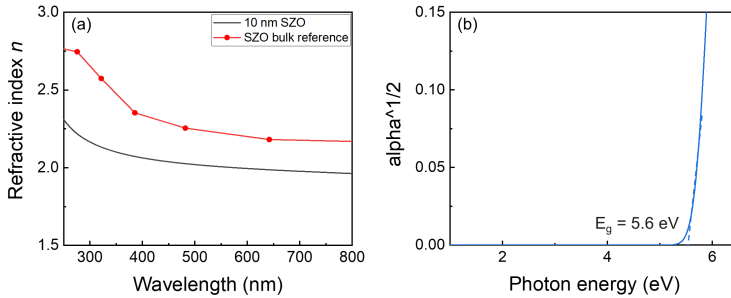


Figure 6.16: (a) Refractive index and (b) absorption coefficient of 10 nm epitaxial SZO. The reference values are taken from Ref.[218].

both SZO / Si(001) and SZO / Ge / Si(001) heterostructures, and the XRD comparison results, including the BTO grown on STO / Si, are summarized in Figure 6.17. As shown in Fig. 6.17(a), the BTO peak position using SZO as buffer layer is at higher angle and closer to the theoretical BTO(200) peak position compared with the BTO layer grown on STO buffer. The calculated out-of-plane lattice parameter of BTO using SZO is $\sim 3.99 \text{ \AA}$, while the film on STO shows to be $\sim 4.02 \text{ \AA}$. This difference is as expected, and it shows the strain is completely reversed by using alternative buffer layers with lattice parameters larger than the BTO one. However, since the STO buffer shows smaller FWHM value compared with SZO, obvious crystallinity differences of the BTO are observed as illustrated in Fig. 6.17(b). The BTO grown on STO buffer shows to have the smallest FWHM from the BTO(002) Bragg reflections with 0.39° , BTO on SZO / Ge / Si(001) presents a FWHM of 0.91° , while the BTO on SZO / Si shows the worst crystallinity with a FWHM value of 1.49° . This trend matches with the buffer crystallinity quality, indicating the defects from buffer layer will impact the subsequent BTO epitaxy.

The in-plane lattice parameters are calculated from asymmetric scan of BTO(202) peak, and the results are shown in Figure 6.18. From the BTO(202) peak, the in-plane lattice parameter are calculated based on the Equation 2.4. After obtaining the d_{202} from XRD measurement, the in-plane lattice parameter can be calculated with the input from out-of-plane lattice parameter c . The lattice parameter comparisons are summarized in Fig. 6.18(b), which shows the BTO / STO has c/a ratio larger than 1, while the BTO using SZO as buffer presents a ratio below unity, indicating an a -oriented BTO layer. These results confirm the BTO orientation can be engineered by using different buffer layers with correct lattice parameters.

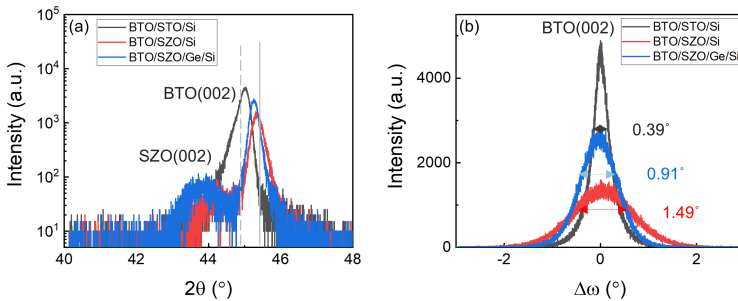


Figure 6.17: XRD comparison between 100-nm BTO films using different buffers and substrates. (a) BTO(002) ω - 2θ scan and (b) BTO(002) ω -scan. The dashed line in (a) represents the theoretical BTO(002) peak position, while the solid line shows the BTO(002) peak position.

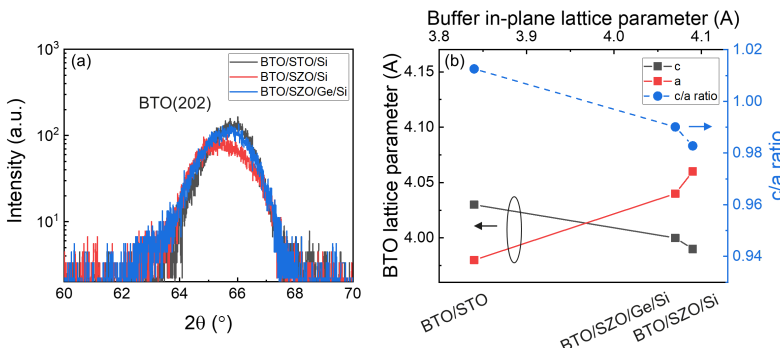


Figure 6.18: Comparison of (a) BTO(202) peak and (b) out-of-plane and in-plane lattice parameters of BTO using different buffer layers and substrates.

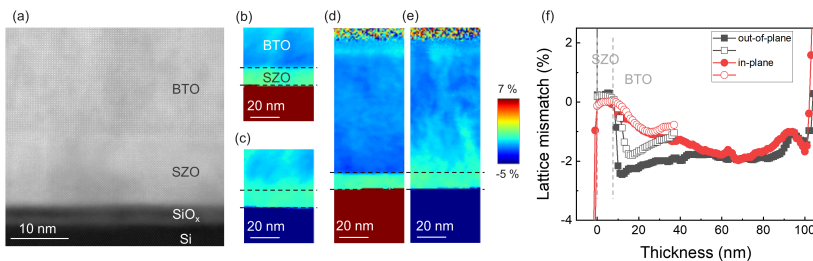


Figure 6.19: (a) BTO / SZO / Si HAADF image. (b)-(e) are NBD mapping results of (b) 25-nm BTO out-of-plane (c) 25-nm BTO in-plane (d) 100-nm BTO out-of-plane and (e) 100-nm BTO in in-plane direction. (f) is the NBD profile in both directions with white symbols from 25 nm BTO and solid symbols from 100 nm BTO.

The epitaxial BTO is further analyzed with STEM and NBD analyses, and the results of BTO / SZO / Si film are shown in Figure 6.19. As shown in Fig. 6.19(a), the BTO is epitaxially grown on SZO buffer layer, with well-aligned atoms clearly being observed. For the detailed lattice parameter change, NBD mappings of both 25-nm and 100-nm BTO films are shown in Fig. 6.19(b)-(e) using SZO as reference for lattice parameter comparisons. In Fig. 6.19(b) and (c), the BTO lattice parameter in out-of-plane direction shows to be smaller than SZO from the beginning of the growth, while in the in-plane direction, the lattice parameter is the same than SZO. However, as we move away from the BTO / SZO interface, the in-plane lattice parameter decreases rapidly, suggesting the tensile strain is fast relaxed with increased thickness. The same relaxation happens in the 100-nm BTO, with more obvious gradient toward the surface in the in-plane direction as in Fig. 6.19(e). The lattice parameter profiles are compared in Fig. 6.19(f), which shows the 100-nm BTO is more thoroughly relaxed, with the lattice parameters reaching the same value after 50 nm of BTO thickness. As clearly depicted, the BTO in-plane lattice parameter is larger than the out-of-plane value, showing the a-BTO can be indeed obtained by changing the buffer layer. However, the tensile strain from SZO buffer layer is fast relaxed, which is linked to the higher defect densities in both SZO and BTO layers. In order to obtain strained a-BTO, the epitaxial quality improvement is needed.

The BTO on Ge / Si(001) is also analyzed by STEM and NBD, and the results can be compared with BTO / SZO / Si(001). The same sets of results are shown in Figure 6.20. The HAADF image in Fig. 6.20(a) shows that the BTO and SZO layers are epitaxially grown on the 1- μ m Ge substrate, with smooth and

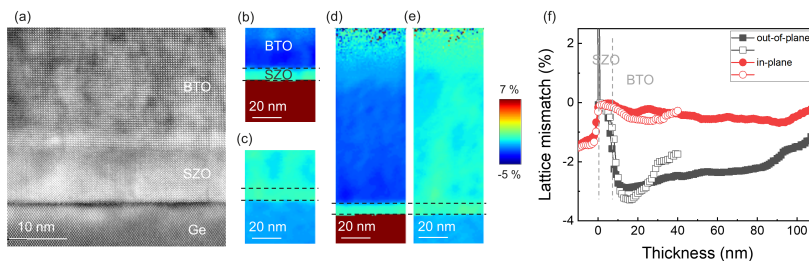


Figure 6.20: (a) BTO / SZO / Ge / Si HAADF image. (b)-(e) are NBD mapping results of (b) 25-nm BTO out-of-plane (c) 25-nm BTO in-plane (d) 100-nm BTO out-of-plane and (e) 100-nm BTO in in-plane direction. (f) is the NBD profile in both directions with white symbols from 25 nm BTO and solid symbols from 100 nm BTO.

sharp interfaces. Compared to the BTO / SZO / Si stack, the interface between SZO and Ge is very abrupt and coherent without the appearance of amorphous sub-oxides. The same NBD analysis is implemented on 25-nm and 100-nm BTO grown on SZO / Ge / Si(001) with the mapping results shown in Fig. 6.20(b)-(e). Like the BTO / SZO / Si sample, the BTO grown on SZO / Ge / Si(001) also possesses smaller out-of-plane lattice parameter as depicted in both Figures 6.20(b) and (d). However, different from BTO / SZO / Si(001), the in-plane lattice parameter shows only little relaxation with no obvious gradient observed in the mapping. Furthermore, the tensile strain is preserved even with the increase of BTO thickness as shown in Fig. 6.20(e). Due to better crystallinity of the SZO and BTO layers, the strain is less relaxed, resulting in a strained 100-nm BTO in a-orientation. The detailed profile is shown in Fig. 6.20(f), which clearly illustrates that the in-plane lattice parameter is larger than the out-of-plane lattice parameter for both 25-nm and 100-nm BTO, with only slight relaxation being observed.

The optical properties of BTO grown on SZO buffer are also investigated, and the results are shown in Figure 6.21. For the refractive index, the BTO grown on SZO shows smaller n values even with the thickness increased up to 100 nm. On the contrary, the BTO layer using STO as buffer layer shows identical values as the bulk BTO, thus the thickness effect should be excluded. As discussed in the chapter 4, the crystal imperfections, including stoichiometry variations and defects, will affect the refractive index n value. Based on the XRD results in Fig. 6.17(b), the decrease of refractive index using SZO buffer is attributed to the worse crystallinity compared with BTO grown on STO / Si(001). For the absorption coefficient in Fig. 6.21(b), the extracted bandgap is 3.4 eV, which is

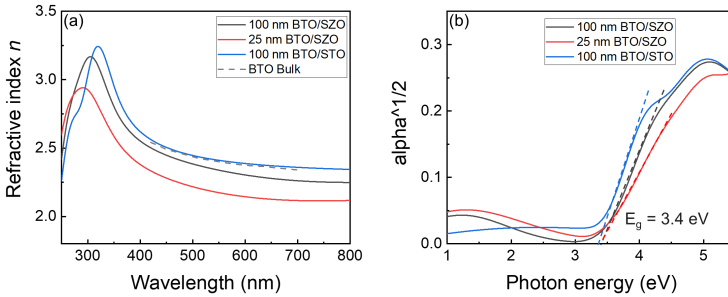


Figure 6.21: Optical indices comparisons of BTO with different buffers of (a) refractive index n and (b) absorption coefficient α as a function of incident energy. The BTO bulk refractive index are adapted from Ref.[151] and [152].

very close to the 3.3 eV bandgap value of BTO grown on STO / Si template. The small deviation from bulk characteristics suggests the BTO grown on SZO still requires some improvements in order to achieve comparable quality with the well-studied BTO / STO stacking.

6.4 Conclusion

To control the BTO orientation with elongated axis lying along the in-plane direction, a new buffer layer with larger lattice parameter is proposed. Among different candidates, the SZO is chosen due to its similar lattice mismatch amount compared to BTO / STO. In this chapter, the SZO epitaxy is investigated on both Si and Ge substrates, showing a much-improved crystallinity when growing on Ge / Si(001) due to reduced lattice mismatch. With growth temperature optimization and Sr/Zr stoichiometry control, the smallest FWHM of SZO(002) peak reaches 0.64° and the surface roughness is only ~ 0.16 nm.

The BTO grown on this epitaxial SZO buffer layer shows to change the orientation to a-BTO as expected. From both XRD and NBD analyses, the in-plane lattice parameter of BTO is indeed larger than the out-of-plane lattice parameter. Furthermore, the BTO / SZO / Ge / Si(001) shows to preserve the tensile strain after 100-nm growth, further confirming the feasibility of using alternative buffers to control domain orientations in BTO thin films. However, the strained a-BTO lacks the Pockels measurement to compare with the BTO grown on STO / Si(001), hence the correlation between physical properties

and Pockels coefficient cannot be further confirmed. Finally, the SZO-buffered samples still show deviations in refractive index values compared to the bulk reference, suggesting the optimization is still needed for the SZO epitaxy.

Chapter 7

Conclusion and Outlook

7.1 Conclusion

The materials demonstrated to exhibit a large Pockels effect allow one to manipulate the refractive index with better EO efficiency, making such material like the functional perovskite oxide BaTiO₃ attracting great attention due to its large theoretical Pockels coefficient and potential for monolithic integration on large scale substrates via epitaxy. In this thesis, a thin STO layer is first grown directly on Si(001) as a buffer layer for the subsequent growth of a BTO active layer. It is demonstrated that the substrate temperature and oxygen exposure largely affect the STO stoichiometry and crystallinity. With oxygen over-exposure, the Si surface is immediately oxidized, forming a thin amorphous SiO_x layer that prevents the epitaxial growth of STO. Furthermore, the Sr/Ti ratio also rises rapidly as the oxygen exposure increases, further hindering the STO epitaxy. Compared to Sr, the Ti is more easily oxidized under the same oxygen conditions. Thus, as the oxygen is largely introduced, the TiO_x is more easily formed and Ti is less incorporated into the STO layer, resulting in a Sr-rich film in the end. The optical losses are crucial in photonic applications, and the ultra-thin STO films show no absorption in the visible wavelength range. As for the change in the ultra-violet (UV) range, it is related to the material bandgap, which shows to be largely affected by film stoichiometry. With proper control of the applied oxygen amount, STO can be epitaxially grown on Si(001) with a well-defined and coherent interface being attained.

While the interface requires optimized exposure of oxygen, the active BTO layer needs a high oxygen pressure during the growth to improve the dielectric and

optical properties. However, as oxygen is introduced in the MBE chamber, the metallic sources are also oxidized, which results in a decrease of the effective atomic fluxes reaching the sample surface aiming to grow thick oxide films ($> \sim 30$ nm). The in-situ oxidation of the metallic sources is studied in detail by using a Sr flux from the effusion cell, and it shows that the elemental partial pressure is largely decreased under oxygen ambient. However, above a certain transition temperature of the source, the partial pressure drop is negligible. The decrease in partial pressure results in the formation of an oxide layer at the metal surface, but at higher temperature, the oxidation becomes ineffective due to the limited amount of oxygen in UHV. As a proof of concept, a thick STO layer with high Sr cell temperature is grown, and no additional Ti-rich reconstruction along the [100]STO azimuthal direction is observed by RHEED. This transition temperature can be used as a measure to counteract the flux loss due to source oxidation.

The BTO grown by MBE also suffers from the source oxidation effect, with the Ba source being oxidized and the Ba/Ti ratio kept decreasing with increasing thickness. However, as we increase the Ba temperature to values higher than the transition temperature, the growth rate also increases, which degrades the film quality. Thus, other than increasing the Ba cell temperature to counteract source oxidation effect, the direct temperature gradient applied to the Ba source is also investigated. By gradually increasing the Ba temperature, the Ba loss is compensated, and a flat Ba profile along the BTO thickness is measured by RBS. The stoichiometry variation of the BTO films much affects the crystallinity and strain relaxation, with the stoichiometric BTO showing the best crystallinity because, without relaxation, the residual strain allows maintaining c-orientation even for thicknesses larger than 100 nm. On the basis of previous works from Imec, we demonstrate a high-quality BTO film with the improved XRD FWHM value to be smaller than 0.4° . Moreover, the long-existed stoichiometry instability is also studied in detail, and the BTO films with more consistent quality can be expected. Finally, the EO measurements of the BTO films shows that the Pockels coefficient is strongly related to the stoichiometry and, consequently, to the film crystallinity. Compared to the Pockels coefficient reported by Abel et al., the value is still not as large for our 100-nm BTO films. Nevertheless, the measured 200 pm/V can result in the change of refractive index (Δn) of ~ 0.05 , which will already be effective for the VH application.

Next to the MBE approach, the PLD technique is also explored for BTO growth since it possesses much higher base pressure and allows an easier control of the stoichiometry. With optimized conditions, the BTO is successfully epitaxially grown on the MBE-STO / Si(001) pseudo-substrate after the vacuum break from MBE chamber. Moreover, the BTO strain relaxation is shown to be strongly correlated to the oxygen chamber pressure. With higher oxygen pressure, the

strain is faster relaxed, hence the BTO polarization evolves rapidly towards the a-orientation. Different physical characterizations, including PFM and C-V analyses, all confirm the domain orientation shift observed by XRD. From NBD mapping results, the a-oriented BTO shows smaller domain size, suggesting the compressive strain is relaxed through the formation of domain boundaries.

For BTO grown on STO, due to the compressive strain from buffer and substrate, the a-oriented BTO can only be obtained with the strain being relaxed. To relax the strain, more defects such as dislocations and domain boundaries will be created, inevitably degrading the film quality. Thus, in the final part of the thesis, alternative buffers and/or substrates are proposed in order to drive the strain towards tensile direction in the final part of the thesis. SrZrO_3 is chosen as the candidate of choice since it creates a similar lattice mismatch amount with BTO compared to the STO buffer layer, but no with opposite strain direction as the SrZrO_3 lattice parameter is larger. However, as the lattice mismatch between Si and SZO is too large to obtain a good epitaxial oxide film, the substrate is switched to Ge. With optimized growth condition, a 10-nm SZO buffer layer can be epitaxially grown on a Ge / Si(001) substrate with the SZO(002) XRD peak FWHM reaching $\sim 0.68^\circ$. Finally, the BTO films grown on a SZO buffer layer show, as expected, to have a larger in-plane lattice parameter. The BTO / SZO / Ge / Si is analyzed by NBD, which shows that the tensile strain is not relaxed after 100-nm growth and proves that the domain orientation can be controlled by selecting the right buffer to induce the desired strain in the subsequent BTO active layer. The tensile strained a-oriented BTO is expected to have a large Pockels coefficient, but will still require more measurements to confirm the expectation.

7.2 Outlook

7.2.1 Effusion cell control with feedback loop

Applying a Ba source temperature gradient can effectively compensate the Ba loss due to oxidation, but it is also found that an inappropriate setting can result in a dramatic stoichiometry shift from Ti-rich to Ba-rich BTO. Due to the lack of feedback loop control of effusion cells, the stoichiometry instability becomes the bottle neck of obtaining BTO films with consistent quality. The XBS mass spectrometer is installed in front of the effusion cells, thus the partial pressure from metallic sources can be measured. However, there is no feedback loop to control the pressure as is the case in Ti e-beam evaporator. With an upgrade of the MBE electronic system, a feedback loop control on both Ba and Sr could be setup. This should solve the flux loss caused by the source oxidation

effect and enable to keep the source partial pressure stable during the growth, thus solving the stoichiometry instability and enabling one to fully control the film quality.

7.2.2 Alternative buffer optimization and extension

In the last chapter, the strain control using SZO shows very promising results, with an a-BTO film preserving tensile strain even after 100-nm growth on a Ge / Si(001) substrate. Compared with the already well-studied STO / Si system, the SZO / Ge epitaxy is relatively new and requires more studies to achieve better quality. In this thesis, the SZO epitaxy uses a similar process as applied for STO growth, with only some optimization of the substrate temperature. From the interface study of STO / Si, it is found that the oxygen exposure amount plays an important role in the epitaxy process, which is not studied in the case of SZO growth. With more thorough study, it is expected that the quality of the SZO epitaxial layer may be further improved.

Since the SZO buffer shows the ability to control strain in the BTO layer, other perovskite oxides with larger lattice parameter compared to BTO should also be investigated. As introduced in chapter 6, the SrHfO₃ was reported to be epitaxially grown on Si, which could be a promising candidate as well to create tensile strain in BTO[210].

7.2.3 Single domain orientation with off-cut wafer

For a-BTO, the elongated axis is lying in in-plane direction, which can be either parallel to the *x*- or *y*-axis, resulting in two possible domain orientations perpendicular to each other. When poling the BTO dipoles, the domain orientation perpendicular to the poling electric field will not be contributing to the change in refractive index, which reduces the Pockels effect. A Si(001) wafer with small off-cut angle is reported to possess only one Si dimer orientation after annealing, which aligns parallel to the step-edge due to surface energy differences[219]. Thus, when growing BTO using such off-cut wafer, the BTO domain orientation is also expected to align with the dimer orientation, eliminating the domains that are perpendicular to the step-edge. During the current work, some preliminary research has already been executed, using a ~6° off-cut angle Si wafer annealed to higher than 900 °C in order to align the dimers and form the double-step. The RHEED images taken for off-axis and on-axis wafer are shown in Figure 7.1. For the sample with double step, the ×2 reconstruction can only be observed along the [1̄10] direction, while the RHEED rotated 90° to [11̄0] shows no additional lines between the main

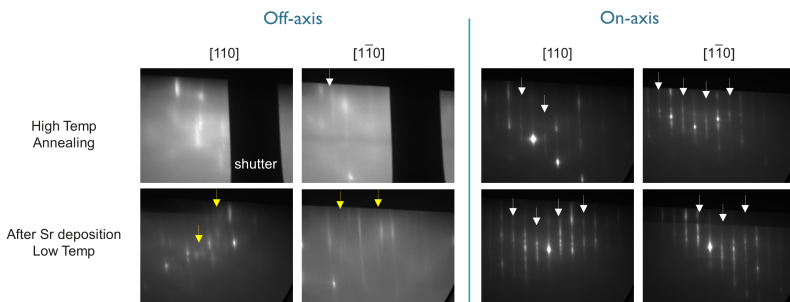


Figure 7.1: RHEED images along [110] and [1 $\bar{1}$ 0] of both off-axis and on-axis wafers. The white arrows indicate signals from $\times 2$ surface reconstruction, while the yellow arrows mark the signals from reconstruction that shows the Sr coverage is less than 1/2 ML.

diffraction streaks. However, based on the RHEED monitor results, the double-step changes back to single-step after the substrate is cooled down to ~ 500 °C. Even with Sr introduced at 850 °C, the single-step RHEED is still observed, and the coverage is also less than 1/2 ML. Based on these results, the annealing and Sr coverage procedure should be further studied prior to the STO and BTO epitaxy growth.

7.2.4 Wafer Bonding Processes for Video Holography Device

As shown in Figure 1.5, the video holography device consists of two parts: BaTiO₃ waveguide and 10-nm node MOSFET with transparent interconnect. In order to combine these two parts, an oxide-oxide bonding process is needed. For the BTO films, after bonded with another wafer, the substrate and the buffer layer for growing BTO will need to be removed by the backside chemical-mechanical polishing (CMP) process. After the CMP process, not only the bonding interface stability needs to be controlled, but also the BTO characteristics required to keep unchanged. The study on wafer bonding process will be started first with the usage of small BTO coupons before proceeding to the usage of the whole 8-inch wafer.

Appendix A

Appendix: Exploitation Plan

Video Holography ERC Project

This work is an integral part of the ERC project “Video Holography” as it paves the way to enable the control of an electro-optic waveguide at the 100 nm scale. For the Video holography application, the BTO thin film is used as a waveguide with pillar meta-material on the bottom acting as the source of electric field. On top of the BTO waveguide is where the evanescent waves of the light come out. By applying electric field to BTO waveguide, the refractive indices are modified, and the light path propagating inside the waveguide is affected. We can decide the light path inside the waveguide, thus creating a 3D image on top of the whole structure. The targeted structure is shown in the Figure A1.

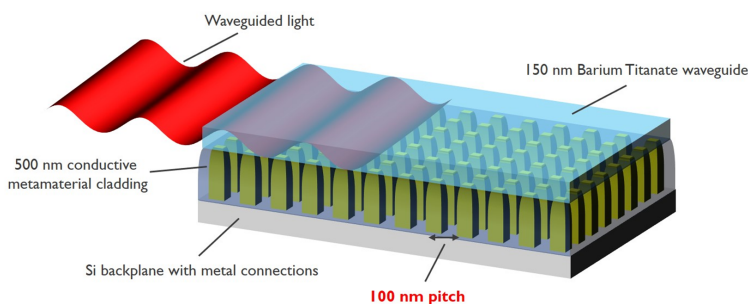


Figure A.1: Targeted structure for video holography project.

Table A.1: Comparison of static and video holography applications

	Security	Display	Entertainment
Static holography	Currency notes	Art works	x
Video holography	Optical information Encryption	3D display	Movies

Potential Outcomes

The video holography project aims to develop a device that can create full-color 3D image based on the advanced FinFET CMOS technology. With BTO waveguide integrated on transparent meta-material pillars, the targeted outcome is a display that can generate 3D image with the update frequency in video framerate.

Target Market

The video holography device contains CMOS from standard semiconductor processing and the subsequent meta-material as well as BTO waveguide are all integrated on top of the CMOS, thus the final structure will be a chip which can be integrated to various display devices, such as projectors and cellphones. Moreover, the static holography is a well-known technology that is difficult to replicate, and is already widely applied on security applications such as bank notes. For the video holography, the fast-updating speed and high resolution can further secure the stored information. Finally, the video holography can be used in entertainment business such as movie industry, and the scenes in sci-fi movies can be created physically without the need of post-production. By using this technology, the video holography with high resolution can be adapted easily and integrated on the already existed equipment. The comparisons between static and video holography applications are listed in the Table A.1.

Operations

The project involves several processes executed at imec, including BTO growth and meta-material deposition and planarization. In imec, the exploitation for video holography application is an integral part of the business plan of a spin-off company.

Bibliography

- [1] D. Gabor, “A new microscopic principle,” *Nature*, vol. 161, pp. 777–778, 1948. [Online]. Available: <https://doi.org/10.1038/161777a0>
- [2] J. W. Goodman, “An introduction to the principles and applications of holography,” *Proceedings of the IEEE*, vol. 59, pp. 1292–1304, 1971. [Online]. Available: <https://doi.org/10.1109/PROC.1971.8405>
- [3] P.-A. Blanche, “Chapter 1 - Introduction to Holographic Principles,” in *Optical Holography: Materials, Theory and Applications*, P.-A. Blanche, Ed. Elsevier, 2020, pp. 1–39. [Online]. Available: <https://www.sciencedirect.com/science/article/pii/B9780128154670000013>
- [4] R. J. Collier, C. B. Burckhardt, and L. H. Lin, “Chapter 1 - Introduction to Basic Concepts,” in *Optical Holography*, R. J. Collier, C. B. Burckhardt, and L. H. Lin, Eds. Academic Press, 1971, pp. 1–34. [Online]. Available: <https://www.sciencedirect.com/science/article/pii/B9780121810504500068>
- [5] P. Marquet, C. Depeursinge, and P. Jourdain, “Cellular Dynamics Revealed by Digital Holographic Microscopy,” in *Reference Module in Neuroscience and Biobehavioral Psychology*. Elsevier, 2017. [Online]. Available: <https://www.sciencedirect.com/science/article/pii/B9780128093245024263>
- [6] P.-A. Blanche, “Chapter 2 - Holographic Recording Media and Devices,” in *Optical Holography: Materials, Theory and Applications*, P.-A. Blanche, Ed. Elsevier, 2020, pp. 41–60. [Online]. Available: <https://www.sciencedirect.com/science/article/pii/B9780128154670000025>
- [7] B. R. Brown and A. W. Lohmann, “Complex Spatial Filtering with Binary Masks,” *Appl. Opt.*, vol. 5, pp. 967–969, 6 1966. [Online]. Available: <http://opg.optica.org/ao/abstract.cfm?URI=ao-5-6-967>

- [8] H. Gao, Y. Wang, X. Fan, B. Jiao, T. Li, C. Shang, C. Zeng, L. Deng, W. Xiong, J. Xia, and M. Hong, “Dynamic 3D meta-holography in visible range with large frame number and high frame rate,” *Science Advances*, vol. 6, p. eaba8595, 8 2022, doi: 10.1126/sciadv.aba8595. [Online]. Available: <https://doi.org/10.1126/sciadv.aba8595>
- [9] M. L. Huebschman, B. Munjuluri, and H. R. Garner, “Dynamic holographic 3-D image projection,” *Opt. Express*, vol. 11, pp. 437–445, 3 2003. [Online]. Available: <http://opg.optica.org/oe/abstract.cfm?URI=oe-11-5-437>
- [10] L. J. Hornbeck, “Digital Light Processing for high-brightness high-resolution applications,” in *Projection Displays III*, M. H. Wu, Ed., vol. 3013, International Society for Optics and Photonics. SPIE, 1997, pp. 27 – 40. [Online]. Available: <https://doi.org/10.1117/12.273880>
- [11] G. Tricoles, “Computer generated holograms: an historical review,” *Appl. Opt.*, vol. 26, pp. 4351–4360, 10 1987. [Online]. Available: <http://opg.optica.org/ao/abstract.cfm?URI=ao-26-20-4351>
- [12] K. J. Miller, R. F. Haglund, and S. M. Weiss, “Optical phase change materials in integrated silicon photonic devices: review,” *Opt. Mater. Express*, vol. 8, pp. 2415–2429, 8 2018. [Online]. Available: <http://opg.optica.org/ome/abstract.cfm?URI=ome-8-8-2415>
- [13] M. Delaney, I. Zeimpekis, D. Lawson, D. W. Hewak, and O. L. Muskens, “A New Family of Ultralow Loss Reversible Phase-Change Materials for Photonic Integrated Circuits: Sb_2S_3 and Sb_2Se_3 ,” *Advanced Functional Materials*, vol. 30, p. 2002447, 9 2020, <https://doi.org/10.1002/adfm.202002447>. [Online]. Available: <https://doi.org/10.1002/adfm.202002447>
- [14] S. Cueff, J. John, Z. Zhang, J. Parra, J. Sun, R. Orobtchouk, S. Ramanathan, and P. Sanchis, “ VO_2 nanophotonics,” *APL Photonics*, vol. 5, p. 110901, 11 2020, doi: 10.1063/5.0028093. [Online]. Available: <https://doi.org/10.1063/5.0028093>
- [15] M. Wuttig and N. Yamada, “Phase-change materials for rewriteable data storage,” *Nature Materials*, vol. 6, pp. 824–832, 2007. [Online]. Available: <https://doi.org/10.1038/nmat2009>
- [16] C.-Y. Hwang, G. H. Kim, J.-H. Yang, C.-S. Hwang, S. M. Cho, W.-J. Lee, J.-E. Pi, J. H. Choi, K. Choi, H.-O. Kim, S.-Y. Lee, and Y.-H. Kim, “Rewritable full-color computer-generated holograms based on color-selective diffractive optical components including phase-change

- materials," *Nanoscale*, vol. 10, pp. 21 648–21 655, 2018. [Online]. Available: <http://dx.doi.org/10.1039/C8NR04471F>
- [17] S.-Y. Lee, Y.-H. Kim, S.-M. Cho, G. H. Kim, T.-Y. Kim, H. Ryu, H. N. Kim, H. B. Kang, C.-Y. Hwang, and C.-S. Hwang, "Holographic image generation with a thin-film resonance caused by chalcogenide phase-change material," *Scientific Reports*, vol. 7, p. 41152, 2017. [Online]. Available: <https://doi.org/10.1038/srep41152>
- [18] H. Y. Cheng, T. H. Hsu, S. Raoux, J. Y. Wu, P. Y. Du, M. Breitwisch, Y. Zhu, E. K. Lai, E. Joseph, S. Mittal, R. Cheek, A. Schrott, S. C. Lai, H. L. Lung, and C. Lam, "A high performance phase change memory with fast switching speed and high temperature retention by engineering the $\text{Ge}_x\text{Sb}_y\text{Te}_z$ phase change material," in *2011 International Electron Devices Meeting*, 2011, pp. 3.4.1–3.4.4. [Online]. Available: <https://doi.org/10.1109/IEDM.2011.6131481>
- [19] S.-M. Yoon, N.-Y. Lee, S.-O. Ryu, K.-J. Choi, Y. S. Park, S.-Y. Lee, B.-G. Yu, M.-J. Kang, S.-Y. Choi, and M. Wuttig, "Sb-Se-based phase-change memory device with lower power and higher speed operations," *IEEE Electron Device Letters*, vol. 27, pp. 445–447, 2006. [Online]. Available: <https://doi.org/10.1109/LED.2006.874130>
- [20] M. M. Howerton, R. P. Moeller, A. S. Greenblatt, and R. Krahenbuhl, "Fully packaged, broad-band LiNbO_3 modulator with low drive voltage," *IEEE Photonics Technology Letters*, vol. 12, pp. 792–794, 2000. [Online]. Available: <https://doi.org/10.1109/68.853502>
- [21] L. R. Dalton, P. Günter, M. Jazbinsek, O.-P. Kwon, and P. A. Sullivan, "Electro-optic effects," in *Organic Electro-Optics and Photonics: Molecules, Polymers, and Crystals*. Cambridge University Press, 2015, p. 28–39. [Online]. Available: <https://doi.org/10.1017/CBO9781139043885.003>
- [22] R. W. Boyd, "The Electrooptic and Photorefractive Effects," in *Nonlinear Optics*, R. W. Boyd, Ed. Academic Press, 2008, pp. 511–541. [Online]. Available: <http://www.sciencedirect.com/science/article/pii/B9780123694706000113>
- [23] T.-C. Poon and T. Kim, "Electro-optics," in *Engineering Optics with MATLAB ®*. WORLD SCIENTIFIC, 1 2017, pp. 254–300, doi:10.1142/9789813100022_0005. [Online]. Available: https://doi.org/10.1142/9789813100022_0005
- [24] R. W. Boyd, "Chapter 4 - The Intensity-Dependent Refractive Index," in *Nonlinear Optics*, R. W. Boyd, Ed. Academic Press, 2008, pp. 207–252.

- [Online]. Available: <https://www.sciencedirect.com/science/article/pii/B9780123694706000046>
- [25] H. Li, F. Zhou, X. Zhang, and W. Ji, “Picosecond Z-scan study of bound electronic Kerr effect in LiNbO_3 crystal associated with two-photon absorption,” *Applied Physics B*, vol. 64, pp. 659–662, 1997. [Online]. Available: <https://doi.org/10.1007/s003400050229>
- [26] R. A. Ganeev, I. A. Kulagin, A. I. Ryasnyansky, R. I. Tugushev, and T. Usmanov, “Characterization of nonlinear optical parameters of KDP, LiNbO_3 and BBO crystals,” *Optics Communications*, vol. 229, pp. 403–412, 2004. [Online]. Available: <https://www.sciencedirect.com/science/article/pii/S0030401803021801>
- [27] D. A. B. Miller, “Device Requirements for Optical Interconnects to Silicon Chips,” *Proceedings of the IEEE*, vol. 97, pp. 1166–1185, 2009. [Online]. Available: <https://doi.org/10.1109/JPROC.2009.2014298>
- [28] G. T. Reed and C. E. J. Png, “Silicon optical modulators,” *Materials Today*, vol. 8, pp. 40–50, 2005. [Online]. Available: <https://www.sciencedirect.com/science/article/pii/S1369702104006789>
- [29] P. Gunter, “Electro-optical effects in ferroelectrics,” *Ferroelectrics*, vol. 74, pp. 305–307, 8 1987, doi: 10.1080/00150198708201311. [Online]. Available: <https://doi.org/10.1080/00150198708201311>
- [30] S. Abel, T. Stöferle, C. Marchiori, D. Caimi, L. Czornomaz, M. Stuckelberger, M. Sousa, B. J. Offrein, and J. Fompeyrine, “A Hybrid Barium Titanate–Silicon Photonics Platform for Ultraefficient Electro-Optic Tuning,” *J. Lightwave Technol.*, vol. 34, pp. 1688–1693, 4 2016. [Online]. Available: <http://opg.optica.org/jlt/abstract.cfm?URI=jlt-34-8-1688>
- [31] <https://www.zurich.ibm.com/st/photonics/materials.html>.
- [32] M. Jazbinsek, L. Mutter, and P. Gunter, “Photonic Applications With the Organic Nonlinear Optical Crystal DAST,” *IEEE Journal of Selected Topics in Quantum Electronics*, vol. 14, pp. 1298–1311, 2008. [Online]. Available: <https://doi.org/10.1109/JSTQE.2008.921407>
- [33] C. Zhang, L. R. Dalton, M.-C. Oh, H. Zhang, and W. H. Steier, “Low $V\pi$ Electrooptic Modulators from CLD-1: Chromophore Design and Synthesis, Material Processing, and Characterization,” *Chemistry of Materials*, vol. 13, pp. 3043–3050, 9 2001, doi: 10.1021/cm010463j. [Online]. Available: <https://doi.org/10.1021/cm010463j>

- [34] P. Pretre, P. Kaatz, A. Bohren, P. Guenter, B. Zysset, M. Ahlheim, M. Staehelin, and F. Lehr, “Modified Polyimide Side-Chain Polymers for Electrooptics,” *Macromolecules*, vol. 27, pp. 5476–5486, 9 1994, doi: 10.1021/ma00097a030. [Online]. Available: <https://doi.org/10.1021/ma00097a030>
- [35] W. Guo, A. B. Posadas, and A. A. Demkov, “Epitaxial integration of BaTiO₃ on Si for electro-optic applications,” *Journal of Vacuum Science and Technology A*, vol. 39, p. 30804, 4 2021, doi: 10.1116/6.0000923. [Online]. Available: <https://doi.org/10.1116/6.0000923>
- [36] L. R. Dalton, P. A. Sullivan, and D. H. Bale, “Electric Field Poled Organic Electro-optic Materials: State of the Art and Future Prospects,” *Chemical Reviews*, vol. 110, pp. 25–55, 1 2010, doi: 10.1021/cr9000429. [Online]. Available: <https://doi.org/10.1021/cr9000429>
- [37] H. Xu, D. L. Elder, L. E. Johnson, Y. de Coene, S. R. Hammond, W. V. Ghinst, K. Clays, L. R. Dalton, and B. H. Robinson, “Electro-Optic Activity in Excess of 1000 pm V⁻¹ Achieved via Theory-Guided Organic Chromophore Design,” *Advanced Materials*, vol. 33, p. 2104174, 11 2021, <https://doi.org/10.1002/adma.202104174>. [Online]. Available: <https://doi.org/10.1002/adma.202104174>
- [38] S. Koeber, R. Palmer, M. Lauermann, W. Heni, D. L. Elder, D. Korn, M. Woessner, L. Alloatti, S. Koenig, P. C. Schindler, H. Yu, W. Bogaerts, L. R. Dalton, W. Freude, J. Leuthold, and C. Koos, “Femtojoule electro-optic modulation using a silicon–organic hybrid device,” *Light: Science and Applications*, vol. 4, pp. e255–e255, 2015. [Online]. Available: <https://doi.org/10.1038/lsa.2015.28>
- [39] C. Kieninger, Y. Kutuvantavida, D. L. Elder, S. Wolf, H. Zwickel, M. Blaicher, J. N. Kemal, M. Lauermann, S. Randel, W. Freude, L. R. Dalton, and C. Koos, “Ultra-high electro-optic activity demonstrated in a silicon-organic hybrid modulator,” *Optica*, vol. 5, pp. 739–748, 6 2018. [Online]. Available: <http://opg.optica.org/optica/abstract.cfm?URI=optica-5-6-739>
- [40] R. Palmer, S. Koeber, D. L. Elder, M. Woessner, W. Heni, D. Korn, M. Lauermann, W. Bogaerts, L. Dalton, W. Freude, J. Leuthold, and C. Koos, “High-Speed, Low Drive-Voltage Silicon-Organic Hybrid Modulator Based on a Binary-Chromophore Electro-Optic Material,” *Journal of Lightwave Technology*, vol. 32, pp. 2726–2734, 2014. [Online]. Available: <https://doi.org/10.1109/JLT.2014.2321498>

- [41] L. R. Dalton, P. Günter, M. Jazbinsek, O.-P. Kwon, and P. A. Sullivan, “Electrically poled organic materials and thermo-optic materials,” in *Organic Electro-Optics and Photonics: Molecules, Polymers, and Crystals*. Cambridge University Press, 2015, p. 118–174. [Online]. Available: <https://doi.org/10.1017/CBO9781139043885.007>
- [42] W. Heni, C. Haffner, D. L. Elder, A. F. Tillack, Y. Fedoryshyn, R. Cottier, Y. Salamin, C. Hoessbacher, U. Koch, B. Cheng, B. Robinson, L. R. Dalton, and J. Leuthold, “Nonlinearities of organic electro-optic materials in nanoscale slots and implications for the optimum modulator design,” *Opt. Express*, vol. 25, pp. 2627–2653, 2 2017. [Online]. Available: <http://opg.optica.org/oe/abstract.cfm?URI=oe-25-3-2627>
- [43] L. R. Dalton, P. Günter, M. Jazbinsek, O.-P. Kwon, and P. A. Sullivan, “Electro-optic effects,” in *Organic Electro-Optics and Photonics: Molecules, Polymers, and Crystals*, L. R. Dalton, M. Jazbinsek, O.-P. Kwon, P. Günter, and P. A. Sullivan, Eds. Cambridge University Press, 2015, pp. 28–39. [Online]. Available: <https://www.cambridge.org/core/books/organic-electrooptics-and-photonics/electrooptic-effects/9F0EC597B42C378B4D45EB3D2F6BED57>
- [44] D. Zhu, L. Shao, M. Yu, R. Cheng, B. Desiatov, C. J. Xin, Y. Hu, J. Holzgrafe, S. Ghosh, A. Shams-Ansari, E. Puma, N. Sinclair, C. Reimer, M. Zhang, and M. Lončar, “Integrated photonics on thin-film lithium niobate,” *Adv. Opt. Photon.*, vol. 13, pp. 242–352, 6 2021. [Online]. Available: <http://opg.optica.org/aop/abstract.cfm?URI=aop-13-2-242>
- [45] P. O. Weigel, J. Zhao, K. Fang, H. Al-Rubaye, D. Trotter, D. Hood, J. Mudrick, C. Dallo, A. T. Pomerene, A. L. Starbuck, C. T. DeRose, A. L. Lentine, G. Rebeiz, and S. Mookherjea, “Bonded thin film lithium niobate modulator on a silicon photonics platform exceeding 100 GHz 3-dB electrical modulation bandwidth,” *Opt. Express*, vol. 26, pp. 23 728–23 739, 9 2018. [Online]. Available: <http://opg.optica.org/oe/abstract.cfm?URI=oe-26-18-23728>
- [46] A. Boes, B. Corcoran, L. Chang, J. Bowers, and A. Mitchell, “Status and Potential of Lithium Niobate on Insulator (L NOI) for Photonic Integrated Circuits,” *Laser and Photonics Reviews*, vol. 12, p. 1700256, 4 2018, <https://doi.org/10.1002/lpor.201700256>. [Online]. Available: <https://doi.org/10.1002/lpor.201700256>
- [47] H. Hu, J. Yang, L. Gui, and W. Sohler, “Lithium niobate-on-insulator (L NOI): status and perspectives,” in *Silicon Photonics and Photonic Integrated Circuits III*, L. Vivien, S. K. Honkanen, L. Pavesi, and S. Pelli,

- Eds., vol. 8431, International Society for Optics and Photonics. SPIE, 5 2012, p. 84311D. [Online]. Available: <https://doi.org/10.1117/12.922401>
- [48] S. Abel, T. Stöferle, C. Marchiori, C. Rossel, M. D. Rossell, R. Erni, D. Caimi, M. Sousa, A. Chelnokov, B. J. Offrein, and J. Fompeyrine, “A strong electro-optically active lead-free ferroelectric integrated on silicon,” *Nature Communications*, vol. 4, p. 1671, 2013. [Online]. Available: <https://doi.org/10.1038/ncomms2695>
- [49] A. von Hippel, “Ferroelectricity, Domain Structure, and Phase Transitions of Barium Titanate,” *Reviews of Modern Physics*, vol. 22, pp. 221–237, 7 1950. [Online]. Available: <https://link.aps.org/doi/10.1103/RevModPhys.22.221>
- [50] H. D. Megaw, “Origin of ferroelectricity in barium titanate and other perovskite-type crystals,” *Acta Crystallographica*, vol. 5, pp. 739–749, 11 1952. [Online]. Available: <https://doi.org/10.1107/S0365110X52002069>
- [51] M. Acosta, N. Novak, V. Rojas, S. Patel, R. Vaish, J. Koruza, G. A. Rossetti, and J. Rödel, “BaTiO₃-based piezoelectrics: Fundamentals, current status, and perspectives,” *Applied Physics Reviews*, vol. 4, p. 41305, 12 2017, doi: 10.1063/1.4990046. [Online]. Available: <https://doi.org/10.1063/1.4990046>
- [52] D. Meier and S. M. Selbach, “Ferroelectric domain walls for nanotechnology,” *Nature Reviews Materials*, vol. 7, pp. 157–173, 2022. [Online]. Available: <https://doi.org/10.1038/s41578-021-00375-z>
- [53] A. Rosa, D. Tulli, P. Castera, A. M. Gutierrez, A. Griol, M. Baquero, B. Vilquin, F. Eltes, S. Abel, J. Fompeyrine, and P. Sanchis, “Barium titanate (BaTiO₃) RF characterization for application in electro-optic modulators,” *Optical Materials Express*, vol. 7, pp. 4328–4336, 2017. [Online]. Available: <http://opg.optica.org/ome/abstract.cfm?URI=ome-7-12-4328>
- [54] W. Kinase, M. Yoshikawa, and N. Ohnishi, “Quantum theory of electrooptic effect in BaTiO₃,” *Ferroelectrics*, vol. 67, pp. 159–168, 3 1986, doi: 10.1080/00150198608245018. [Online]. Available: <https://doi.org/10.1080/00150198608245018>
- [55] D. Khatib, B. Jannot, and P. Jullien, “Theory of electro-optic effect in the tetragonal phase of BaTiO₃,” *Ferroelectrics Letters Section*, vol. 15, pp. 1–7, 1 1993, doi: 10.1080/07315179308203354. [Online]. Available: <https://doi.org/10.1080/07315179308203354>

- [56] I. P. Kaminow and W. D. Johnston, "Quantitative Determination of Sources of the Electro-Optic Effect in LiNbO₃ and LiTaO₃," *Phys. Rev.*, vol. 160, pp. 519–522, Aug 1967. [Online]. Available: <https://link.aps.org/doi/10.1103/PhysRev.160.519>
- [57] T. Paoletta and A. A. Demkov, "Pockels effect in low-temperature rhombohedral BaTiO₃," *Physical Review B*, vol. 103, p. 14303, 1 2021. [Online]. Available: <https://link.aps.org/doi/10.1103/PhysRevB.103.014303>
- [58] A. K. Hamze, M. Reynaud, J. Geler-Kremer, and A. A. Demkov, "Design rules for strong electro-optic materials," *npj Computational Materials*, vol. 6, p. 130, 2020. [Online]. Available: <https://doi.org/10.1038/s41524-020-00399-z>
- [59] P. Castera, D. Tulli, A. M. Gutierrez, and P. Sanchis, "Influence of BaTiO₃ ferroelectric orientation for electro-optic modulation on silicon," *Opt. Express*, vol. 23, pp. 15 332–15 342, 6 2015. [Online]. Available: <http://www.opticsexpress.org/abstract.cfm?URI=oe-23-12-15332>
- [60] K. J. Kormondy, Y. Popoff, M. Sousa, F. Eltes, D. Caimi, M. D. Rossell, M. Fiebig, P. Hoffmann, C. Marchiori, M. Reinke, M. Trassin, A. A. Demkov, J. Fompeyrine, and S. Abel, "Microstructure and ferroelectricity of BaTiO₃ thin films on Si for integrated photonics," *Nanotechnology*, vol. 28, p. 75706, 1 2017. [Online]. Available: <https://doi.org/10.1088%2F1361-6528%2Faa53c2>
- [61] E. L. Lin, A. B. Posadas, L. Zheng, J. E. Ortmann, S. Abel, J. Fompeyrine, K. Lai, A. A. Demkov, and J. G. Ekerdt, "Atomic layer deposition of epitaxial ferroelectric barium titanate on Si(001) for electronic and photonic applications," *Journal of Applied Physics*, vol. 126, p. 64101, 8 2019, doi: 10.1063/1.5087571. [Online]. Available: <https://doi.org/10.1063/1.5087571>
- [62] P. Castera, A. M. Gutierrez, D. Tulli, S. Cueff, R. Orobtchouk, P. R. Romeo, G. Saint-Girons, and P. Sanchis, "Electro-Optical Modulation Based on Pockels Effect in BaTiO₃ With a Multi-Domain Structure," *IEEE Photonics Technology Letters*, vol. 28, pp. 990–993, 2016. [Online]. Available: <https://doi.org/10.1109/LPT.2016.2522509>
- [63] L. Mazet, R. Bachelet, L. Louahadj, D. Albertini, B. Gautier, R. Cours, S. Schamm-Chardon, G. Saint-Girons, and C. Dubourdieu, "Structural study and ferroelectricity of epitaxial BaTiO₃ films on silicon grown by molecular beam epitaxy," *Journal of Applied Physics*, vol. 116, p. 214102, 12 2014, doi: 10.1063/1.4902165. [Online]. Available: <https://doi.org/10.1063/1.4902165>

- [64] K. J. Kormondy, S. Abel, F. Fallegger, Y. Popoff, P. Ponath, A. B. Posadas, M. Sousa, D. Caimi, H. Siegwart, E. Uccelli, L. Czornomaz, C. Marchiori, J. Fompeyrine, and A. A. Demkov, “Analysis of the Pockels effect in ferroelectric barium titanate thin films on Si(001),” *Microelectronic Engineering*, vol. 147, pp. 215–218, 2015. [Online]. Available: <https://www.sciencedirect.com/science/article/pii/S0167931715002531>
- [65] J. Lyu, S. Estandía, J. Gazquez, M. F. Chisholm, I. Fina, N. Dix, J. Fontcuberta, and F. Sánchez, “Control of Polar Orientation and Lattice Strain in Epitaxial BaTiO₃ Films on Silicon,” *ACS Applied Materials and Interfaces*, vol. 10, pp. 25 529–25 535, 8 2018, doi: 10.1021/acsami.8b07778. [Online]. Available: <https://doi.org/10.1021/acsami.8b07778>
- [66] C. Dubourdieu, J. Bruley, T. M. Arruda, A. Posadas, J. Jordan-Sweet, M. M. Frank, E. Cartier, D. J. Frank, S. V. Kalinin, A. A. Demkov, and V. Narayanan, “Switching of ferroelectric polarization in epitaxial BaTiO₃ films on silicon without a conducting bottom electrode,” *Nature Nanotechnology*, vol. 8, pp. 748–754, 2013. [Online]. Available: <https://doi.org/10.1038/nnano.2013.192>
- [67] S. Abel, F. Eltes, J. E. Ortmann, A. Messner, P. Castera, T. Wagner, D. Urbonas, A. Rosa, A. M. Gutierrez, D. Tulli, P. Ma, B. Baeuerle, A. Josten, W. Heni, D. Caimi, L. Czornomaz, A. A. Demkov, J. Leuthold, P. Sanchis, and J. Fompeyrine, “Large Pockels effect in micro- and nanostructured barium titanate integrated on silicon,” *Nature Materials*, vol. 18, pp. 42–47, 2019. [Online]. Available: <https://doi.org/10.1038/s41563-018-0208-0>
- [68] M.-H. M. Hsu, C. Merckling, S. El Kazzi, M. Pantouvaki, O. Richard, H. Bender, J. Meersschaut, J. Van Campenhout, P. Absil, and D. Van Thourhout, “Diffraction studies for stoichiometry effects in BaTiO₃ grown by molecular beam epitaxy on Ge(001),” *Journal of Applied Physics*, vol. 120, no. 22, p. 225114, 2016. [Online]. Available: <https://doi.org/10.1063/1.4972101>
- [69] M.-H. M. Hsu, D. V. Thourhout, M. Pantouvaki, J. Meersschaut, T. Conard, O. Richard, H. Bender, P. Favia, M. Vila, R. Cid, J. Rubio-Zuazo, G. R. Castro, J. V. Campenhout, P. Absil, and C. Merckling, “Controlled orientation of molecular-beam-epitaxial BaTiO₃ on Si(001) using thickness engineering of BaTiO₃ and SrTiO₃ buffer layers,” *Applied Physics Express*, vol. 10, p. 65501, 5 2017. [Online]. Available: <https://doi.org/10.7567/apex.10.065501>
- [70] C. Merckling, M. Korytov, U. Celano, M.-H. M. Hsu, S. M. Neumayer, S. Jesse, and S. de Gendt, “Epitaxial growth and strain relaxation

- studies of BaTiO₃ and BaTiO₃/SrTiO₃ superlattices grown by MBE on SrTiO₃-buffered Si(001) substrate,” *Journal of Vacuum Science and Technology A*, vol. 37, p. 21510, 1 2019, doi: 10.1116/1.5082237. [Online]. Available: <https://doi.org/10.1116/1.5082237>
- [71] M.-H. M. Hsu, A. Marinelli, C. Merckling, M. Pantouvaki, J. V. Campenhout, P. Absil, and D. V. Thourhout, “Orientation-dependent electro-optical response of BaTiO₃ on SrTiO₃-buffered Si(001) studied via spectroscopic ellipsometry,” *Opt. Mater. Express*, vol. 7, pp. 2030–2039, 6 2017. [Online]. Available: <http://www.osapublishing.org/ome/abstract.cfm?URI=ome-7-6-2030>
- [72] C. N. Berglund and H. J. Braun, “Optical Absorption in Single-Domain Ferroelectric Barium Titanate,” *Physical Review*, vol. 164, pp. 790–799, 12 1967. [Online]. Available: <https://link.aps.org/doi/10.1103/PhysRev.164.790>
- [73] N. Newman and M. Vahidi, “20 - Kinetic Processes in Vapor Phase Epitaxy,” in *Handbook of Crystal Growth (Second Edition)*, T. F. Kuech, Ed. North-Holland, 2015, pp. 835–868. [Online]. Available: <https://www.sciencedirect.com/science/article/pii/B9780444633040000202>
- [74] U. W. Pohl, “Thermodynamics of Epitaxial Layer-Growth,” in *Epitaxy of Semiconductors: Physics and Fabrication of Heterostructures*, U. W. Pohl, Ed. Springer International Publishing, 2020, pp. 207–250. [Online]. Available: https://doi.org/10.1007/978-3-030-43869-2_6
- [75] D. Wang, W. Zhang, W. Zheng, X. Cui, T. Rojo, and Q. Zhang, “Towards High-Safe Lithium Metal Anodes: Suppressing Lithium Dendrites via Tuning Surface Energy,” *Advanced Science*, vol. 4, p. 1600168, 1 2017, <https://doi.org/10.1002/advs.201600168>. [Online]. Available: <https://doi.org/10.1002/advs.201600168>
- [76] A. Y. Cho, “Recent developments in molecular beam epitaxy (MBE),” *Journal of Vacuum Science and Technology*, vol. 16, pp. 275–284, 3 1979, doi: 10.1116/1.569926. [Online]. Available: <https://doi.org/10.1116/1.569926>
- [77] K. Y. Cheng, “Development of molecular beam epitaxy technology for III-V compound semiconductor heterostructure devices,” *Journal of Vacuum Science and Technology A*, vol. 31, p. 50814, 8 2013, doi: 10.1116/1.4816932. [Online]. Available: <https://doi.org/10.1116/1.4816932>
- [78] C. O’Sullivan and G. Guilbault, “Commercial quartz crystal microbalances - theory and applications,” *Biosensors and Bioelectronics*,

- vol. 14, no. 8, pp. 663–670, 1999. [Online]. Available: <https://www.sciencedirect.com/science/article/pii/S0956566399000408>
- [79] S. N. Thomas, “Chapter 10 - Mass spectrometry,” in *Contemporary Practice in Clinical Chemistry (Fourth Edition)*, W. Clarke and M. A. Marzinke, Eds. Academic Press, 2019, pp. 171–185. [Online]. Available: <https://www.sciencedirect.com/science/article/pii/B9780128154991000107>
- [80] B. Fultz and J. M. Howe, “Diffraction from Crystals,” in *Transmission Electron Microscopy and Diffractometry of Materials*, B. Fultz and J. M. Howe, Eds. Springer Berlin Heidelberg, 2008, pp. 223–272. [Online]. Available: https://doi.org/10.1007/978-3-540-73886-2_5
- [81] G.-C. Wang and T.-M. Lu, “Strain measurement of ultrathin epitaxial films using electron diffraction techniques,” *Journal of Applied Physics*, vol. 125, p. 82401, 12 2018, doi: 10.1063/1.5049357. [Online]. Available: <https://doi.org/10.1063/1.5049357>
- [82] C. W. Schneider and T. Lippert, “Laser Ablation and Thin Film Deposition,” in *Laser Processing of Materials*, P. Schaaf, Ed. Springer Berlin Heidelberg, 2010, pp. 89–112. [Online]. Available: https://doi.org/10.1007/978-3-642-13281-0_5
- [83] H.-U. Krebs, M. Weisheit, J. Faupel, E. Süske, T. Scharf, C. Fuhsse, M. Störmer, K. Sturm, M. Seibt, H. Kijewski, D. Nelke, E. Panchenko, and M. Buback, “Pulsed Laser Deposition (PLD) – A Versatile Thin Film Technique,” in *Advances in Solid State Physics*, B. Kramer, Ed. Springer Berlin Heidelberg, 2003, pp. 505–518. [Online]. Available: https://doi.org/10.1007/978-3-540-44838-9_36
- [84] B. Cullity and S. Stock, *Elements of X-ray Diffraction, Third Edition*. Prentice-Hall, 2001.
- [85] K. M. Zimmermann, “Advanced analysis techniques for X-ray reflectivities. Theory and application,” Ph.D. dissertation, Dortmund University (Germany). Mathematisch-Naturwissenschaftliche Fakultaet, 2005. [Online]. Available: https://inis.iaea.org/search/search.aspx?orig_q=RN:41025055
- [86] M. Yasaka, “X-ray thin-film measurement techniques V . X-ray reflectivity measurement,” in *Rigaku Journal*, 2010.
- [87] D. Denning, J. Guyonnet, and B. J. Rodriguez, “Applications of piezoresponse force microscopy in materials research: from inorganic ferroelectrics to biopiezoelectrics and beyond,” *International Materials*

- Reviews*, vol. 61, no. 1, pp. 46–70, 2016. [Online]. Available: <https://doi.org/10.1179/1743280415Y.0000000013>
- [88] W.-K. Chu, J. W. Mayer, and M.-A. Nicolet, “Chapter 1 - Introduction,” in *Backscattering Spectrometry*, W.-K. Chu, J. W. Mayer, and M.-A. Nicolet, Eds. Academic Press, 1978, pp. 1–20. [Online]. Available: <https://www.sciencedirect.com/science/article/pii/B9780121738501500065>
- [89] S. A. Johansson and T. B. Johansson, “Analytical application of particle induced X-ray emission,” *Nuclear Instruments and Methods*, vol. 137, no. 3, pp. 473–516, 1976. [Online]. Available: <https://www.sciencedirect.com/science/article/pii/0029554X76904705>
- [90] R. F. Egerton, “TEM Specimens and Images,” in *Physical Principles of Electron Microscopy: An Introduction to TEM, SEM, and AEM*, R. F. Egerton, Ed. Springer US, 2005, pp. 93–124. [Online]. Available: https://doi.org/10.1007/0-387-26016-1_4
- [91] D. B. Williams and C. B. Carter, “Amplitude Contrast,” in *Transmission Electron Microscopy: A Textbook for Materials Science*, D. B. Williams and C. B. Carter, Eds. Springer US, 2009, pp. 371–388. [Online]. Available: https://doi.org/10.1007/978-0-387-76501-3_22
- [92] P. Favia, M. B. Gonzales, E. Simoen, P. Verheyen, D. Klenov, and H. Bender, “Nanobeam Diffraction: Technique Evaluation and Strain Measurement on Complementary Metal Oxide Semiconductor Devices,” *Journal of The Electrochemical Society*, vol. 158, p. H438, 2011. [Online]. Available: <http://dx.doi.org/10.1149/1.3546851>
- [93] R. T. Haasch, “X-ray Photoelectron Spectroscopy (XPS) and Auger Electron Spectroscopy (AES),” in *Practical Materials Characterization*, M. Sardela, Ed. Springer New York, 2014, pp. 93–132. [Online]. Available: https://doi.org/10.1007/978-1-4614-9281-8_3
- [94] F. A. Stevie and C. L. Donley, “Introduction to x-ray photoelectron spectroscopy,” *Journal of Vacuum Science and Technology A*, vol. 38, p. 63204, 9 2020, doi: 10.1116/6.0000412. [Online]. Available: <https://doi.org/10.1116/6.0000412>
- [95] H. Fujiwara, “Principles of Spectroscopic Ellipsometry,” in *Spectroscopic Ellipsometry*. John Wiley and Sons, Ltd, 1 2007, pp. 81–146, <https://doi.org/10.1002/9780470060193.ch4>. [Online]. Available: <https://doi.org/10.1002/9780470060193.ch4>
- [96] I. J. A. W. Co., “CompleteEASE software manual.”

- [97] D. G. Schlom and J. H. Haeni, "A Thermodynamic Approach to Selecting Alternative Gate Dielectrics," *MRS Bulletin*, vol. 27, pp. 198–204, 2002. [Online]. Available: <https://www.cambridge.org/core/article/thermodynamic-approach-to-selecting-alternative-gate-dielectrics/D3DC2684AEC1BCF00DD600C819BDF524>
- [98] A. Ramstad, G. Brocks, and P. J. Kelly, "Theoretical study of the Si(100) surface reconstruction," *Physical Review B*, vol. 51, pp. 14504–14523, 5 1995. [Online]. Available: <https://link.aps.org/doi/10.1103/PhysRevB.51.14504>
- [99] R. M. Tromp, R. J. Hamers, and J. E. Demuth, "Si(001) Dimer Structure Observed with Scanning Tunneling Microscopy," *Physical Review Letters*, vol. 55, pp. 1303–1306, 9 1985. [Online]. Available: <https://link.aps.org/doi/10.1103/PhysRevLett.55.1303>
- [100] C. R. Ashman, C. J. Först, K. Schwarz, and P. E. Blöchl, "First-principles calculations of strontium on Si(001)," *Physical Review B*, vol. 69, p. 75309, 2 2004. [Online]. Available: <https://link.aps.org/doi/10.1103/PhysRevB.69.075309>
- [101] X. Hu, Z. Yu, J. A. Curless, R. Droopad, K. Eisenbeiser, J. L. Edwards, W. J. Ooms, and D. Sarid, "Comparative study of Sr and Ba adsorption on Si(100)," *Applied Surface Science*, vol. 181, pp. 103–110, 2001. [Online]. Available: <https://www.sciencedirect.com/science/article/pii/S0169433201003798>
- [102] A. A. Denkov and X. Zhang, "Theory of the Sr-induced reconstruction of the Si (001) surface," *Journal of Applied Physics*, vol. 103, p. 103710, 5 2008, doi: 10.1063/1.2924433. [Online]. Available: <https://doi.org/10.1063/1.2924433>
- [103] Y. Liang, S. Gan, and M. Engelhard, "First step towards the growth of single-crystal oxides on Si: Formation of a two-dimensional crystalline silicate on Si(001)," *Applied Physics Letters*, vol. 79, pp. 3591–3593, 11 2001, doi: 10.1063/1.1415372. [Online]. Available: <https://doi.org/10.1063/1.1415372>
- [104] C. J. Först, C. R. Ashman, K. Schwarz, and P. E. Blöchl, "The interface between silicon and a high-k oxide," *Nature*, vol. 427, pp. 53–56, 2004. [Online]. Available: <https://doi.org/10.1038/nature02204>
- [105] J. Robertson, "Band offsets of wide-band-gap oxides and implications for future electronic devices," *Journal of Vacuum Science and Technology B: Microelectronics and Nanometer Structures Processing, Measurement,*

- and Phenomena*, vol. 18, pp. 1785–1791, 5 2000, doi: 10.1116/1.591472. [Online]. Available: <https://avs.scitation.org/doi/abs/10.1116/1.591472>
- [106] K. Eisenbeiser, J. M. Finder, Z. Yu, J. Ramdani, J. A. Curless, J. A. Hallmark, R. Droopad, W. J. Ooms, L. Salem, S. Bradshaw, and C. D. Overgaard, “Field effect transistors with SrTiO₃ gate dielectric on Si,” *Applied Physics Letters*, vol. 76, pp. 1324–1326, 2 2000, doi: 10.1063/1.126023. [Online]. Available: <https://doi.org/10.1063/1.126023>
- [107] R. A. McKee, F. J. Walker, and M. F. Chisholm, “Crystalline Oxides on Silicon: The First Five Monolayers,” *Physical Review Letters*, vol. 81, pp. 3014–3017, 10 1998. [Online]. Available: <https://link.aps.org/doi/10.1103/PhysRevLett.81.3014>
- [108] A. A. Demkov and A. B. Posadas, “Growing SrTiO₃ on Si(001) by Molecular Beam Epitaxy,” in *Integration of Functional Oxides with Semiconductors*, A. A. Demkov and A. B. Posadas, Eds. Springer New York, 2014, pp. 115–158. [Online]. Available: https://doi.org/10.1007/978-1-4614-9320-4_6
- [109] J. Lapano, M. Brahlek, L. Zhang, J. Roth, A. Pogrebnyakov, and R. Engel-Herbert, “Scaling growth rates for perovskite oxide virtual substrates on silicon,” *Nature Communications*, vol. 10, p. 2464, 2019. [Online]. Available: <https://doi.org/10.1038/s41467-019-10273-2>
- [110] R. Droopad, Z. Yu, H. Li, Y. Liang, C. Overgaard, A. Demkov, X. Zhang, K. Moore, K. Eisenbeiser, M. Hu, J. Curless, and J. Finder, “Development of integrated heterostructures on silicon by MBE,” *Journal of Crystal Growth*, vol. 251, pp. 638–644, 2003. [Online]. Available: <http://www.sciencedirect.com/science/article/pii/S0022024802022005>
- [111] J. Ramdani, R. Droopad, Z. Yu, J. A. Curless, C. D. Overgaard, J. Finder, K. Eisenbeiser, J. A. Hallmark, W. J. Ooms, V. Kaushik, P. Alluri, and S. Pietambaram, “Interface characterization of high-quality SrTiO₃ thin films on Si(100) substrates grown by molecular beam epitaxy,” *Applied Surface Science*, vol. 159-160, pp. 127–133, 2000. [Online]. Available: <https://www.sciencedirect.com/science/article/pii/S0169433200000507>
- [112] G. Delhaye, C. Merckling, M. El-Kazzi, G. Saint-Girons, M. Gendry, Y. Robach, G. Hollinger, L. Largeau, and G. Patriarche, “Structural properties of epitaxial SrTiO₃ thin films grown by molecular beam epitaxy on Si(001),” *Journal of Applied Physics*, vol. 100, p. 124109, 12 2006, doi: 10.1063/1.2407273. [Online]. Available: <https://doi.org/10.1063/1.2407273>
- [113] G. Niu, W. W. Peng, G. Saint-Girons, J. Penuelas, P. Roy, J. B. Brubach, J.-L. Maurice, G. Hollinger, and B. Vilquin, “Direct epitaxial

- growth of SrTiO₃ on Si (001): Interface, crystallization and IR evidence of phase transition,” *Thin Solid Films*, vol. 519, pp. 5722–5725, 2011. [Online]. Available: <http://www.sciencedirect.com/science/article/pii/S0040609010018742>
- [114] G. Niu, B. Vilquin, J. Penuelas, C. Botella, G. Hollinger, and G. Saint-Girons, “Heteroepitaxy of SrTiO₃ thin films on Si (001) using different growth strategies: Toward substratelike quality,” *Journal of Vacuum Science and Technology B*, vol. 29, p. 41207, 7 2011, doi: 10.1116/1.3609813. [Online]. Available: <https://doi.org/10.1116/1.3609813>
- [115] T.-H. Wang, R. Gehlhaar, T. Conard, P. Favia, J. Genoe, and C. Merckling, “Interfacial control of SrTiO₃/Si(001) epitaxy and its effect on physical and optical properties,” *Journal of Crystal Growth*, vol. 582, p. 126524, 2022. [Online]. Available: <https://www.sciencedirect.com/science/article/pii/S0022024822000124>
- [116] G. Saint-Girons, R. Bachelet, R. Moalla, B. Meunier, L. Louahadj, B. Canut, A. Carretero-Genevrier, J. Gazquez, P. Regreny, C. Botella, J. Penuelas, M. G. Silly, F. Sirotti, and G. Grenet, “Epitaxy of SrTiO₃ on Silicon: The Knitting Machine Strategy,” *Chemistry of Materials*, vol. 28, pp. 5347–5355, 8 2016, doi: 10.1021/acs.chemmater.6b01260. [Online]. Available: <https://doi.org/10.1021/acs.chemmater.6b01260>
- [117] F. V. E. Hensling, C. Baeumer, M.-A. Rose, F. Gunkel, and R. Dittmann, “SrTiO₃ termination control: a method to tailor the oxygen exchange kinetics,” *Materials Research Letters*, vol. 8, pp. 31–40, 1 2020, doi: 10.1080/21663831.2019.1682705. [Online]. Available: <https://doi.org/10.1080/21663831.2019.1682705>
- [118] A. Kosola, M. Putkonen, L.-S. Johansson, and L. Niinistö, “Effect of annealing in processing of strontium titanate thin films by ALD,” *Applied Surface Science*, vol. 211, pp. 102–112, 2003. [Online]. Available: <https://www.sciencedirect.com/science/article/pii/S0169433203001752>
- [119] E. Bagherisereshki, J. Tran, F. Lei, and N. AuYeung, “Investigation into SrO/SrCO₃ for high temperature thermochemical energy storage,” *Solar Energy*, vol. 160, pp. 85–93, 2018. [Online]. Available: <https://www.sciencedirect.com/science/article/pii/S0038092X17310666>
- [120] M. Tyunina, J. Narkilahti, J. Levoska, D. Chvostova, A. Dejneka, V. Trepakov, and V. Zelezny, “Ultrathin SrTiO₃ films: epitaxy and optical properties,” *Journal of Physics: Condensed Matter*, vol. 21, p. 232203, 5 2009. [Online]. Available: <https://doi.org/10.1088/0953-8984/21/23/232203>

- [121] S. Zollner, A. A. Demkov, R. Liu, P. L. Fejes, R. B. Gregory, P. Alluri, J. A. Curless, Z. Yu, J. Ramdani, R. Droopad, T. E. Tiwald, J. N. Hilfiker, and J. A. Woollam, “Optical properties of bulk and thin-film SrTiO₃ on Si and Pt,” *Journal of Vacuum Science and Technology B: Microelectronics and Nanometer Structures Processing, Measurement, and Phenomena*, vol. 18, pp. 2242–2254, 7 2000, doi: 10.1116/1.1303741. [Online]. Available: <https://avs.scitation.org/doi/abs/10.1116/1.1303741>
- [122] M. Gaidi, L. Stafford, A. Amassian, M. Chaker, J. Margot, L. Martinu, and M. Kulishov, “Influence of the Microstructure on the Optical Characteristics of SrTiO₃ thin films,” *Journal of Materials Research*, vol. 20, pp. 68–74, 2005. [Online]. Available: <https://www.cambridge.org/core/article/influence-of-the-microstructure-on-the-optical-characteristics-of-srtio3-thin-films/2BDF2A659DDB439364C4F33D47073AAA>
- [123] Z. Wang, V. Kugler, U. Helmersson, E. K. Evangelou, N. Konofaos, S. Nakao, and P. Jin, “Characteristics of SrTiO₃ thin films deposited on Si by rf magnetron sputtering at various substrate temperatures,” *Philosophical Magazine B*, vol. 82, pp. 891–903, 5 2002, doi: 10.1080/13642810208218351. [Online]. Available: <https://doi.org/10.1080/13642810208218351>
- [124] Z. Hu, Y. Li, C. Zhang, and B. Ao, “Structural, electronic, optical and bonding properties of strontianite, SrCO₃: First-principles calculations,” *Journal of Physics and Chemistry of Solids*, vol. 98, pp. 65–70, 2016. [Online]. Available: <https://www.sciencedirect.com/science/article/pii/S0022369716301391>
- [125] J. Rams, A. Tejeda, and J. M. Cabrera, “Refractive indices of rutile as a function of temperature and wavelength,” *Journal of Applied Physics*, vol. 82, pp. 994–997, 8 1997, doi: 10.1063/1.365938. [Online]. Available: <https://doi.org/10.1063/1.365938>
- [126] M. Cardona, “Optical Properties and Band Structure of SrTiO₃ and BaTiO₃,” *Physical Review*, vol. 140, pp. A651–A655, 10 1965. [Online]. Available: <https://link.aps.org/doi/10.1103/PhysRev.140.A651>
- [127] G. E. Pynchon and E. F. Sieckmann, “Refractive Index of Strontium Oxide,” *Physical Review*, vol. 143, pp. 595–597, 3 1966. [Online]. Available: <https://link.aps.org/doi/10.1103/PhysRev.143.595>
- [128] M. Wöhlecke, V. Marrello, and A. Onton, “Refractive index of BaTiO₃ and SrTiO₃ films,” *Journal of Applied Physics*, vol. 48, pp. 1748–1750, 4 1977, doi: 10.1063/1.323822. [Online]. Available: <https://doi.org/10.1063/1.323822>

- [129] K. Saravanan, R. Krishnan, S. H. Hsieh, H. T. Wang, Y. F. Wang, W. F. Pong, K. Asokan, D. K. Avasthi, and D. Kanjilal, “Effect of defects and film thickness on the optical properties of ZnO–Au hybrid films,” *RSC Advances*, vol. 5, pp. 40 813–40 819, 2015. [Online]. Available: <http://dx.doi.org/10.1039/C5RA02144H>
- [130] K. W. Böer and U. W. Pohl, “Optical Properties of Defects,” in *Semiconductor Physics*, K. W. Böer and U. W. Pohl, Eds. Springer International Publishing, 2018, pp. 629–676. [Online]. Available: https://doi.org/10.1007/978-3-319-69150-3_17
- [131] B. Reihl, J. G. Bednorz, K. A. Müller, Y. Jugnet, G. Landgren, and J. F. Morar, “Electronic structure of strontium titanate,” *Physical Review B*, vol. 30, pp. 803–806, 7 1984. [Online]. Available: <https://link.aps.org/doi/10.1103/PhysRevB.30.803>
- [132] Z. Ci and Y. Wang, “Preparation, Electronic Structure, and Photoluminescence Properties of Eu²⁺-Activated Carbonate Sr_{1-x}Ba_xCO₃ for White Light-Emitting Diodes,” *Journal of The Electrochemical Society*, vol. 156, p. J267, 2009. [Online]. Available: <https://doi.org/10.1149/1.3166183>
- [133] H. Fujiwara, “Introduction to Spectroscopic Ellipsometry,” in *Spectroscopic Ellipsometry*, H. Fujiwara, Ed. John Wiley and Sons, Ltd, 1 2007, pp. 1–11, wiley Online Books. [Online]. Available: <https://doi.org/10.1002/978047006193.ch1>
- [134] A. B. Mei, Y. Tang, J. Schubert, D. Jena, H. G. Xing, D. C. Ralph, and D. G. Schlom, “Self-assembly and properties of domain walls in BiFeO₃ layers grown via molecular-beam epitaxy,” *APL Materials*, vol. 7, p. 71101, 7 2019, doi: 10.1063/1.5103244. [Online]. Available: <https://doi.org/10.1063/1.5103244>
- [135] Z. Wang, H. P. Nair, G. C. Correa, J. Jeong, K. Lee, E. S. Kim, A. S. H., C. S. Lee, H. J. Lim, D. A. Muller, and D. G. Schlom, “Epitaxial integration and properties of SrRuO₃ on silicon,” *APL Materials*, vol. 6, p. 86101, 8 2018, doi: 10.1063/1.5041940. [Online]. Available: <https://doi.org/10.1063/1.5041940>
- [136] H. Paik, Z. Chen, E. Lochocki, A. S. H., A. Verma, N. Tanen, J. Park, M. Uchida, S. Shang, B.-C. Zhou, M. Brützam, R. Uecker, Z.-K. Liu, D. Jena, K. M. Shen, D. A. Muller, and D. G. Schlom, “Adsorption-controlled growth of La-doped BaSnO₃ by molecular-beam epitaxy,” *APL Materials*, vol. 5, p. 116107, 11 2017, doi: 10.1063/1.5001839. [Online]. Available: <https://doi.org/10.1063/1.5001839>

- [137] R. P. Laughlin, D. A. Currie, R. Contreras-Guererro, A. Dedigama, W. Priyantha, R. Droopad, N. Theodoropoulou, P. Gao, and X. Pan, “Magnetic and structural properties of BiFeO₃ thin films grown epitaxially on SrTiO₃/Si substrates,” *Journal of Applied Physics*, vol. 113, p. 17D919, 4 2013, doi: 10.1063/1.4796150. [Online]. Available: <https://doi.org/10.1063/1.4796150>
- [138] J. F. Ihlefeld, W. Tian, Z.-K. Liu, W. A. Doolittle, M. Bernhagen, P. Reiche, R. Uecker, R. Ramesh, and D. G. Schlom, “Adsorption-Controlled Growth of BiFeO₃ by MBE and Integration with Wide Band Gap Semiconductors,” *IEEE Transactions on Ultrasonics, Ferroelectrics, and Frequency Control*, vol. 56, pp. 1528–1533, 2009. [Online]. Available: <https://doi.org/10.1109/TUFFC.2009.1216>
- [139] Y. Shen, “Carbothermal synthesis of metal-functionalized nanostructures for energy and environmental applications,” *J. Mater. Chem. A*, vol. 3, pp. 13 114–13 188, 2015. [Online]. Available: <http://dx.doi.org/10.1039/C5TA01228G>
- [140] D. Risold, B. Hallstedt, and L. J. Gauckler, “The strontium-oxygen system,” *Calphad*, vol. 20, pp. 353–361, 1996. [Online]. Available: <https://www.sciencedirect.com/science/article/pii/S0364591696000375>
- [141] M. Schreck, H. Roll, and B. Stritzker, “Diamond/Ir/SrTiO₃: A material combination for improved heteroepitaxial diamond films,” *Applied Physics Letters*, vol. 74, pp. 650–652, 1 1999, doi: 10.1063/1.123029. [Online]. Available: <https://doi.org/10.1063/1.123029>
- [142] K. H. Lee, S. Saada, J.-C. Arnault, R. Moalla, G. Saint-Girons, R. Bachelet, H. Bensalah, I. Stenger, J. Barjon, A. Tallaire, and J. Achard, “Epitaxy of iridium on SrTiO₃/Si (001): A promising scalable substrate for diamond heteroepitaxy,” *Diamond and Related Materials*, vol. 66, pp. 67–76, 2016. [Online]. Available: <https://www.sciencedirect.com/science/article/pii/S0925963516300905>
- [143] Y. S. Kim, N. Bansal, C. Chaparro, H. Gross, and S. Oh, “Sr flux stability against oxidation in oxide-molecular-beam-epitaxy environment: Flux, geometry, and pressure dependence,” *Journal of Vacuum Science and Technology A*, vol. 28, pp. 271–276, 2 2010, doi: 10.1116/1.3298880. [Online]. Available: <https://doi.org/10.1116/1.3298880>
- [144] E. S. Hellman and E. H. Hartford, “Effects of oxygen on the sublimation of alkaline earths from effusion cells,” *Journal of Vacuum Science and Technology B: Microelectronics and Nanometer Structures Processing, Measurement, and Phenomena*, vol. 12, pp.

- 1178–1180, 3 1994, doi: 10.1116/1.587036. [Online]. Available: <https://avs.scitation.org/doi/abs/10.1116/1.587036>
- [145] M. A. Moram and M. E. Vickers, “X-ray diffraction of III-nitrides,” *Reports on Progress in Physics*, vol. 72, p. 36502, 2009. [Online]. Available: <http://dx.doi.org/10.1088/0034-4885/72/3/036502>
- [146] F. Niu and B. W. Wessels, “Epitaxial growth and strain relaxation of BaTiO₃ thin films on SrTiO₃ buffered (001) Si by molecular beam epitaxy,” *Journal of Vacuum Science and Technology B: Microelectronics and Nanometer Structures Processing, Measurement, and Phenomena*, vol. 25, pp. 1053–1057, 5 2007, doi: 10.1116/1.2539503. [Online]. Available: <https://avs.scitation.org/doi/abs/10.1116/1.2539503>
- [147] S. Lee, C. A. Randall, and Z.-K. Liu, “Modified Phase Diagram for the Barium Oxide–Titanium Dioxide System for the Ferroelectric Barium Titanate,” *Journal of the American Ceramic Society*, vol. 90, pp. 2589–2594, 8 2007, <https://doi.org/10.1111/j.1551-2916.2007.01794.x> [Online]. Available: <https://doi.org/10.1111/j.1551-2916.2007.01794.x>
- [148] T. Metzger, R. Höpler, E. Born, O. Ambacher, M. Stutzmann, R. Stömmmer, M. Schuster, H. Göbel, S. Christiansen, M. Albrecht, and H. P. Strunk, “Defect structure of epitaxial GaN films determined by transmission electron microscopy and triple-axis X-ray diffractometry,” *Philosophical Magazine A*, vol. 77, pp. 1013–1025, 4 1998, doi: 10.1080/01418619808221225. [Online]. Available: <https://doi.org/10.1080/01418619808221225>
- [149] A. Borzì, S. Dolabella, W. Szmyt, J. Geler-Kremer, S. Abel, J. Fompeyrine, P. Hoffmann, and A. Neels, “Microstructure analysis of epitaxial BaTiO₃ thin films on SrTiO₃-buffered Si: Strain and dislocation density quantification using HRXRD methods,” *Materialia*, vol. 14, p. 100953, 2020. [Online]. Available: <https://www.sciencedirect.com/science/article/pii/S2589152920303690>
- [150] E. Arslan, M. K. Ozturk, A. Teke, S. Ozcelik, and E. Ozbay, “Buffer optimization for crack-free GaN epitaxial layers grown on Si(111) substrate by MOCVD,” *Journal of Physics D: Applied Physics*, vol. 41, p. 155317, 2008. [Online]. Available: <https://dx.doi.org/10.1088/0022-3727/41/15/155317>
- [151] S. H. Wemple, M. Didomenico, and I. Camlibel, “Dielectric and optical properties of melt-grown BaTiO₃,” *Journal of Physics and Chemistry of Solids*, vol. 29, pp. 1797–1803, 1968. [Online]. Available: <https://www.sciencedirect.com/science/article/pii/0022369768901649>

- [152] G. Gupta, T. Nautiyal, and S. Auluck, “Optical properties of the compounds BaTiO₃ and SrTiO₃,” *Physical Review B*, vol. 69, p. 52101, 2 2004. [Online]. Available: <https://link.aps.org/doi/10.1103/PhysRevB.69.052101>
- [153] E. Chernova, O. Pacherova, D. Chvostova, A. Dejneka, T. Kocourek, M. Jelinek, and M. Tyunina, “Strain-controlled optical absorption in epitaxial ferroelectric BaTiO₃ films,” *Applied Physics Letters*, vol. 106, p. 192903, 5 2015, doi: 10.1063/1.4921083. [Online]. Available: <https://doi.org/10.1063/1.4921083>
- [154] A. Karvounis, F. Timpu, V. V. Vogler-Neuling, R. Savo, and R. Grange, “Barium Titanate Nanostructures and Thin Films for Photonics,” *Advanced Optical Materials*, vol. 8, p. 2001249, 12 2020, <https://doi.org/10.1002/adom.202001249>. [Online]. Available: <https://doi.org/10.1002/adom.202001249>
- [155] J. Schubert, O. Trithaveesak, A. Petraru, C. L. Jia, R. Uecker, P. Reiche, and D. G. Schlom, “Structural and optical properties of epitaxial BaTiO₃ thin films grown on GdScO₃(110),” *Applied Physics Letters*, vol. 82, pp. 3460–3462, 5 2003, doi: 10.1063/1.1575935. [Online]. Available: <https://doi.org/10.1063/1.1575935>
- [156] R. Groenen, J. Smit, K. Orsel, A. Vailionis, B. Bastiaens, M. Huijben, K. Boller, G. Rijnders, and G. Koster, “Research Update: Stoichiometry controlled oxide thin film growth by pulsed laser deposition,” *APL Materials*, vol. 3, p. 070701, 7 2015, doi: 10.1063/1.4926933. [Online]. Available: <https://doi.org/10.1063/1.4926933>
- [157] F. He and B. O. Wells, “Lattice strain in epitaxial BaTiO₃ thin films,” *Applied Physics Letters*, vol. 88, p. 152908, 4 2006, doi: 10.1063/1.2194231. [Online]. Available: <https://doi.org/10.1063/1.2194231>
- [158] M. Spreitzer, D. Klement, R. Egoavil, J. Verbeeck, J. Kovač, A. Založník, G. Koster, G. V. Tendeloo, D. Suvorov, and G. Rijnders, “Growth mechanism of epitaxial SrTiO₃ on a (1 × 2) + (2 × 1) reconstructed Sr(1/2 ML)/Si(001) surface,” *J. Mater. Chem. C*, vol. 8, pp. 518–527, 2020. [Online]. Available: <http://dx.doi.org/10.1039/C9TC04092G>
- [159] T.-H. Wang, P.-C. B. Hsu, M. Korytov, J. Genoe, and C. Merckling, “Polarization control of epitaxial barium titanate (BaTiO₃) grown by pulsed-laser deposition on a MBE-SrTiO₃/Si(001) pseudo-substrate,” *Journal of Applied Physics*, vol. 128, p. 104104, 9 2020, doi: 10.1063/5.0019980. [Online]. Available: <https://doi.org/10.1063/5.0019980>

- [160] M. R. Sardela and G. V. Hansson, "Thermal relaxation kinetics of strained Si/Si_{1-x}Ge_x heterostructures determined by direct measurement of mosaicity and lattice parameter variations," *Journal of Vacuum Science and Technology A*, vol. 13, pp. 314–326, 3 1995, doi: 10.1116/1.579416. [Online]. Available: <https://doi.org/10.1116/1.579416>
- [161] R. Chierchia, "Strain and crystalline defects in epitaxial GaN layers studied by high-resolution X-ray diffraction," Ph.D. dissertation, Universität Bremen, 2007.
- [162] T. Scharf and H. U. Krebs, "Influence of inert gas pressure on deposition rate during pulsed laser deposition," *Applied Physics A*, vol. 75, pp. 551–554, 2002. [Online]. Available: <https://doi.org/10.1007/s00339-002-1442-4>
- [163] B. S. Kwak, A. Erbil, J. D. Budai, M. F. Chisholm, L. A. Boatner, and B. J. Wilkens, "Domain formation and strain relaxation in epitaxial ferroelectric heterostructures," *Physical Review B*, vol. 49, pp. 14865–14879, 6 1994. [Online]. Available: <https://link.aps.org/doi/10.1103/PhysRevB.49.14865>
- [164] J. Gazquez, S. Bose, M. Sharma, M. A. Torija, S. J. Pennycook, C. Leighton, and M. Varela, "Lattice mismatch accommodation via oxygen vacancy ordering in epitaxial La_{0.5}Sr_{0.5}CoO_{3-δ} thin films," *APL Materials*, vol. 1, p. 12105, 6 2013, doi: 10.1063/1.4809547. [Online]. Available: <https://doi.org/10.1063/1.4809547>
- [165] D. O. Klenov, W. Donner, B. Foran, and S. Stemmer, "Impact of stress on oxygen vacancy ordering in epitaxial (La_{0.5}Sr_{0.5})CoO_{3-δ} thin films," *Applied Physics Letters*, vol. 82, pp. 3427–3429, 5 2003, doi: 10.1063/1.1575503. [Online]. Available: <https://doi.org/10.1063/1.1575503>
- [166] M. Scigaj, N. Dix, I. Fina, R. Bachelet, B. Warot-Fonrose, J. Fontcuberta, and F. Sánchez, "Ultra-flat BaTiO₃ epitaxial films on Si(001) with large out-of-plane polarization," *Applied Physics Letters*, vol. 102, p. 112905, 3 2013, doi: 10.1063/1.4798246. [Online]. Available: <https://doi.org/10.1063/1.4798246>
- [167] O. Trithaveesak, J. Schubert, and C. Buchal, "Ferroelectric properties of epitaxial BaTiO₃ thin films and heterostructures on different substrates," *Journal of Applied Physics*, vol. 98, p. 114101, 12 2005, doi: 10.1063/1.2135891. [Online]. Available: <https://doi.org/10.1063/1.2135891>
- [168] D. K. Schroder, "Oxide and Interface Trapped Charges, Oxide Thickness," in *Semiconductor Material and Device Characterization*. Wiley-IEEE Press, 10 2005, pp. 319–387, <https://doi.org/10.1002/0471749095.ch6> [Online]. Available: <https://doi.org/10.1002/0471749095.ch6>

- [169] A. E. O. Persson, R. Athle, J. Svensson, M. Borg, and L.-E. Wernersson, “A method for estimating defects in ferroelectric thin film MOSCAPs,” *Applied Physics Letters*, vol. 117, p. 242902, 12 2020, doi: 10.1063/5.0029210. [Online]. Available: <https://doi.org/10.1063/5.0029210>
- [170] Y. Zhang, Y. Y. Shao, X. B. Lu, M. Zeng, Z. Zhang, X. S. Gao, X. J. Zhang, J.-M. Liu, and J. Y. Dai, “Defect states and charge trapping characteristics of HfO₂ films for high performance nonvolatile memory applications,” *Applied Physics Letters*, vol. 105, p. 172902, 10 2014, doi: 10.1063/1.4900745. [Online]. Available: <https://doi.org/10.1063/1.4900745>
- [171] J. Tao, C. Z. Zhao, C. Zhao, P. Taechakumput, M. Werner, S. Taylor, and P. R. Chalker, “Extrinsic and Intrinsic Frequency Dispersion of High-k Materials in Capacitance-Voltage Measurements,” *Materials*, vol. 5, pp. 1005–1032, 2012. [Online]. Available: <https://www.mdpi.com/1996-1944/5/6/1005>
- [172] L. Zhu, “Exploring Strategies for High Dielectric Constant and Low Loss Polymer Dielectrics,” *The Journal of Physical Chemistry Letters*, vol. 5, pp. 3677–3687, 11 2014, doi: 10.1021/jz501831q. [Online]. Available: <https://doi.org/10.1021/jz501831q>
- [173] Y. Wu and G. Cao, “Ferroelectric and Dielectric Properties of Strontium Bismuth Niobate Vanadates,” *Journal of Materials Research*, vol. 15, pp. 1583–1590, 2000. [Online]. Available: <https://doi.org/10.1557/JMR.2000.0227>
- [174] G. Niu, B. Gautier, S. Yin, G. Saint-Girons, P. Lecoer, V. Pillard, G. Hollinger, and B. Vilquin, “Molecular beam epitaxy growth of BaTiO₃ thin films and crucial impact of oxygen content conditions on the electrical characteristics,” *Thin Solid Films*, vol. 520, pp. 4595–4599, 2012. [Online]. Available: <http://www.sciencedirect.com/science/article/pii/S0040609011019237>
- [175] V. Srikant, E. J. Tarsa, D. R. Clarke, and J. S. Speck, “Crystallographic orientation of epitaxial BaTiO₃ films: The role of thermal-expansion mismatch with the substrate,” *Journal of Applied Physics*, vol. 77, pp. 1517–1522, 2 1995, doi: 10.1063/1.358902. [Online]. Available: <https://doi.org/10.1063/1.358902>
- [176] E. Garcia-Caurel, A. D. Martino, J.-P. Gaston, and L. Yan, “Application of Spectroscopic Ellipsometry and Mueller Ellipsometry to Optical Characterization,” *Appl. Spectrosc.*, vol. 67, pp. 1–21, 1 2013. [Online]. Available: <http://opg.optica.org/as/abstract.cfm?URI=as-67-1-1>

- [177] S. A. Hall, M.-A. Hoyle, J. S. Post, and D. K. Hore, “Combined Stokes Vector and Mueller Matrix Polarimetry for Materials Characterization,” *Analytical Chemistry*, vol. 85, pp. 7613–7619, 8 2013, doi: 10.1021/ac401864g. [Online]. Available: <https://doi.org/10.1021/ac401864g>
- [178] P. F. Ndione, M. Gaidi, C. Durand, M. Chaker, R. Morandotti, and G. Rioux, “Structural and optical properties of epitaxial $\text{Ca}_x\text{Ba}_{1-x}\text{Nb}_2\text{O}_6$ thin films grown on MgO by pulsed laser deposition,” *Journal of Applied Physics*, vol. 103, p. 33510, 2 2008, doi: 10.1063/1.2838176. [Online]. Available: <https://doi.org/10.1063/1.2838176>
- [179] K. Prabhakaran, F. Maeda, Y. Watanabe, and T. Ogino, “Thermal decomposition pathway of Ge and Si oxides: observation of a distinct difference,” *Thin Solid Films*, vol. 369, pp. 289–292, 2000. [Online]. Available: <https://www.sciencedirect.com/science/article/pii/S0040609000008816>
- [180] P. Ponath, A. B. Posadas, R. C. Hatch, and A. A. Demkov, “Preparation of a clean Ge(001) surface using oxygen plasma cleaning,” *Journal of Vacuum Science and Technology B*, vol. 31, p. 31201, 4 2013, doi: 10.1116/1.4798390. [Online]. Available: <https://doi.org/10.1116/1.4798390>
- [181] E. L. Lin, A. B. Posadas, H. W. Wu, D. J. Smith, A. A. Demkov, and J. G. Ekerdt, “Epitaxial growth of barium titanate thin films on germanium via atomic layer deposition,” *Journal of Crystal Growth*, vol. 476, pp. 6–11, 2017. [Online]. Available: <https://www.sciencedirect.com/science/article/pii/S0022024817304876>
- [182] L. Dai, G. Niu, J. Zhao, Y. Xue, R. Luo, B. Chen, R. An, Y. Sun, B. Feng, S. Ding, W. Luo, Z.-G. Ye, and W. Ren, “Oxygen vacancy induced phase and conductivity transition of epitaxial $\text{BaTiO}_{3-\delta}$ films directly grown on Ge (001) without surface passivation,” *Journal of Applied Physics*, vol. 129, p. 45302, 1 2021, doi: 10.1063/5.0036604. [Online]. Available: <https://doi.org/10.1063/5.0036604>
- [183] S. Hu, E. L. Lin, A. K. Hamze, A. Posadas, H. Wu, D. J. Smith, A. A. Demkov, and J. G. Ekerdt, “Zintl layer formation during perovskite atomic layer deposition on Ge (001),” *The Journal of Chemical Physics*, vol. 146, p. 52817, 12 2016, doi: 10.1063/1.4972071. [Online]. Available: <https://doi.org/10.1063/1.4972071>
- [184] C. Merckling, G. Saint-Girons, C. Botella, G. Hollinger, M. Heyns, J. Dekoster, and M. Caymax, “Molecular beam epitaxial growth of BaTiO_3 single crystal on Ge-on-Si(001) substrates,” *Applied Physics*

- Letters*, vol. 98, p. 92901, 2 2011, doi: 10.1063/1.3558997. [Online]. Available: <https://doi.org/10.1063/1.3558997>
- [185] K. D. Fredrickson, P. Ponath, A. B. Posadas, M. R. McCartney, T. Aoki, D. J. Smith, and A. A. Demkov, “Atomic and electronic structure of the ferroelectric BaTiO₃/Ge(001) interface,” *Applied Physics Letters*, vol. 104, p. 242908, 6 2014, doi: 10.1063/1.4883883. [Online]. Available: <https://doi.org/10.1063/1.4883883>
- [186] L. Mazet, S. M. Yang, S. V. Kalinin, S. Schamm-Chardon, and C. Dubourdieu, “A review of molecular beam epitaxy of ferroelectric BaTiO₃ films on Si, Ge and GaAs substrates and their applications,” *Science and Technology of Advanced Materials*, vol. 16, p. 36005, 6 2015. [Online]. Available: <https://doi.org/10.1088%2F1468-6996%2F16%2F3%2F036005>
- [187] C. Buchal, L. Beckers, A. Eckau, J. Schubert, and W. Zander, “Epitaxial BaTiO₃ thin films on MgO,” *Materials Science and Engineering: B*, vol. 56, pp. 234–238, 1998. [Online]. Available: <https://www.sciencedirect.com/science/article/pii/S0921510798002190>
- [188] B. Kim, Y.-U. Jeon, C. Lee, I. S. Kim, B.-H. Lee, Y.-H. Kim, Y. D. Kim, I. K. Han, K. Lee, J. Kim, and J. Kang, “Controlling of lattice strains for crack-free and strong ferroelectric barium titanate films by post-thermal treatment,” *Scientific Reports*, vol. 12, p. 5363, 2022. [Online]. Available: <https://doi.org/10.1038/s41598-022-09182-0>
- [189] M. E. Marssi, F. L. Marrec, I. A. Lukyanchuk, and M. G. Karkut, “Ferroelectric transition in an epitaxial barium titanate thin film: Raman spectroscopy and x-ray diffraction study,” *Journal of Applied Physics*, vol. 94, pp. 3307–3312, 8 2003, doi: 10.1063/1.1596720. [Online]. Available: <https://doi.org/10.1063/1.1596720>
- [190] Y. K. Jeong and B. W. Wessels, “Properties of epitaxial barium titanate thin films using a highly volatile Ba(hfa)₂triglyme precursor,” *Journal of Vacuum Science and Technology B*, vol. 33, p. 51206, 7 2015, doi: 10.1116/1.4927380. [Online]. Available: <https://doi.org/10.1116/1.4927380>
- [191] S. Kim, S. Hishita, Y. M. Kang, and S. Baik, “Structural characterization of epitaxial BaTiO₃ thin films grown by sputter deposition on MgO(100),” *Journal of Applied Physics*, vol. 78, pp. 5604–5608, 11 1995, doi: 10.1063/1.360696. [Online]. Available: <https://doi.org/10.1063/1.360696>
- [192] H. Z. Guo, Z. H. Chen, B. L. Cheng, H. B. Lu, L. F. Liu, and Y. L. Zhou, “Structure dynamics of strongly reduced epitaxial

- BaTiO_{3-x} studied by Raman scattering,” *Journal of the European Ceramic Society*, vol. 25, pp. 2347–2352, 2005. [Online]. Available: <https://www.sciencedirect.com/science/article/pii/S0955221905002153>
- [193] S. Chattopadhyay, A. R. Teren, J.-H. Hwang, T. O. Mason, and B. W. Wessels, “Diffuse Phase Transition in Epitaxial BaTiO₃ Thin Films,” *Journal of Materials Research*, vol. 17, pp. 669–674, 2002. [Online]. Available: <https://doi.org/10.1557/JMR.2002.0095>
- [194] Y. Yoneda, T. Okabe, K. Sakaue, and H. Terauchi, “Growth of ultrathin BaTiO₃ films on SrTiO₃ and MgO substrates,” *Surface Science*, vol. 410, pp. 62–69, 1998. [Online]. Available: <https://www.sciencedirect.com/science/article/pii/S0039602898002969>
- [195] J. H. Lee, J. H. Eun, S. G. Kim, S. Y. Park, M. J. Lee, and H. J. Kim, “Hydration behavior of MgO single crystals and thin films,” *Journal of Materials Research*, vol. 18, pp. 2895–2903, 2003. [Online]. Available: <https://doi.org/10.1557/JMR.2003.0404>
- [196] C. Merckling, M. El-Kazzi, G. Delhaye, V. Favre-Nicolin, Y. Robach, M. Gendry, G. Grenet, G. Saint-Girons, and G. Hollinger, “Strain relaxation and critical thickness for epitaxial LaAlO₃ thin films grown on SrTiO₃(001) substrates by molecular beam epitaxy,” *Journal of Crystal Growth*, vol. 306, pp. 47–51, 2007. [Online]. Available: <https://www.sciencedirect.com/science/article/pii/S0022024807004411>
- [197] A. S. Verma and V. K. Jindal, “Lattice constant of cubic perovskites,” *Journal of Alloys and Compounds*, vol. 485, pp. 514–518, 2009. [Online]. Available: <https://www.sciencedirect.com/science/article/pii/S0925838809011578>
- [198] D. de Ligny and P. Richet, “High-temperature heat capacity and thermal expansion of SrTiO₃ and SrZrO₃ perovskites,” *Physical Review B*, vol. 53, pp. 3013–3022, 2 1996. [Online]. Available: <https://link.aps.org/doi/10.1103/PhysRevB.53.3013>
- [199] M. Zapf, M. Stübinger, L. Jin, M. Kamp, F. Pfaff, A. Lubk, B. Büchner, M. Sing, and R. Claessen, “Domain matching epitaxy of BaBiO₃ on SrTiO₃ with structurally modified interface,” *Applied Physics Letters*, vol. 112, p. 141601, 4 2018, doi: 10.1063/1.5016116. [Online]. Available: <https://doi.org/10.1063/1.5016116>
- [200] A. Prakash, J. Dewey, H. Yun, J. S. Jeong, K. A. Mkhdyan, and B. Jalan, “Hybrid molecular beam epitaxy for the growth of stoichiometric BaSnO₃,” *Journal of Vacuum Science and Technology A*,

- vol. 33, p. 60608, 10 2015, doi: 10.1116/1.4933401. [Online]. Available: <https://doi.org/10.1116/1.4933401>
- [201] Y. He, R. Wei, C. Zhou, W. Cheng, X. Ding, C. Shao, L. Hu, W. Song, X. Zhu, and Y. Sun, “Microstructural Engineering of Solution-Processed Epitaxial La-Doped BaSnO₃ Transparent Conducting Films,” *Crystal Growth and Design*, vol. 21, pp. 5800–5806, 10 2021, doi: 10.1021/acs.cgd.1c00698. [Online]. Available: <https://doi.org/10.1021/acs.cgd.1c00698>
- [202] R. Zhang, X. Li, J. Bi, S. Zhang, S. Peng, Y. Song, Q. Zhang, L. Gu, J. Duan, and Y. Cao, “One-step epitaxy of high-mobility La-doped BaSnO₃ films by high-pressure magnetron sputtering,” *APL Materials*, vol. 9, p. 61103, 6 2021, doi: 10.1063/5.0046639. [Online]. Available: <https://doi.org/10.1063/5.0046639>
- [203] S. Raghavan, T. Schumann, H. Kim, J. Y. Zhang, T. A. Cain, and S. Stemmer, “High-mobility BaSnO₃ grown by oxide molecular beam epitaxy,” *APL Materials*, vol. 4, p. 16106, 1 2016, doi: 10.1063/1.4939657. [Online]. Available: <https://doi.org/10.1063/1.4939657>
- [204] A. Prakash, P. Xu, X. Wu, G. Haugstad, X. Wang, and B. Jalan, “Adsorption-controlled growth and the influence of stoichiometry on electronic transport in hybrid molecular beam epitaxy-grown BaSnO₃ films,” *J. Mater. Chem. C*, vol. 5, pp. 5730–5736, 2017. [Online]. Available: <http://dx.doi.org/10.1039/C7TC00190H>
- [205] Z. Wang, H. Paik, Z. Chen, D. A. Muller, and D. G. Schlom, “Epitaxial integration of high-mobility La-doped BaSnO₃ thin films with silicon,” *APL Materials*, vol. 7, p. 22520, 1 2019, doi: 10.1063/1.5054810. [Online]. Available: <https://doi.org/10.1063/1.5054810>
- [206] M. Reynaud, P.-Y. Chen, W. Li, T. Paoletta, S. Kwon, D. H. Lee, I. Beskin, A. B. Posadas, M. J. Kim, C. M. Landis, K. Lai, J. G. Ekerdt, and A. A. Demkov, “Electro-optic response in epitaxially stabilized orthorhombic mm2 BaTiO₃,” *Physical Review Materials*, vol. 5, p. 35201, 3 2021. [Online]. Available: <https://link.aps.org/doi/10.1103/PhysRevMaterials.5.035201>
- [207] M. Sawkar-Mathur, C. Marchiori, J. Fompeyrine, M. F. Toney, J. Bargar, and J. P. Chang, “Structural properties of epitaxial SrHfO₃ thin films on Si (001),” *Thin Solid Films*, vol. 518, pp. S118–S122, 2010. [Online]. Available: <https://www.sciencedirect.com/science/article/pii/S0040609009017118>
- [208] M. D. McDaniel, C. Hu, S. Lu, T. Q. Ngo, A. Posadas, A. Jiang, D. J. Smith, E. T. Yu, A. A. Demkov, and J. G. Ekerdt, “Atomic layer

- deposition of crystalline SrHfO₃ directly on Ge (001) for high-k dielectric applications,” *Journal of Applied Physics*, vol. 117, p. 54101, 2 2015, doi: 10.1063/1.4906953. [Online]. Available: <https://doi.org/10.1063/1.4906953>
- [209] M. Sousa, C. Rossel, C. Marchiori, H. Siegwart, D. Caimi, J.-P. Locquet, D. J. Webb, R. Germann, J. Fompeyrine, K. Babich, J. W. Seo, and C. Dieker, “Optical properties of epitaxial SrHfO₃ thin films grown on Si,” *Journal of Applied Physics*, vol. 102, p. 104103, 11 2007, doi: 10.1063/1.2812425. [Online]. Available: <https://doi.org/10.1063/1.2812425>
- [210] C. Rossel, B. Mereu, C. Marchiori, D. Caimi, M. Sousa, A. Guiller, H. Siegwart, R. Germann, J.-P. Locquet, J. Fompeyrine, D. J. Webb, C. Dieker, and J. W. Seo, “Field-effect transistors with SrHfO₃ as gate oxide,” *Applied Physics Letters*, vol. 89, p. 53506, 7 2006, doi: 10.1063/1.2236464. [Online]. Available: <https://doi.org/10.1063/1.2236464>
- [211] C. Hu, M. D. McDaniel, A. Jiang, A. Posadas, A. A. Demkov, J. G. Ekerdt, and E. T. Yu, “A Low-Leakage Epitaxial High- κ Gate Oxide for Germanium Metal-Oxide-Semiconductor Devices,” *ACS Applied Materials and Interfaces*, vol. 8, pp. 5416–5423, 3 2016, doi: 10.1021/acsmami.5b10661. [Online]. Available: <https://doi.org/10.1021/acsmami.5b10661>
- [212] Z. H. Lim, K. Ahmadi-Majlan, E. D. Grimley, Y. Du, M. Bowden, R. Moghadam, J. M. LeBeau, S. A. Chambers, and J. H. Ngai, “Structural and electrical properties of single crystalline SrZrO₃ epitaxially grown on Ge (001),” *Journal of Applied Physics*, vol. 122, p. 84102, 8 2017, doi: 10.1063/1.5000142. [Online]. Available: <https://doi.org/10.1063/1.5000142>
- [213] S. Hu, L. Ji, P.-Y. Chen, B. I. Edmondson, H.-L. Chang, A. Posadas, H. W. Wu, E. T. Yu, D. J. Smith, A. A. Demkov, and J. G. Ekerdt, “Crystalline SrZrO₃ deposition on Ge (001) by atomic layer deposition for high-k dielectric applications,” *Journal of Applied Physics*, vol. 124, p. 44102, 7 2018, doi: 10.1063/1.5026790. [Online]. Available: <https://doi.org/10.1063/1.5026790>
- [214] Y. Zhao and D. J. Weidner, “Thermal expansion of SrZrO₃ and BaZrO₃ perovskites,” *Physics and Chemistry of Minerals*, vol. 18, pp. 294–301, 1991. [Online]. Available: <https://doi.org/10.1007/BF00200187>
- [215] S. Yamanaka, T. Maekawa, H. Muta, T. Matsuda, S. ichi Kobayashi, and K. Kurosaki, “Thermophysical properties of SrHfO₃ and SrRuO₃,” *Journal of Solid State Chemistry*, vol. 177, pp. 3484–3489, 2004. [Online]. Available: <https://www.sciencedirect.com/science/article/pii/S0022459604002701>

- [216] R. Loo, G. Wang, L. Souriau, J. C. Lin, S. Takeuchi, G. Brammertz, and M. Caymax, “High Quality Ge Virtual Substrates on Si Wafers with Standard STI Patterning,” *Journal of The Electrochemical Society*, vol. 157, p. H13, 2010. [Online]. Available: <https://dx.doi.org/10.1149/1.3244564>
- [217] H. Tian, A.-J. Mao, H. J. Zhao, Y. Cui, H. Li, and X.-Y. Kuang, “Large polarization and dielectric response in epitaxial SrZrO₃ films,” *Phys. Chem. Chem. Phys.*, vol. 18, pp. 7680–7687, 2016. [Online]. Available: <http://dx.doi.org/10.1039/C5CP07881D>
- [218] G. Nazir, A. Ahmad, M. F. Khan, and S. Tariq, “Putting DFT to the trial: First principles pressure dependent analysis on optical properties of cubic perovskite SrZrO₃,” *Computational Condensed Matter*, vol. 4, pp. 32–39, 2015. [Online]. Available: <https://www.sciencedirect.com/science/article/pii/S2352214315300046>
- [219] O. L. Alerhand, A. N. Berker, J. D. Joannopoulos, D. Vanderbilt, R. J. Hamers, and J. E. Demuth, “Finite-temperature phase diagram of vicinal Si(100) surfaces,” *Physical Review Letters*, vol. 64, pp. 2406–2409, 5 1990. [Online]. Available: <https://link.aps.org/doi/10.1103/PhysRevLett.64.2406>

List of Publications

Journal Article / Conference Proceedings

1. T.-H. Wang, P.-C.(Brent) Hsu, M. Korytov, J. Genoe, and C. Merckling, “Polarization control of epitaxial barium titanate (BaTiO_3) grown by pulsed-laser deposition on a MBE- $\text{SrTiO}_3/\text{Si}(001)$ pseudosubstrate,” *J. Appl. Phys.* 128, 104104 (2020); doi: 10.1063/5.0019980
2. T.-H. Wang, R. Gehlhaar, T. Conard, P. Favia, J. Genoe and C. Merckling, “Interfacial control of $\text{SrTiO}_3/\text{Si}(001)$ epitaxy and its effect on physical and optical properties,” *J. Cryst. Growth* 582(2022) 126524; doi.org/10.1016/j.jcrysgro.2022.126524
3. C. Merckling, I. Ahmed, T.-H. Wang, M. Kaviani, J. Genoe, and S. de Gendt, “(Invited) Integrated Perovskites Oxides on Silicon: From Optical to Quantum Applications,” 2022 Meet. Abstr. MA2022-01 1060
4. G. Croes, N. Smolentsev, T.-H. Wang, R. Gehlhaar, and J. Genoe, “Non-linear electro-optic modelling of a barium titanate grating coupler,” *Proc. SPIE* 11484, Optical Modeling and Performance Predictions XI, 114840D (20 August 2020); <https://doi.org/10.1117/12.2568032>
5. S. Chang, M. Zhao, V. Spampinato, A. Franquet, T.-H. Do, A. Uedono, T.-T. Luong, T.-H. Wang, L. Chang, “The Influence of AlN Nucleation Layer on Radio Frequency Transmission Loss of AlN-on-Si Heterostructure,” *Phys. Status Solidi A*, 217: 1900755, 2020. <https://doi.org/10.1002/pssa.20190075>

Conference Presentation

1. T.-H. Wang, M. Korytov, P.-C.(Brent) Hsu, J. Genoe, and C. Merckling, “Single Crystalline BaTiO_3 Grown by Pulsed-Laser Deposition (PLD)

- on SrTiO₃ / Si Pseudo-Substrate,” E-MRS, Strasbourg, France. Proc. E-MRS String. Strasbourg, France. 25 May 2020
2. T.-H. Wang, R. Gehlhaar, T. Conard, J. Genoe and C. Merckling, “Interface Control and Characterization of SrTiO₃/Si(001),” EMRS fall 2021, virtual, 20 Sep 2021 - 23 Sep 2021. Proc. E-MRS fall. MRS. 20 Sep 2021

FACULTY OF ENGINEERING TECHNOLOGY
DEPARTMENT OF ELECTRICAL ENGINEERING
Wetenschapspark 27 box 15152
3590 Diepenbeek

